October 2021

Advances in Assessing Flood Hazard and Sediment Dynamics at the Coast

Hannah Baranes
University of Massachusetts Amherst

ADVANCES IN ASSESSING FLOOD HAZARD AND SEDIMENT DYNAMICS AT THE COAST

A Dissertation Presented

by

HANNAH E. BARANES

Submitted to the Graduate School of the
University of Massachusetts Amherst in partial fulfillment
of the requirements for the degree of

DOCTOR OF PHILOSOPHY

September 2021

Geosciences

ADVANCES IN ASSESSING FLOOD HAZARD AND SEDIMENT DYNAMICS AT THE COAST

A Dissertation Presented

by

HANNAH E. BARANES

Approved as to style and content by:

_____
Jonathan D. Woodruff, Chair

_____
Raymond S. Bradley, Member

_____
Robert M. DeConto, Member

_____
Elisabeth Hamin Infield, Member

_____
Stephen J. Burns, Department Head
Geosciences

ACKNOWLEDGMENTS

I owe a great deal of the joy, challenge, and fulfillment I experienced during my graduate career to a stellar team of mentors and colleagues. I have also had the privilege of studying and living on the ancestral homelands of the Nonotuck, west of the Nipmuc and Wampanoag, north of the Mohegan and Pequot, east of the Mohican, and south of the Abenaki. I remember those who were lost to white colonist genocide and recognize the resilient Native people live in Amherst today.

Thank you to my advisor, Jon Woodruff, for teaching me to problem-solve, write, and teach. Jon's humble brilliance, infectious excitement, and steady kindness motivated me to strive for excellence in my research. His willingness to learn alongside me enabled me to pursue the broad range of coastal topics covered in this dissertation. Thank you to the entire sedimentology and coastal processes research group for the support and laughter. Brian Yellen, Tim Cook, Frances Griswold, Kelly McKeon, Pedro Matos, Doug Beach, Caroline Ladlow, Alycia Ditroia, Stella Wenczel, Julia Casey, and Waverly Lau: you are a curious, kind, and all-around-awesome team of humans who make me excited to come into the lab and log on to Zoom meetings.

Thank you to my dissertation committee members Ray Bradley, Rob DeConto, and Elisabeth Hamin Infield for the thoughtful questions that pushed me to connect my research with broader societal challenges. I am also grateful to all the UMass Geosciences faculty who opened doors to formative public engagement and service opportunities. Thanks to Julie Brigam-Grette's longtime dedication to communicating science to policymakers, I was able to participate in a climate change briefing for a Massachusetts legislator and attend the United Nations COP-25 Climate Change

Conference. Rob DeConto and Jon Woodruff brought me onto the Greater-Boston Research Advisory Group and gave me experience writing a stakeholder-oriented climate projections report. Thank you to Michele Cooke for being a role model as a strong voice for enhancing justice, equity, diversity, and inclusion in the Geosciences and for inviting me to join her efforts to improve the graduate admissions process.

I would also like to thank my collaborators within and beyond UMass who lent their time and expertise to my projects. Jack Loveless taught me everything about earthquakes that appears in Chapter 1, and when I need a refresher, I still sometimes search my inbox for his emails that elegantly explain tectonics concepts. Thank you to Stefan Talke, who first thought to explore the impact of tidal nonstationarity on Boston flood hazard. His thoughtful revisions on Chapter 2 also taught me to write with more specificity and clarity. Thank you to Richard Ray for the technical guidance on tides, to Bob Kopp for his help with flood statistics, and to Rocky Geyer for the long Zoom calls discussing estuarine processes. Finally, thanks to Justin Richardson, who improved my writing when I had the opportunity to collaborate with him on a manuscript in my final months of graduate school. All the work that appears in this dissertation was possible thanks to this team of mentors.

The NASA Earth and Space Sciences Fellowship generously funded the first three years of my graduate career, and the Northeast Climate Adaptation Science Center graduate fellowship program funded my final year and a half. These fellowships gave the gifts of dedicated research time and flexibility to pursue enriching teaching and public engagement opportunities.

Finally, I give deep thanks to my family and friends. My parents, Cherie and Shalom, and my sisters, Elena and Sarah, are my role models as people who are dedicated to improving their communities through their work. My partner Mike inspires me to find joy in challenge, and I am so grateful to him for making me smile every single day of graduate school. The confidence and endurance required to pursue challenging work is born out of a rock-solid support system. Thank you for being that for me.

ABSTRACT

ADVANCES IN ASSESSING FLOOD HAZARD AND SEDIMENT DYNAMICS AT THE COAST

SEPTEMBER 2021

HANNAH BARANES, B.A., DARTMOUTH COLLEGE

M.S., UNIVERSITY OF MASSACHUSETTS AMHERST

Ph.D., UNIVERSITY FO MASSACHUSETTS AMHERST

Directed by: Professor Jonathan D. Woodruff

Earth's coastlines are shaped by geophysical and human dynamism. Waves, tides, currents, and sea level change reconfigure coastal environments on hourly to centennial timescales, and the coast is experiencing the fastest economic and population growth rates in the world. This coexistence of a dynamic environment and human development makes coastal communities uniquely vulnerable to natural hazards. Climate change is expected to exacerbate flooding and erosion hazards in the future; thus, it is critical that we understand the underlying physical drivers of coastal change. The overarching goal of this dissertation is to improve the mechanistic understanding and quantification of dynamic processes that shape the coastal environment. Specific topics range broadly from earthquake modeling to coastal flood statistics and salt marsh sediment dynamics.

Chapter 1 aims to constrain a worst-case earthquake and tsunami along southwestern Japan's Nankai Trough using novel earthquake rupture modeling techniques. The work is motivated by a mismatch between lacustrine sedimentological records of tsunami inundation in the region and modeled earthquake and tsunami scenarios in published literature. Recent advances in space geodesy enable high-precision

measurements of crustal motion that can be used to estimate the degree of frictional locking along fault interfaces, known as interseismic coupling. We demonstrate methods for scaling modern interseismic coupling to coseismic slip to construct Nankai Trough earthquake scenarios. Results show that coupling-based models produce distributions of ground surface deformation and tsunami inundation that are similar to historical and geologic records of the largest known Nankai earthquake in C.E. 1707 and to an independent, quasi-dynamic rupture model. This implies that contemporary coupling mirrors the slip distribution of a full-margin, 1707-type rupture, and GPS measurements of surface motion are connected with the trough's physical characteristics.

Chapter 2 presents a new statistical methodology for calculating non-stationary flood height-frequency relationships that account for modulation of flood hazard by predictable tidal cycles. We developed the methodology after the winter of 2018, when two Nor'easters with relatively moderate storm surges led to the first and third highest water levels recorded at the Boston tide gauge in 100 years due to their overlap with anomalously high tides. Applying the new method in the Gulf of Maine, we find significant tidal forcing of winter storm season flood hazard by the 18.6-year nodal cycle; for example, the nodal cycle forces decadal oscillations in the 1% annual chance storm tide at an average rate of ±13.5 mm/y in Eastport, ME; ±4.0 mm/y in Portland, ME; and ±5.9 mm/y in Boston, MA.

Appendix C is a contribution to the City of Boston's climate projections report that combines the Chapter 2 methodology with probabilistic sea level rise to generate probabilistic flood projections that account for both sea level and tidal non-stationarity. We outline mechanisms of both extreme and tide-only coastal flooding; describe the

impacts of climatic and natural tidal variability on flood hazard; give context for the record-breaking 2018 floods; and provide projections of flooding through 2100. Projections show that increases in the frequency and magnitude of flood hazard driven by sea level rise will plateau during decades when the 18.6-year nodal cycle is in a negative phase (2019-2027 and 2037-2046) but accelerate in the subsequent decade as the nodal cycle enters a positive phase and increased tide range combined with sea level rise amplifies flood hazard (2028-2036 and 2047-2055). Beyond mid-century, the importance of tide range on probabilistic flood projections becomes less important, as background sea level rise becomes the dominant influence on flooding.

Chapter 3 presents an observational study of sediment delivery to a New England tidal salt marsh. An external clastic sediment supply is a key factor in determining salt marsh resilience to future sea level rise, yet information on sources, mechanisms, and timescales of sediment delivery are lacking for most marsh systems. We show that marine sediment mobilized and delivered during coastal storms is the primary source to the North and South River, a mesotidal bar-built estuary typical to New England. On the marsh platform, deposition rates, clastic content, and dilution of fluvially-sourced contaminated sediment by marine material all increase down-estuary toward the estuary inlet, consistent with a dominantly marine-derived sediment source. Marsh clastic deposition rates are also highest in the storm season. We observe that periods of elevated turbidity in channels and over the marsh are concurrent with storm surge and high wave activity offshore, rather than with high river discharge. Flood tide turbidity also exceeds ebb tide turbidity during these high turbidity intervals. Timescales of storm-driven marine sediment delivery range from 2.5 days (5 tide cycles) to 2 weeks, depending on location

within the estuary; therefore the phasing of storm surge and wave events with the spring-neap cycle determines how effectively post-event suspended sediment is delivered to the marsh platform. This study reveals that sediment supply and the associated resilience of New England mesotidal salt marshes involves the interplay of coastal and estuarine processes, underscoring the importance of looking both up- and downstream to identify key drivers of environmental change.

PREFACE

Chapter 1 / Appendix A

Chapter one and Appendix A were published in *Geophysical Research Letters* (2018) and are written in first person plural with co-authors Jonathan Woodruff, John Loveless, and Mamoru Hyodo. No changes have been made to the published manuscript.

Chapter 2 / Appendix B

Chapter two and Appendix B were published *Journal of Geophysical Research Letters: Oceans* (2020) and are written in first person plural with co-authors Jonathan Woodruff, Stefan Talke, Robert Kopp, Richard Ray, and Robert DeConto. No changes have been made to the published manuscript.

Chapter 3 / Appendix D

Chapter three and Appendix D contain a manuscript submitted to *Journal of Geophysical Research: Earth Surface* and are written in first person plural in collaboration with Jonathan Woodruff, Rockwell Geyer, Brian Yellen, and Justin Richardson. No changes have been made to the [prepared/submitted] manuscript.

Appendix C

Appendix C contains the coastal flooding chapter of a climate projections report written for the City of Boston. The chapter is written in first-person plural in collaboration with Robert DeConto, Jonathan Woodruff, Robert Kopp, and Anna Ruth Halberstadt. The chapter is currently in review, and no changes have been made to the submission.

TABLE OF CONTENTS

Page

LIST OF TABLES

LIST OF FIGURES

Figure Page

CHAPTER 1

INTERSEISMIC COUPLING-BASED EARTHQUAKE AND TSUNAMI SCENARIOS FOR THE NANKAI TROUGH

1.1 Abstract

Theoretical modeling and investigations of recent subduction zone earthquakes show that geodetic estimates of interseismic coupling and the spatial distribution of coseismic rupture are correlated. However, the utility of contemporary coupling in guiding construction of rupture scenarios has not been evaluated on the world's most hazardous faults. Here we demonstrate methods for scaling coupling to slip to create rupture models for southwestern Japan's Nankai Trough. Results show that coupling-based models produce distributions of ground surface deformation and tsunami inundation that are similar to historical and geologic records of the largest known Nankai earthquake in C.E. 1707 and to an independent, quasi-dynamic rupture model. Notably, these models and records all support focused subsidence around western Shikoku that makes the region particularly vulnerable to flooding. Results imply that contemporary coupling mirrors the slip distribution of a full-margin, 1707-type rupture, and GPS measurements of surface motion are connected with the trough's physical characteristics.

1.2 Plain Language Summary

In regions that are vulnerable to earthquakes, constructing rupture scenarios based on scientific observations of faults is key to managing risk. High-precision GPS measurements that track the motion of earth's crust can be used to estimate interseismic

coupling, which is a measure of frictional locking along fault interfaces that causes stress buildup between earthquakes. Past studies have shown that the distribution of coupling preceding an earthquake is correlated with rupture during an earthquake. We demonstrate methods for constructing rupture scenarios based on estimates of coupling for southwestern Japan's Nankai Trough, where a magnitude 8-9 earthquake is likely to occur within the next few decades. Modeled ground surface deformation and tsunami inundation for these coupling-based rupture scenarios are similar to historical and geologic records of the largest known Nankai earthquake in C.E. 1707 and to an independent rupture model based on the trough's physical characteristics. Notably, these models and records all show that the ground surface around western Shikoku sinks during earthquake rupture and becomes particularly vulnerable to tsunami flooding. Our results imply that contemporary coupling mirrors the rupture pattern of the Nankai Trough's largest known historical event and that GPS measurements of surface motion are connected with the trough's physical characteristics.

1.3 Introduction

Subduction-zone earthquakes and accompanying tsunamis have catastrophically damaged coastal communities around the world. Recent advances in space geodesy that offer unprecedented insight into the present-day kinematic behavior of faults have the potential to significantly advance earthquake hazard assessment (Feigl et al., 1993; Hager et al., 1991). High-precision measurements of crustal motion can be used to estimate spatiotemporal variation in slip deficit that accumulates where a fault interface is locked by friction between earthquakes (Loveless & Meade, 2016; McCaffrey et al., 2000;

Nishimura & Hashimoto, 2006). Interseismic coupling is the ratio of this estimated slip deficit to relative plate motion. Both numerical simulations (Kaneko et al., 2010) and observations from the 2010 Maule (Moreno et al., 2010), 2011 Tōhoku (Loveless & Meade, 2011), and 2012 Nicoya (Protti et al., 2014) megathrust earthquakes have provided evidence for correlation between the estimated spatial distributions of interseismic coupling and subsequent coseismic slip. These studies have posited that coupling may be used to anticipate the spatial extent of future rupture. Here, we test this correlation on one of the world's most hazardous faults by creating rupture scenarios from coupling distributions and evaluating the scenarios by comparing simulated ground surface deformation and tsunami inundation to historical and geologic observations.

The Nankai Trough, located just offshore of southwestern Japan (Figure 1.1a), is ideal for testing the utility of recent, geodetically-constrained estimates of interseismic coupling in constructing future rupture scenarios. Following the unexpectedly severe 2011 Tohoku earthquake, Japan's government called for hazard-assessment research to focus on defining worst-case scenarios for earthquakes and tsunamis impacting the country (Central Disaster Management Council, 2012). This guideline has focused attention on the Nankai Trough, where the subduction of the Philippine Sea Plate beneath the southwest Japan forearc is predicted to generate a magnitude 8-9 earthquake within the next few decades (Headquarters for Earthquake Research Promotion, 2013). Thirteen-hundred years of historical records document Nankai earthquakes occurring every 100-200 years (Ishibashi, 1999), and numerous studies have documented ~8,000 years of land-based geologic evidence for Nankai earthquakes (Garrett et al., 2016 and references therein). The largest known historical Nankai earthquake occurred in C.E. 1707 and is

thought to have simultaneously ruptured the majority of the trough, extending from Suruga Bay southwest to Hyūga-nada (i.e. the full length shown in Figure 1.1a). Documentation of the resultant tsunami height reaches 10 m in the most severely impacted areas along the open Pacific coastline of Shikoku, Japan (Hatori, 1974, 1985; Murakami et al., 1995).

Japan's extensive GEONET GPS network has measured crustal motion across the Japanese islands since 1996, and several studies have utilized this dataset to estimate the distribution of interseismic coupling for the Nankai Trough (Loveless & Meade, 2016; Nishimura & Hashimoto, 2006; Yokota et al., 2016; Nishimura et al., 2018). These coupling estimates differ in detail depending on whether or not the contributions of crustal block motion to the GPS velocity field are considered, and whether or not seafloor geodetic measurements are used in addition to land-based GEONET data. However, the resultant spatial distributions of coupling in these studies are broadly similar. In particular, strong coupling is estimated along the Nankai interface from Kyushu to the Tokai region, with concentrations offshore Shikoku and the Kii peninsula, coincident with the estimated rupture areas of the great 1944 and 1946 earthquakes (e.g., Sagiya and Thatcher, 1999).

There are also several published rupture scenarios for a future worst-case Nankai earthquake that draw on geophysical, geologic, and historical investigations of the trough. A series of simple, kinematic source models (models of coseismic slip that do not consider stress conditions or the fault's physical properties) have been formulated to match historical and geologic records of ground shaking and tsunamigenic flooding from the 1707 earthquake, which is often considered a worst-case event (Aida, 1981; Ando,

1975; An'naka et al., 2003; Furumura et al., 2011). As geophysical studies have enabled physical characterization of the Nankai subduction interface, large rupture scenarios have also been generated from dynamic and quasi-dynamic simulations that solve the spatiotemporal evolution of slip by incorporating the trough's geometry, geologic structure, and frictional properties (Hok et al., 2011; Hyodo & Hori, 2013; Kodaira et al., 2006). Dynamic simulations consider inertial effects, while quasi-dynamic simulations approximate them with a radiation damping term. One kinematic model of the 1707 earthquake used an interseismic coupling distribution to support extending its rupture area (Furumura et al., 2011), and one dynamic simulation used slip deficit rates to define an initial stress distribution (Hok et al., 2011); however, there is no rupture scenario based solely on the spatial correlation between coupling and slip. Furthermore, we emphasize that our interseismic coupling estimates consider crustal block motion in southwestern Japan, which reduces potential biases in moment accumulation on the Nankai subduction interface that may arise by neglecting this motion.

1.4 Methods

Here, we create a set of four new kinematic rupture models for the Nankai Trough by linearly scaling estimated interseismic coupling to coseismic slip. We use temporally-averaged coupling fraction distributions estimated with elastic block models (Loveless & Meade, 2016) (Appendix A, Text S1). This technique simultaneously considers the contributions to the geodetic velocity field from interplate coupling and crustal block motion. Near-trench coupling is poorly resolved, in part due to the scarcity of seafloor geodetic data (Yokota et al., 2016; Yasuda et al., 2017; Nishimura et al., 2018); thus,

following Loveless and Meade (2016), we adopt two candidate coupling scenarios (Figure 1.1c): one in which non-zero slip deficit can be estimated along the trench ("trench-coupled" scenario) and one in which the subduction interface around the trench is assumed not to accumulate slip deficit ("trench-creeping" scenario). When translating coupling to coseismic slip for the trench-coupled and trench-creeping cases, we also test two methods for determining the rake (direction) of slip: 1) opposite the direction of accumulated slip deficit, and 2) opposite the direction of relative plate motion (Appendix A, Text S1). Of the four slip models, we favor the trench-coupled distribution with rake of slip opposite the direction of slip deficit. Direct observations from drilling (Sakaguchi et al., 2011) and new coupling estimates that incorporate a few years of seafloor geodetic measurements (Yokota et al., 2016) both indicate that coupling at the trench is likely, and the first rake method produces a fanning pattern of coseismic rakes around concentrations of slip that is consistent with spatially-variable slip magnitudes. Although we favor this one scenario, considering all four better represents the uncertainty in our methodology for scaling a given coupling distribution to slip, and it addresses the possibility that coupling near the trench might not necessarily translate to shallow coseismic slip (e.g., Ide et al., 2011).

Finally, we test a range of peak slip magnitudes for the linear scaling of coupling to slip. The Nankai Trough is currently coupled along its entire length (Figure 1.1b), so we scale slip to generate an event comparable to the most recent full-margin Nankai rupture in 1707. There are no measurements of the 1707 earthquake's magnitude, but historical records document the resultant tsunami's height (Hatori, 1974, 1985; Murakami et al., 1995); thus, we simulate tsunami inundation with a range of peak slip magnitudes

for each of the four coupling-based slip distributions and choose the value that produces the best match between modeled and observed 1707 tsunami heights. We perform tsunami inundation simulations using version 5.3.0 of the open source tsunami model GeoClaw (Berger et al., 2011; Clawpack Development Team, 2015; Mandli et al., 2016), which is a subset of Clawpack. Earthquake sources for tsunami simulations, GeoClaw model parameters, development of a topographic model, and methodology for comparing modeled and historical tsunami inundation heights are all described in detail in Appendix A Text S2-S4 and Figure A.1.

1.5 Results and Discussion

Table 1.1 provides the best fit peak slip values and associated seismic moments (m0), moment magnitudes, and return periods for each coupling-based rupture scenario. Return periods are calculated using the scenario slip magnitudes and estimated slip deficit rates from the block models. Estimated seismic moments are consistent among the four scenarios, with the average internal m0 deviation equaling 16% of the average estimated m0. Scenario return periods range from 236 to 384 years. In paleoseismic studies, Nankai earthquake recurrence intervals are poorly constrained due to uncertainty in event chronology, event magnitude, and flood threshold characterization (Garrett et al., 2016). However, historical records indicate that full-length Nankai ruptures occurred in C.E. 1707, 1361, and 684 (Garrett et al., 2016 and references therein). Our calculated 236 to 384-year return period for the accumulated Nankai Trough slip deficit is similar to the return periods for the two most recent historical full-margin events in C.E. 1707 and 1361, and slightly shorter when considering three events between present and C.E. 684.

Figures 1.1c and 1.1d show modeled coupling distributions, slip magnitudes, and vertical ground surface displacements for the four rupture scenarios. The trench-creeping and trench-coupled scenarios differ principally in terms of the down-dip locations of concentrated slip. Because of the enforced creep at the shallowest portion of the interface in the trench-creeping models, the down-dip gradient in coupling, and hence scenario slip, is steeper than in the trench-coupled models. This variation in down-dip locus of slip yields vertical displacement patterns showing a similar shift: peak uplift and subsidence calculated from the trench-creeping models are located farther northwest than those of the trench-coupled models, which feature peak slip near the trench. The along-strike slip concentrations near Shikoku and the Kii Peninsula are consistent between the trench-coupled and trench-creeping cases and are broadly consistent with other estimates of interseismic coupling (e.g. Yokota et al., 2016). Distributions of modeled ground surface displacement differ for the two methods of assigning rake of slip: the along-strike variation in uplift is smoother for scenarios with rake opposite the direction of relative plate motion and more spatially variable with smaller regions of focused uplift for scenarios with rake opposite the direction of slip deficit.

Modeled vertical ground surface displacement also has varying agreement with geologic evidence for past coseismic uplift and subsidence. There is robust geologic evidence for uplift associated with Nankai earthquakes at Cape Muroto (Iryu et al., 2009; Maemoku, 1988, 2001) and the southern tip of the Kii peninsula (Shishikura et al., 2008, 2013) (locations 1 and 2, respectively, in Figure 1.1d). There is also a potential indication of uplift in southwestern Shizuoka prefecture (Azuma et al., 2005; Fujiwara et al., 2007a, 2010) and subsidence at in Suruga Bay (Fujiwara et al., 2007b, 2016) (locations 3 and 4

in Figure 1.1d), but the connection between deformation to Nankai earthquakes is more uncertain at these sites (Garrett et al., 2016). Three of the four coupling-based models reproduce the observed uplift around Cape Muroto and the Kii peninsula, but they do not consistently reproduce the uplift in Shizuoka and subsidence in Suruga Bay. The Kochi Plain also subsided ~60 cm during the 1946 Nankai earthquake (Geographical Survey Institute of Japan, 1952; Miyabe, 1955). Although subsidence around Kochi is commonly cited as a feature of Nankai earthquakes (e.g. Ando, 1975; Furumura et al., 2011), our coupling-based simulations do not produce this subsidence. Hyodo et al. (2014) conducted a series of modeling experiments demonstrating that slip on the downdip extent of the Nankai subduction interface reduces Pacific coastal subsidence and lowers tsunami heights such that they are more consistent with historical observations of the 1707 event. This is consistent with our coupling-based rupture scenarios, where the strongly coupled patch of the subduction interface underlying Shikoku produces large slip on its downdip extent (Figure 1.1d), and modeled tsunami heights largely agree with 1707 observations on Shikoku's Pacific coast (Figure 1.2d).

The spatial distributions of modeled tsunami inundation are internally consistent among the four coupling-based scenarios (gray line with shading in Figures 1.2c-e shows the range). Along most of the coast, tsunami heights vary by less than 0.5 m among scenarios, and larger inconsistencies are generally due to local variation in vertical ground surface deformation. The purpose of these tsunami simulations is to validate coupling-based rupture models against observations of the 1707 Nankai event of record; thus, we do not attempt to provide detailed sensitivity testing and modeled inundation analysis that would be required for tsunami simulations intended for hazard mitigation.

Along most of the Nankai Trough, the spatial distribution of flooding from the scaled, coupling-based model tsunamis compares favorably with the distribution of observed 1707 tsunami heights (circles in Figures 1.2c-e). This general consistency indicates that contemporary coupling along the trough mirrors the slip distribution of a full-margin, 1707-type rupture. The model-observation fit is particularly consistent in Shikoku and Honshu, where the most historical observations are available. For 25 of 33 observations in Shikoku and 20 of 30 observations in Honshu, the discrepancy between the coupling-based model and the observed tsunami height is less than 25% of the observed height (Appendix A, Text S5). In Kyushu, 3 of the 9 available observations of the 1707 tsunami are matched. General model exceedance for the remaining 6 could be due to uncertainty in the limited number of historical observations available for this region (Ando, 1975; Ishibashi, 2004; Murakami et al., 1995). These 6 unmatched Kyushu observations are also clustered around a strongly coupled patch of the Nankai interface south of the Bungo Channel (Figures 1.1c, 1.2c). In this region there are known slow-slip events (Ozawa et al., 2013), and the coupling fraction has varied since 1996 (Loveless & Meade, 2016), potentially adding uncertainty to the local modeled slip distribution. Figure 1.2 also highlights the contribution of coseismic uplift and subsidence to tsunamigenic flooding along Japan's coast. Vertical ground displacement changes maximum flood heights by 1-2 m along more than half of the coastline shown in Figure 1.2, and subsidence accounts for a significant fraction of the total inundation height along major coastline segments on all three mainland islands. In western Shikoku in particular, focused coseismic subsidence contributes to unexpectedly large flood heights (up to 7 m)

in the Bungo Channel region that otherwise would be relatively sheltered from Nankai Trough tsunamis (Figures 1.1d, 1.2d).

We focus attention on validating the identified region of subsidence in the Bungo Channel (Figure 1.1a) both because the area contains Shikoku's sole nuclear power plant (Ikata Power Plant), and because historical records for the 1707 tsunami along the west coast of Shikoku are geographically limited to the Uwajima embayment, where 4-5 m of inundation was recorded (Figure 1.2d). Over the duration of each tsunami simulation, we monitor water level with model tide gauges at two locations within this subsided region (Figure 1.3): one within the Uwajima embayment and two at Lake Ryuuoo. Lake Ryuuoo is the site of a recent back-barrier sedimentological reconstruction that provided 4 m as the region's first physically-based 1707 tsunami inundation height constraint (Baranes et al., 2016). At Uwajima, ~2 m of coseismic subsidence and a ~2.5 m tsunami combine to match historical documentation of a 4-5 m tsunami impacting the city in 1707 (Figure 1.3c) (Murakami et al., 1995). At Lake Ryuuoo, subsidence lowers the barrier beach separating the lake from the ocean by nearly 2 m. This subsidence allows for barrier inundation by the 1707 tsunami and is required to explain a marine flood deposit within Lake Ryuuoo's sediment that dates to the event (Figure 1.3d) (Baranes et al., 2016). Coupling-based rupture scenarios, the Lake Ryuuoo sedimentary record, and historical observations therefore provide three independent lines of evidence for substantial subsidence on the eastern side of the Bungo Channel.

As a final means of validation, we compare our kinematic coupling-based models to the independent, quasi-dynamic "larger-earthquake scenario" from Hyodo et al. (2014) (Mw = 9.03; m0 = 4.37 x 1022 N-m; peak slip = 20.6 m), hereafter referred to as H14.

The H14 slip distribution is based on the geometry, geologic structure, and frictional properties of the Nankai Trough inferred from geophysical studies. Like our two trench-coupled rupture scenarios, the H14 model also allows for slip at the trench axis. Estimated seismic moments are consistent among the H14 and the two trench-coupled scenarios, with the average internal M0 deviation equaling 16% of the average estimated M0. Figures 1.1b and 1.1d also illustrate the similar pattern of vertical ground surface displacement produced by the independent kinematic and quasi-dynamic modeling techniques. The spatial extent of rupture is nearly identical for the two cases, and both include slip on the downdip extent of the subduction interface that yields a focused region of subsidence around western Shikoku (eastern side of the Bungo Channel). For the coupling-based models, the transition from offshore uplift to inland subsidence generally occurs farther to the northwest, and the pattern of ground surface deformation is more complex. The greater complexity is to be expected, given that the coupling-based models are based on GPS data, while the H14 model is based on a smoother set of defined fault characteristics (Figure 1.3 in Hyodo & Hori, 2013).

The kinematic and quasi-dynamic scenarios also produce a consistent distribution of modeled tsunami inundation along the Kyushu, Shikoku, and Honshu coastlines (Figure 1.2; methods described in Appendix A, Text S2-S4). Maximum tsunami heights are generally within 2 m of each other, and spatial variation in modeled inundation is similar over both 100 and 1000-km-scale distances along impacted coastlines of Japan. Furthermore, similar to the coupling-based scenario results, subsidence in the H14 model enables the tsunami to inundate Lake Ryuuoo (Figure 1.3d). The quasi-dynamic modeling approach in H14 is therefore not only consistent with kinematic coupling-based

scenarios, but also with sedimentological evidence for subsidence in the region. These similarities in simulated seismic moment, ground surface displacement, and tsunami inundation between the coupling-based and H14 models both support the scaling of coupling to slip as a valid tool for generating rupture scenarios, and demonstrate the connection between modern geodetic measurements of surface motion and physical characteristics of the subduction interface.

1.6 Conclusions

This study demonstrates methods for constructing and evaluating rupture scenarios based on the scaling of interseismic coupling to coseismic slip. Results show similarities in ground surface deformation and tsunami inundation among kinematic coupling-based Nankai Trough rupture scenarios, historical and geologic records of the 1707 earthquake and tsunami, and the independent, quasi-dynamic H14 model. Study implications include:

1. Contemporary coupling mirrors the slip distribution of a full-margin, 1707-type rupture of the Nankai Trough.
2. Coupling-based rupture scenarios, historical observations from Uwajima, the Lake Ryuuoo sedimentological record, and the H14 quasi-dynamic model all independently support focused coseismic subsidence in western Shikoku.
3. There is a connection between geodetic measurements of surface motion and physical properties of the subduction interface.

1.7 Acknowledgments and Data

Funding was provided by the US National Science Foundation (Award 1630090) and the National Aeronautics and Space Administration (Award NNX16AO24H S02). We thank K. Imai for providing us with historical tsunami heights compiled from existing studies. Ground surface displacements for the coupling-based scenarios are provided in the supporting information. Sources for coupling distributions, topographic data used in tsunami simulations, 1707 tsunami historical observations, and the GeoClaw code are provided in the references.

Table 1.1. Best fit peak slip values and associated seismic moments, moment magnitudes, and return periods (based on estimated slip deficit rates) for the four coupling-based rupture scenarios.

Near-trench behavior	Slip rake	Peak slip (m)	m_0 (N-m x 10^{22})	M_W	Return period (years)
Coupled	Opposite slip deficit	16	3.43	8.99	236
Coupled	Opposite relative plate motion	26	4.22	9.05	384
Creeping	Opposite slip deficit	18	2.69	8.92	286
Creeping	Opposite relative plate motion	20	2.60	8.91	257

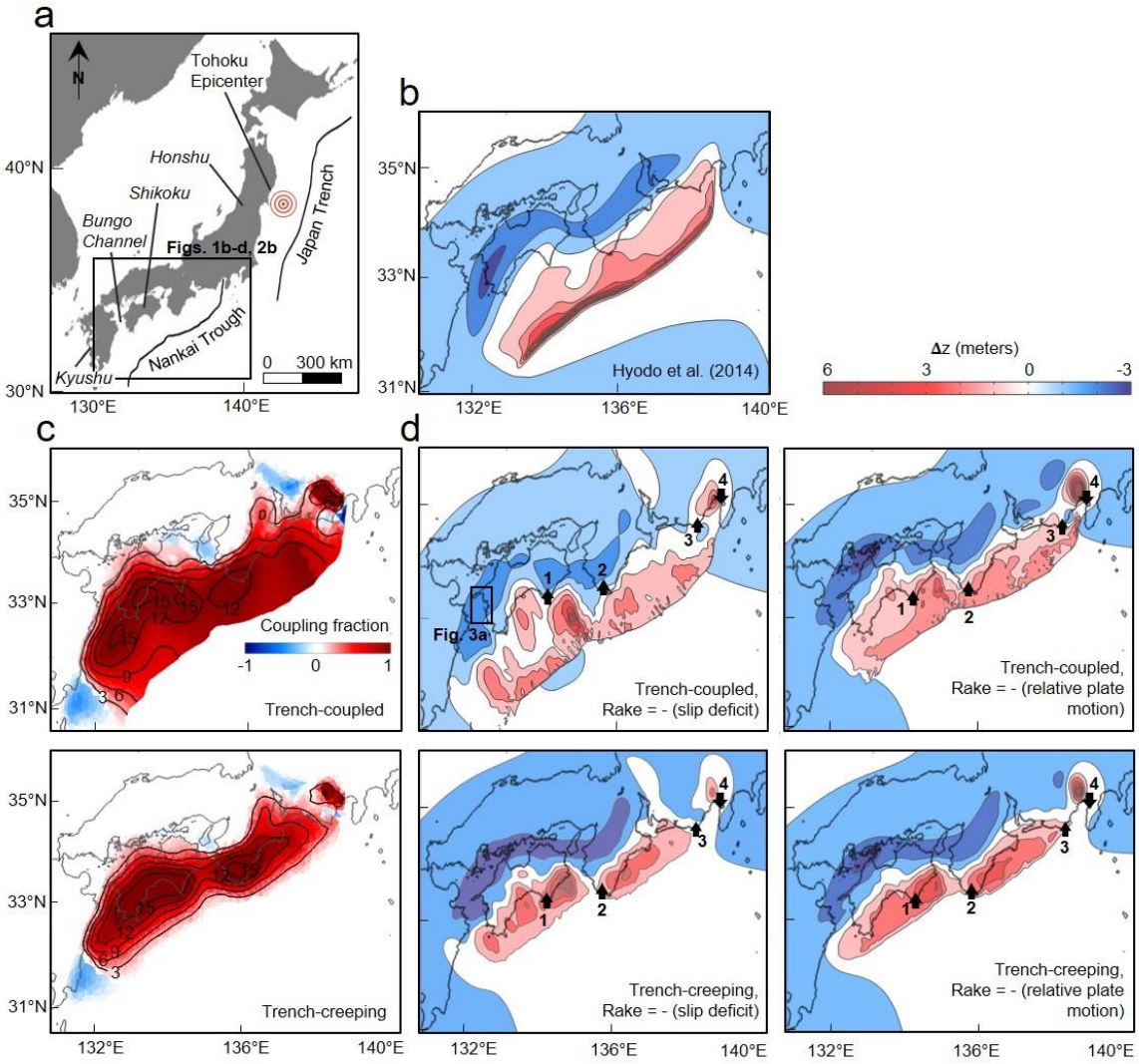

Figure 1.1. Nankai Trough earthquake scenarios. **a** Regional setting of the Nankai Trough. **b** Vertical surface displacement for a previously published and independent quasi-dynamic rupture model by Hyodo et al. (2014). **c** Nankai Trough coupling fraction for the "trench-coupled" and "trench-creeping" cases (Loveless & Meade, 2016), where coupling fraction is defined as the ratio of slip deficit rate to relative plate motion rate. Contour lines show the resulting coseismic slip magnitudes in meters for the cases where rake of slip is opposite slip deficit (see Table 1 for peak slip values). **d** Calculated vertical surface displacement for the four kinematic coupling-based models. Locations 1-4 referenced in text.

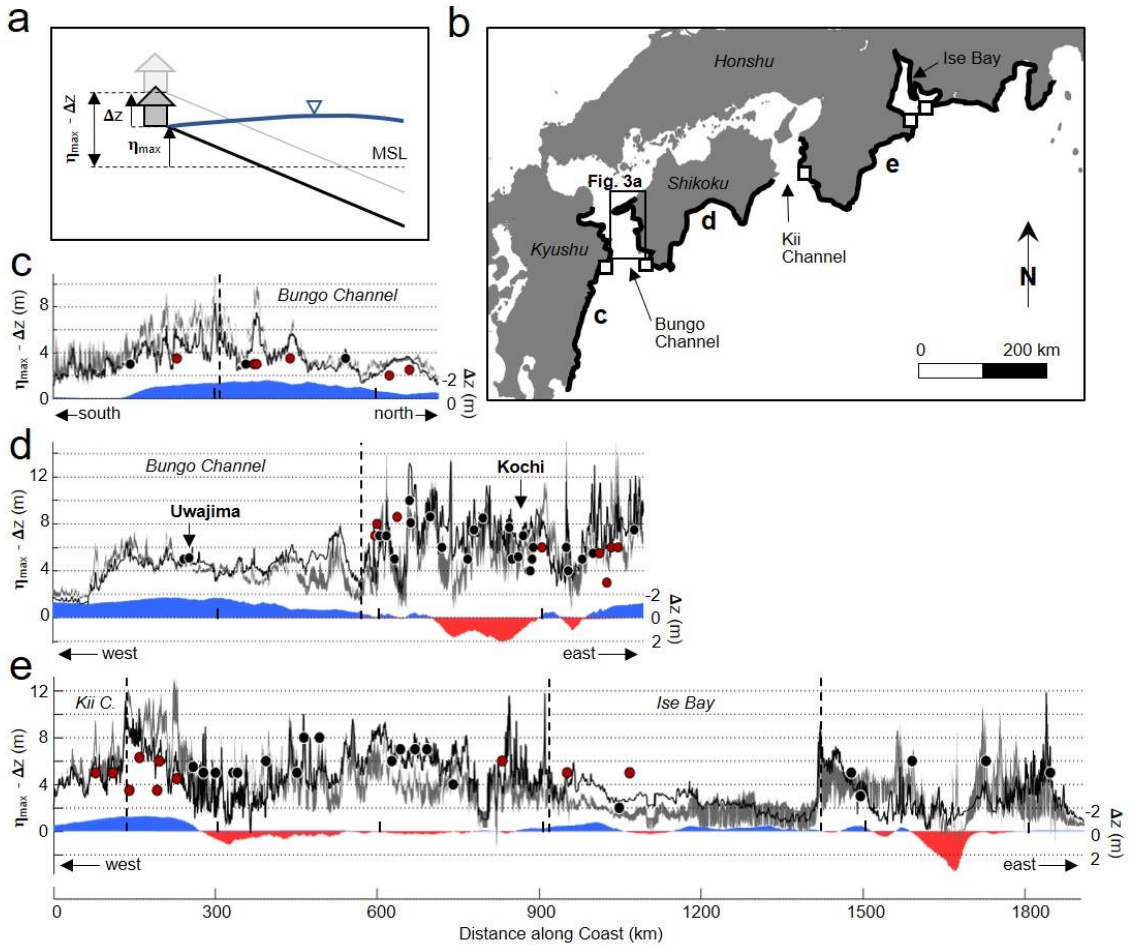

Figure 1.2. Modeled inundation heights due to both tsunami and vertical land movement. **a** Illustration of maximum total water level change, η_{max} - Δz (left-hand y-axis in c-e), where Δz = vertical ground surface displacement (right-hand y-axis in c-e), and η_{max} = maximum tsunami height above MSL. **b** Regional coastline near the Nankai Trough, where distance is mapped on x-axes in c, d, and e. White squares mark transitions between open Pacific and relatively sheltered coastlines. **c to e** η_{max} - Δz along coastlines for the H14 scenario (black line) and the four coupling-based scenarios in Table 1 (gray line with shading shows range for four cases). Blue and red filled regions centered at zero show the contributions of subsidence (negative Δz) and uplift (positive Δz), respectively, to total relative water level change (i.e. η_{max} - Δz). Circles represent observed 1707 tsunami inundation heights (Hatori, 1974, 1985; Murakami et al., 1995) (black if the discrepancy between modeled and observed tsunami heights is < 25% of the observed height, and red if not). Vertical dashed lines in c, d, and e denote locations of squares in b.

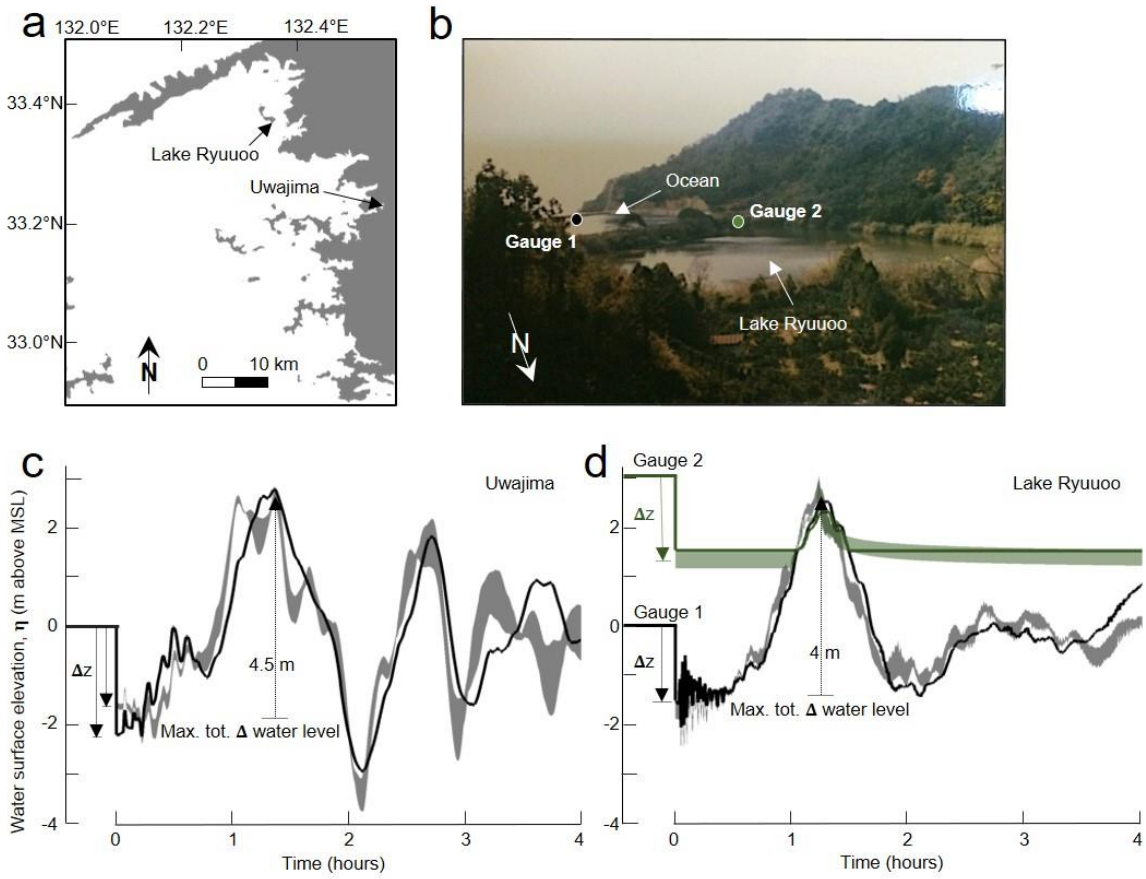

Figure 1.3. Model gauge results in the Bungo Channel region of focused subsidence. **a** Northwestern Shikoku model gauge locations (see Figure 1.1 for regional context). **b** Photograph of Lake Ryuuoo showing locations of model gauges, where Gauge 1 is offshore, and Gauge 2 is on the lowest-elevation area of Lake Ryuuoo's barrier beach. **c** Uwajima and **d** Lake Ryuuoo gauge results for the H14 scenario (green and black solid lines for Gauges 1 and 2, respectively), and the four coupling-based scenarios (green and black shaded regions). Note in d how subsidence (Δz) is required for the observed inundation of Lake Ryuuoo's barrier beach (Gauge 2).

CHAPTER 2

TIDALLY DRIVEN INTERANNUAL VARIATION IN EXTREME SEA LEVEL FREQUENCIES IN THE GULF OF MAINE

2.1 Abstract

Astronomical variations in tidal magnitude can strongly modulate the severity of coastal flooding on daily, monthly, and interannual timescales. Here, we present a new quasi-nonstationary skew surge joint probability method (qn-SSJPM) that estimates interannual fluctuations in flood hazard caused by the 18.6 and quasi 4.4-year modulations of tides. We demonstrate that qn-SSJPM-derived storm tide frequency estimates are more precise and stable compared with the standard practice of fitting an extreme value distribution to measured storm tides, which is often biased by the largest few events within the observational period. Applying the qn-SSJPM in the Gulf of Maine, we find significant tidal forcing of winter storm season flood hazard by the 18.6-year nodal cycle, whereas 4.4-year modulations and a secular trend in tides are small compared to interannual variation and long-term trends in sea-level. The nodal cycle forces decadal oscillations in the 1% annual chance storm tide at an average rate of ±13.5 mm/y in Eastport, ME; ±4.0 mm/y in Portland, ME; and ±5.9 mm/y in Boston, MA. Currently (in 2020), nodal forcing is counteracting the sea-level rise-induced increase in flood hazard; however, in 2025, the nodal cycle will reach a minimum and then begin to accelerate flood hazard increase as it moves toward its maximum phase over the subsequent decade. Along the world's meso-to-macrotidal coastlines, it is therefore critical to consider both sea-level rise and tidal non-stationarity in planning for the

transition to chronic flooding that will be driven by sea-level rise in many regions over the next century.

2.2 Plain Language Summary

Coastal management practices around flood risk often rely on estimates of the percent chance of a particular flood height occurring within a year. For example, U.S. flood insurance requires designating areas with a 100-year flood recurrence interval (the "100-year flood zone"). When storms hit regions with large tides, the height and timing of high tide often determine flood severity. Thus, the relationship between flood height and annual frequency can be altered by natural, daily-to-decadal cyclical variation in tide heights. Here, we present a new method for calculating annually-varying flood height–frequency relationships based on known tidal cycles. Applying the new method in the Gulf of Maine, we find an 18.6-year-long tidal cycle (the *nodal cycle*) has forced decadal variation in the 1% annual chance flood at a faster rate than the historical average rate of sea-level rise over the past century. Currently, nodal cycle forcing is counteracting the sea-level rise-induced increase in flood hazard; however, in 2025, the nodal cycle will reach a minimum in the Gulf and then begin to accelerate flood hazard as it moves toward its maximum over the subsequent decade. It is therefore critical to consider sea-level rise and tidal variation in medium-term flood hazard planning.

2.3 Glossary of acronyms

GEV	Generalized Extreme Value distribution
GPD	Generalized Pareto distribution
GPD_{ST}	Generalized Pareto distribution fit to measured storm tides

JPM	Joint probability method
MSL	Mean sea level
NOAA	National Oceanic and Atmospheric Administration
qn-SSJPM	Quasi-nonstationary joint probability method
RJPM	Revised joint probability method
SLR	Sea-level rise
SSJPM	Skew surge joint probability method
$ST_{0.01}$	Storm tide at the 0.01 exceedances/year level

2.4 Introduction

Extreme coastal flooding poses a growing hazard to coastal communities (e.g. Hallegatte et al., 2013; Neumann et al., 2015). Management practices around flood risk often require estimates of extreme sea level recurrence intervals; for example, in the United States, federal flood insurance and building codes depend on estimates of the current 100-year flood zone (Galloway et al., 2006; Hunter, 2010; Buchanan et al., 2017). Coastal flood hazard, however, is not stationary. The relationship between flood height and recurrence interval is approximately log-linear, so even small interannual variations in storm surge, tides, waves, or mean sea-level (trends on the order of millimeters per year) can significantly alter extreme sea level frequencies (e.g. Oppenheimer et al., 2019). Robust statistical methods for considering sea-level non-stationarity (Hunter, 2010; Buchanan et al., 2017; Wahl et al., 2017) have been used to incorporate uncertain sea-level rise (SLR) projections into global (e.g. Lin et al., 2016; Garner et al., 2017; Oppenheimer et al., 2019) and local (e.g. NYC, 2013; Douglas et al., 2016; Griggs et al.,

2017) hazard assessments. In this paper, we investigate the impact of quasi-deterministic variation in astronomical tides on low-frequency, high-impact extreme sea levels.

Tidal magnitude modulates the severity of flooding in meso-to-macrotidal regions, and interannual variation in tides causing periods of enhanced flood risk is a well-known phenomenon (e.g. Sobey, 2005; Eliot, 2010; Menéndez & Woodworth, 2010; Ray & Foster, 2016; Talke et al., 2018; Peng et al., 2019; Haigh et al., 2020; Talke & Jay, 2020). In particular, the 18.6-year lunar nodal cycle and the 8.85-year cycle of lunar perigee influence high water globally on weekly, monthly, and annual timescales (e.g., Haigh et al., 2011; Peng et al., 2019). Ray and Foster (2016) showed that the perigean cycle modulates predicted future nuisance tidal flooding at a quasi 4.4-year period. For extreme flooding, Menéndez and Woodworth (2010) modeled global nodal and perigean astronomical modulations using a non-stationary location parameter in extreme sea level probability distributions fit to satellite altimetry records over the 1970–2008 time period. Over a longer, nearly 200-year record from Boston, Massachusetts, Talke et al. (2018) also showed that the nodal cycle produces 10–20 cm of variation in extreme sea levels with recurrence intervals between 2 and 100 years.

On decadal to centennial timescales, non-astronomical factors also force local-to-global-scale variations and trends in tides (Schindelegger et al., 2018; Haigh et al., 2020; Talke & Jay, 2020). Changes in water depth, shoreline position, frictional resistance, and river flow have led to dramatic local-scale tidal amplification and reduction over the past two centuries, particularly in estuaries and tidal rivers (Winterwerp et al., 2013; Haigh et al., 2020; Talke & Jay, 2020). Spatially coherent, regional-scale variation in tides has been driven by changes in ocean depth, shoreline position, sea ice extent, ocean

stratification, non-linear interactions, and radiational forcing (e.g. Woodworth, 2010; Müller et al., 2011; Müller, 2012; Haigh et al., 2020).

In summary, interannual variations and long-term trends in tides have significant implications for flood hazard. Astronomical nodal and perigean cycles can significantly increase flood hazard compared to the long-term average during their positive phases (e.g. Talke et al., 2018), and secular changes in tides driven by non-astronomical factors will either enhance or counteract the increase in flood hazard driven by SLR (e.g. Haigh et al., 2020). Given that the expected frequency of flooding changes year-to-year, considering sea-level rise and tidal non-stationarity together is important to both short and long-term municipal planning and emergency management at the coast. However, as mentioned by Talke et al. (2018), methods for assessing tidally driven interannual variation in extreme sea-level hazard require further development.

In this paper, we describe a new method for estimating tidally driven non-stationarity in extreme still water levels measured at tide gauges using an adaptation of the measurement-based joint probability methods developed by Pugh and Vassie (1978, 1980), Tawn and Vassie (1989), Tawn (1992), and Batstone et al. (2013). We apply and validate our methodology using century-long tide gauge records from the Gulf of Maine coast in the northwest Atlantic Ocean (Fig. 2.1), a region with significant nodal variability and secular trends in tides (Ray, 2006; Ray & Talke, 2019). Under the assumption of stationary storm characteristics, this new quasi-nonstationary joint probability method provides separate statistical treatment of tides and surge and accounts for interannual variation in tides. We use the term “still water level” to convey that the tide gauge-based analyses presented here do not consider wave impacts. Tide gauges

located in wave-sheltered harbors measure the contributions storm surge, tides, and mean sea level to flood level (i.e. the still water level) but exclude waves (Melet et al., 2018; Dodet et al., 2019; Woodworth et al., 2019). Note that in subsequent sections, we use the term "storm tides" for extreme still water levels referenced to the annual mean sea-level.

2.5 Background

2.5.1 Site description

We apply this new quasi-nonstationary joint probability method to estimating extreme still water level recurrence intervals at the three longest running and most complete National Oceanic and Atmospheric Administration (NOAA) tide gauge records within the Gulf of Maine at Boston, Portland, and Eastport (Fig. 2.1). Table 2.1 shows their locations, measurement timespans, and relevant tidal datums. An additional record at St. John, New Brunswick (1893-present) is not included because of significant data gaps and unusual interannual variation in the amplitude of the M_2 tidal constituent after 1980 (Ray & Talke, 2019). In addition to its multiple century-long tide gauge records, the Gulf of Maine's large tide range and known local and regional tidal variation make it an ideal location for applying our statistical method. The region also hosts major cities and sensitive infrastructure that require careful flood risk assessment; for example, Hallegate et al. (2013) ranked Boston, Massachusetts within the top twenty cities globally for modeled flood loss under both present-day and future (2050) scenarios.

The Gulf of Maine coast is vulnerable to flooding from both tropical and extratropical cyclones, but extratropical cyclones have historically been the dominant flooding mechanism, as they are more frequent and more likely to intersect with high tide

due to their often longer durations (e.g. Kirshen et al., 2008; Talke et al., 2018). The total still water level (i.e. not including waves) recorded during a storm, relative to some vertical datum, is called *storm tide* and represents the net impact of meteorological and tidal forcing. Here, we use annual mean sea level (MSL) as the vertical datum, such that storm tide time series do not include SLR. *Storm surge* is the meteorologically forced deviation from the predicted tide, calculated by subtracting the predicted tide from time series of measured storm tide values. Extreme storm surges reach ~1.3 meters in the Gulf (e.g. Talke et al., 2018), and tides are significantly larger. The great diurnal tide range increases northward from 3.1 meters in Boston to ~16 meters in the Bay of Fundy's northern embayments, making tides a primary control on most of the region's extreme coastal flooding events. In Boston, for example, Talke et al. (2018) found that 92 of the top 100 storm events occurring between 1825 and 2018 coincided with a predicted high tide that exceeded modern mean higher high water.

Tides in the Gulf of Maine and Bay of Fundy are unusual in several respects. In addition to the well-known large tidal range, there is a natural resonance frequency in the Gulf near the frequency of the N_2 tide (Garrett, 1972; Godin, 1993). Observed N_2 amplitudes are larger than S_2 amplitudes, although the opposite is true of the theoretical tidal potential; thus, the classic fortnightly spring-neap modulation is relatively weak and is smaller than the monthly modulation induced by M_2/N_2 beating. The strongest astronomical tides during any month therefore occur near times of lunar perigee. Similar to many locations, there are additional modulations at semiannual, 4.4-year, and 18.6-year periods (Haigh et al., 2011; Ray & Merrifield, 2019). The 4.4-year and 18.6-year modulations of the highest predicted tide are moderate at Boston and Portland (roughly

3–4 cm in amplitude) but get much larger (up to 15 cm in amplitude) inside the Bay of Fundy (Ray & Merrifield, 2019; see also Ray & Talke, 2019 for 18.6-year modulations of the M_2 constituent in the Gulf of Maine). The 18.6-year modulation is caused by the lunar nodal cycle, or a precession of the moon's orbital plane around the ecliptic 360° every 18.6 years. The 4.4-year modulation is caused by perigean spring tides coinciding with the winter or summer solstice (when the diurnal tidal contribution is largest) twice per 8.85 years (see Ray & Foster, 2016 for an explanation).

Perhaps owing to the basin resonance being near N_2, Gulf of Maine tides are sensitive to small changes in basin geometry, depth, and friction. Indeed, they display some of the largest secular tidal trends observed anywhere in the world for a regional body of water. Since the early-20th century, the amplitude of the M_2 tidal constituent has steadily increased at an average rate of 0.25 ± 0.04 mm/y at the Boston tide gauge, 0.59 ± 0.04 mm/y at Portland, and 0.77 ± 0.08 mm/y at Eastport (Ray & Talke, 2019). In comparison, average rates of SLR measured at these tide gauges over the same time period (see Tab. 2.1 for exact date range) are 2.83 ± 0.15 mm/y in Boston, 1.88 ± 0.14 mm/y in Portland, and 2.14 ± 0.17 mm/y in Eastport. New tide estimates derived from 19th-century water level measurements show that the M_2 trend began sometime in the late-19th or early-20th century, coincident with the transition to modern rates of SLR (Ray & Talke, 2019). Numerical models show that SLR has only caused part of the observed increase in M_2 amplitude in the Gulf of Maine (e.g. Müller et al., 2011; Greenberg et al., 2012; Pelling & Green, 2013; Schindelegger et al., 2018), suggesting that ocean stratification driven by sea-surface temperature warming has also played a role in the increase (Müller, 2012; Ray & Talke, 2019).

2.5.2 Review of extreme sea level statistical methods

Extreme sea level recurrence intervals can be estimated from data or models. In both cases, an extreme value probability distribution is fit to a set of measured or simulated extreme sea levels assumed to be representative of the possible flood scenarios in a region. Hydrodynamic simulations have the advantage of explicitly including wave impacts and providing spatially continuous flood elevations and flow velocities; however, they are computationally intensive, take time to develop, and as with all models, rely on uncertain parameterizations, bathymetry, and assumptions (e.g. Vousdoukas et al., 2016; Lin et al., 2010). At gauged locations with multi-decadal records, estimating storm tide recurrence intervals from data is a simpler alternative that will be the focus of this paper.

The two most commonly used extreme value distributions are the Generalized Extreme Value distribution (GEV) and the Generalized Pareto Distribution (GPD). The GEV is fit to block maxima data, or the n-largest measurements per some time interval (e.g. the largest event each year), and the GPD is fit to peaks-over-threshold data, or all measurements over some threshold value that defines extremes. The GPD approach is more robust because it uses more available extreme observations (e.g. NERC, 1975; Coles et al., 2001; Tebaldi et al., 2012; Buchanan et al., 2017). In Boston, for example, only 46 of the top 100 storm tides recorded at the NOAA gauge occurred in distinct years. A GEV using annual block maxima would therefore omit more than half of the top-100 events. Compared with the GEV, however, the GPD requires higher data quality and is more difficult to fit automatically because of its sensitivity to the choice of threshold (Coles, 2001; Arns et al., 2013). Storm tide statistics published by NOAA, for example, are derived from GEV fits because choosing a GPD threshold can be subjective,

and NOAA requires a method that can be quickly applied and periodically updated at over 100 gauges (Zervas, 2013). Nonetheless, Talke et al. (2018) found that GEV and GPD fits to Boston extreme storm tides yielded similar recurrence interval estimates.

In meso-to-macrotidal regions, where tides are a primary control on flooding, a joint probability approach that convolves separate tide and surge distributions can capture more extreme storm surges within a temporally limited tide gauge record (e.g. Pugh & Vassie, 1979, 1980). For example, in 63 of the 100 years in Boston's record, the largest storm surge of the year did not coincide with any of the year's top-3 storm tides; thus, a GPD fit to measured Boston storm tides would exclude two-thirds of the largest storm surges (assuming a GPD threshold that was exceeded, on average, three or fewer times per year). The first two published storm tide joint probability methods were the Joint Probability Method (JPM; Pugh & Vassie, 1978, 1980) and the Revised Joint Probability Method (RJPM; Tawn & Vassie, 1989; Tawn, 1992). The JPM separates measured water levels into the predicted tide and a non-tidal residual (measured minus predicted water level at a given time), fits an empirical probability distribution to each component, and obtains the joint storm tide distribution by a convolution of the two component distributions. The RJPM improves upon the JPM by 1) fitting a GEV distribution to extreme non-tidal residual values in order to model events exceeding the observed maximum, and 2) applying an extremal index that accounts for dependence of non-tidal residuals occurring close together in time (the extremal index will be further explained in section 2.6.2).

The primary shortcoming of the JPM and RJPM is the assumed independence between the predicted tide and the non-tidal residual. Storm surge and tides interact;

storm surge increases water depth, and tidal wave speed increases in deeper water (Horsburgh and Wilson, 2007). The non-tidal residual time series of measured minus predicted water level therefore often includes an "illusory" surge during storm events, which is an artifact of the difference in the predicted tide and the phase-shifted tide. Furthermore, the amplitude, timing, and timescale of the surge wave impacts its frictional interaction with tides (Familkhalili et al., 2020).

The Skew Surge Joint Probability Method (SSJPM; Batstone et al., 2013) improves upon the JPM by eliminating the bias introduced by the uncertain timing of the tidal prediction during storm conditions. *Skew surge* is defined as the difference between the maximum measured water level and the predicted high water within each tidal cycle. After accounting for seasonal variation in tides, Williams et al. (2016) found statistical independence between predicted high water and skew surge at 77 Atlantic tide gauges in the United States and Europe. They concluded that this skew surge independence enables a simplified joint probability approach for calculating storm tide recurrence intervals that does not require the inclusion of an empirical relationship between tide and the non-tidal residual to account for tide-surge interaction. The argument is primarily statistical and not dynamical, as the absence of correlation does not indicate the absence of effect; rather, in observational records, natural variability in storm systems dominates over tidally driven variation in surge. We address this issue by using primarily coastal (rather than estuary) locations, such that frictional interaction effects are likely less prominent.

These joint probability methods have lowered bias in storm tide recurrence interval estimates (compared to GPD or GEV fits to data) in regions where tides are large relative to meteorological forcing, particularly for short data series (Dixon & Tawn,

1999; Haigh et al., 2010); however, none has accounted for year-to-year fluctuations or secular trends in tidal properties. In the following sections, we describe a new, quasi-nonstationary (*qn*) modification of the SSJPM called the *qn-SSJPM*, which calculates a separate set of storm tide recurrence intervals for winter and summer storm seasons using that season's known high tides. We fit separate summer and winter distributions because the region's large storm events mostly occur in the winter season (e.g. Talke et al., 2018), while summertime tide levels are larger on average (Ray & Foster, 2016).

2.6 Methods

2.6.1 Tide gauge data processing

At the Eastport, Portland, and Boston NOAA gauges, we use hourly water level data from NOAA, downloaded from the University of Hawaii Sea Level Center database for pre-2016 data (Caldwell et al., 2010) and from NOAA's website for post-2016 data (https://tidesandcurrents.noaa.gov). We remove the annual MSL trend by subtracting a one-year moving average of all hourly water level measurements (following Arns et al., 2013).

We fit a six-minute cubic spline function to the hourly data over the entire length of each tide gauge record (six-minute data are only available from NOAA beginning in 1996) to reduce the peak truncation caused by using hourly records. For example, hourly-based high waters from Boston in 2018 were an average of 4.1 cm lower than 6-minute resolution records. The six-minute spline fit reduces this bias to 0.7 cm. Since the precision of individual, pre-digital measurements varies from 0.015 meters (due to rounding) to 0.05–0.1 meters or more during periods with timing or gauge problems (e.g.

Talke et al., 2018, 2020), this small bias is less than other sources of error. All subsequent calculations use this MSL-adjusted six-minute spline fit to the hourly data.

We estimate the tidal contribution to each water level measurement using the MATLAB-based harmonic analysis program r_t_tide (Pawlowicz et al., 2002; Leffler and Jay, 2009). We calculate tidal constituents independently for each year from a 369-day analysis that includes 67 constituents. The 369-day analysis enables estimation of the semiannual and annual constituents, as well as the seasonal sidelines to M_2 (often called MA_2 and MB_2, but mislabeled H_1 and H_2 in r_t_tide). Since we are interested in the effect of the nodal cycle, no nodal corrections were applied. r_t_tide also applies nodal corrections based on the astronomic potential, rather than the empirically measured and slightly smaller correction observed in practice in the Gulf of Maine (e.g. Ku et al., 1985; Ray & Foster 2016; Ray & Talke, 2019).

We calculate the skew surge parameter by subtracting maximum predicted water level from maximum observed water level within each semidiurnal tidal cycle. Following Williams et al. (2016), we test for statistical independence between predicted high water and the top 1% of skew surge at all sites using the rank-based Kendall's Tau correlation test (Kendall, 1938), where the criteria for significant correlation are $|tau| > 0.1$ and $p < 0.05$. We do not find significant correlation between predicted high water and skew surge at any of the three sites (Appendix B, Tab. S1).

The final inputs into the joint probability analysis are semidiurnal predicted high waters (relative to annual MSL) and their associated skew surges over the length of each tide gauge record. Measured high waters are only used to calculate the declustering coefficient (see equation 6 for calculating the extremal index in section 2.6.2). Prior to

the joint probability analysis, we also divide tides and skew surges into the winter storm season, defined as 31 October to 30 April, and the more quiescent summer season, defined as 1 May to 30 October (Wahl and Chambers, 2015; Thompson et al., 2013). Including 31 October in the winter storm season avoids exclusion of a 1991 hybrid storm (Talke et al., 2018). In all subsequent analyses, we only include seasons where the set of measured water levels is at least 75% complete (Menéndez and Woodworth, 2010; Wahl and Chambers, 2015). Table 2.1 lists the winter and summer seasons omitted at each tide gauge.

2.6.2 Quasi-nonstationary joint probability analysis (qn-SSJPM)

We calculate storm tide exceedance curves for each season, where the expected number of exceedances (i.e. the number of storm tides exceeding a certain level) is equal to the inverse of recurrence interval. Each winter or summer-season storm tide exceedance curve is calculated by convolving probability distributions of that season's predicted high waters and all winter or summer skew surges recorded over the length of the tide gauge record. We model winter and summer extreme skew surge probabilities with a GPD following Batstone et al. (2013). For skew surges x above a threshold μ, the GPD cumulative distribution function $G_{ss}(x)$ takes the form

$$G_{ss}(x) = 1 - \left(1 + \xi \frac{x-\mu}{\sigma}\right)^{-1/\xi} \quad (1)$$

with shape parameter $\xi \neq 0$ and scale parameter $\sigma > 0$. To account for uncertainty in the skew surge GPD, we sample 1,000 pairs of ξ and σ from the covariance matrix of their maximum likelihood estimates with Latin hypercube sampling (Buchanan et al., 2016,

2017). We choose the GPD threshold that defines extreme skew surges by minimizing the root mean square error of GPD exceedances versus empirically-derived storm tide plotting positions (Arns et al., 2013). We calculate plotting positions using the Weibull formula

$$\tilde{F}_{ss}(x_i) = \frac{i}{n+1} \quad (2)$$

where x_i is the ith-largest skews surge, and n is the total number of skew surges. We find that setting the threshold as the 99.7th percentile of skew surges for both the winter and summer seasons minimizes error across all sites, and past studies have used a similarly high threshold (Menéndez and Woodworth, 2010; Arns et al., 2013). This 99.7th percentile threshold samples an average of 1.1 events per season. Following Batstone et al. (2013), we assume there are sufficient observations to use the empirical distribution $\tilde{F}_{ss}(x)$ (i.e. plotting positions; equation 2) for skew surges below the threshold, such that the cumulative distribution function of all skew surges $F_{ss}(x)$ is

$$F_{ss}(x) = \begin{cases} \tilde{F}_{ss}(x), & x < \mu \\ (1 - 0.997) * G_{ss}(x) + 0.997, & x \geq \mu \end{cases} \quad (3)$$

We then calculate the joint cumulative distribution function of storm tides $F_{ST}(z)$ for each season following the SSJPM (Batstone et al., 2013), which assumes that there is an equal probability of a given skew surge occurring at any high tide in a season:

$$F_{ST}(z) = \left[\prod_{t=1}^{N_{HW}} F_{ss}(z - P_t)\right]^{1/N_{HW}} \quad (4)$$

where z is storm tide, P_t is the predicted high water in tidal cycle t, and N_{HW} is the total number of high waters in the season. To account for statistical uncertainty in the skew surge GPD parameters, tides are convolved with all 1,000 skew surge GPDs (F_{ss}). The

50th quantile of the resulting 1,000 storm tide distributions (F_{ST}) represents the central estimate, and the 5th and 95th quantiles provide a 90% uncertainty range. We convert storm tide cumulative probabilities to expected number of exceedances per season *N(z)* by

$$N(z) = [N_{HW} * \theta(z)] * [1 - F_{ST}(z)] \quad (5)$$

where $\theta(z)$ is the extremal index, which effectively reduces the number of high waters per season to the number of independent high waters per season to account for events that span multiple high tides (Leadbetter, 1983; Tawn, 1992). The extremal index is the inverse of mean cluster size (the mean number of storm tides exceeding a certain height that are associated with a single event) and calculated as a function of storm tide, following Ferro and Segers (2003):

$$\frac{1}{\theta(z)} = \frac{2\left[\sum_{i=1}^{E(z)-1}(I(z)_i - 1)\right]^2}{(E(z)-1) * \sum_{i}^{E(z)-1}[(I(z)_i - 1) * (I(z)_i - 2)]} \quad (6)$$

where *E(z)* is the number of measured storm tides exceeding *z*, and *I(z)* is interexceedance time. We find that the extremal index reduces storm tide magnitudes in the 1 to 30-year recurrence interval range; thus, it is likely that these water levels are sometimes exceeded multiple times during a single storm event, while the most extreme water levels with recurrence intervals longer than 30 years are generally independent.

At each site, the final products of the qn-SSJPM calculations include:

1. A storm tide exceedance curve for each summer and winter season in the NOAA record

2. Full-year (i.e. combined winter and summer) storm tide exceedance curves for each year in the NOAA record, calculated by adding the expected number of summer and winter exceedances in a given year for each storm tide height
3. Two time-averaged storm tide exceedance curves (one winter, one summer), calculated using winter or summer tides over the full length of the NOAA record
4. One full-year, time-averaged storm tide exceedance curve

2.7 Results and discussion

2.7.1 qn-SSJPM results

We focus our discussion on winter storm season results because extreme flooding is primarily a winter hazard in the Gulf of Maine. A comparison of the time-averaged qn-SSJPM storm tide exceedance curves for winter, summer, and the full year (Fig. 2.2a) shows that storm tides from the full-year curves are, at most, 1.5 cm higher than winter curves at frequencies below 0.1 expected exceedances/year. Thus, when viewing the full-year curve, it is important to do so with the caveat that summer floods are only a minor contributor to total flood hazard.

Figure 2.2b shows the winter-season annual and time-averaged storm tide exceedance curves for Eastport, Portland, and Boston. The spread among annual curves represents deterministic tidal variability and is thus greatest in Eastport where tide range and nodal cycle amplitude are the largest. As an example, the winter storm tide with 0.01 expected exceedances/year ranges 4.20–4.50 meters in Eastport, 2.56–2.74 meters in Portland, and 2.83–2.99 meters in Boston depending on the tidal properties of the calendar year (note that all storm tides are relative to annual MSL). The 90% uncertainty

region (blue shading in Fig. 2.2b) encompasses both deterministic tidal variability and statistical uncertainty in the skew surge GPD parameters.

We also compare qn-SSJPM storm tide exceedance distributions to a GPD fit to the top 0.3% of storm tides in each record (Fig. 2.2b). This is a common approach for deriving storm tide exceedances (see section 2.5.2), hereafter referred to as GPD_{ST}. We fit GPD_{ST} following the same methods described in section 2.6.2 for fitting the skew surge GPD, using the 99.7^{th} percentile of measured storm tides as the GPD threshold. Uncertainty ranges are larger for the GPD_{ST} distributions than the qn-SSJPM distributions (gray versus blue shaded regions in Fig. 2.2b). Although both incorporate GPD parameter uncertainty, for the qn-SSJPM, the deterministic predicted high water distribution reduces overall uncertainty. In Boston, the GPD_{ST} method estimates significantly higher winter storm tides at exceedance levels < 0.1 compared to the qn-SSJPM. Given the disagreement, we 1) use Monte Carlo simulations to validate the two statistical approaches, 2) compare the Boston qn-SSJPM and GPD_{ST} exceedance curves to a GPD_{ST} exceedance curve fit to an extended, 200-year long record of Boston storm tides (Talke et al., 2018), and 3) test for sensitivity to GPD threshold selection for in each method.

2.7.2 Monte Carlo validation

We compare the validity of the qn-SSJPM and GPD_{ST} methods using Monte Carlo simulations. We create a synthetic 10,000-year time series of winter-season high waters by splicing together the 1921-2018 Boston winter-season predicted high waters 102 times (102 times the 98-year record ≈ 10,000 years) and combining each predicted

high water with a skew surge randomly sampled from the cumulative distribution function of Boston winter skew surges. We treat empirical storm tide exceedances calculated from the synthetic 10,000-year record (equation 2) as the "truth." We then run 1,000 trials of randomly selecting 100 of the 10,000 years and calculating storm tide exceedance distributions based on those 100 years using both the qn-SSJPM and GPD_{ST} methods. We use the 99.7^{th} percentile storm tide and skew surge as GPD thresholds, and for the qn-SSJPM calculation, we only generate a single time-averaged storm tide exceedance distribution for the 100 years (i.e. we do not calculate annual distributions). These simulations test how reliably the two statistical methods can represent flooding conditions over 10,000 years based on a limited "observational" period of 100 years.

In analyzing the results, "estimate" refers to the storm tide-exceedance relationship calculated from a 100-year subsample using the qn-SSJPM or GPD_{ST} methods. "Truth" refers to the empirical storm tide-exceedance relationship calculated from the synthetic 10,000-year record. For each of the 1,000 trials, we determine 1) whether or not the truth falls within the central 67% ranges of storm tide estimates at the 0.1, 0.01, and 0.002 exceedances/year levels for the two methods, and 2) the bias of the estimates, calculated as the difference between the truth and the central (50^{th} quantile) qn-SSJPM and GPD_{ST} storm tide estimates at the 0.1, 0.01, and 0.002 exceedances/year levels.

We find that the truth falls within the central 67% range of estimates 55–65% of the time for the qn-SSJPM and 59–67% of the time for GPD_{ST} (Fig. 2.3a). Both methods' overlap with the truth generally increases at lower exceedance levels because uncertainty range also increases with decreasing expected exceedances. The lower coverage of qn-

SSJPM error ranges indicates that the method's estimate errors are more overconfident than GPD_{ST} estimate errors; however, both the qn-SSJPM and GPD_{ST} have reasonable coverage.

Comparing biases in qn-SSJPM and GPD_{ST} estimates of storm tides at the 0.1, 0.01, and 0.002 exceedances/year levels reveals that qn-SSJPM estimates are more precise and stable (i.e. consistently closer to the truth). Box plots in Figure 2.3b show each method's biases for all 1,000 trials. The interquartile ranges increasing (i.e. the boxes getting larger) at lower exceedance levels reflects the expected trend of increasing instability (i.e. variability) in estimated exceedances at lower exceedance levels for a given record length (e.g. Haigh et al., 2010). Mean bias is close to zero for both methods at all three exceedance levels; however, for storm tides at the 0.01 and 0.002 exceedances/year levels, both the interquartile range and total range in biases are significantly narrower for qn-SSJPM estimates than for GPD_{ST} estimates. This result indicates that for a 100-year observational record, both methods will, on average, provide accurate storm tide estimates between the 0.1 and 0.002 exceedances/year levels; however, GPD_{ST} estimates of storm tides with recurrence intervals nearing the record length (e.g. the storm tide with a 100-year recurrence interval or 0.01 expected exceedances/year for a 100-year-long record), are more susceptible to being biased by the largest few events within the observational period. This finding is consistent with past studies that have shown GPD and GEV fits to observed storm tides (often called "direct methods" of estimation) are more unstable to historical outlier events than joint probability distributions that incorporate large historical storm surges not necessarily coinciding with high tides (e.g. Tawn and Vassie, 1989; Tawn, 1992; Haigh et al., 2010).

This instability to historical outliers partially explains the disagreement between the qn-SSJPM and GPD_{ST} curves for Boston (Fig. 2.2b). Boston's highest three recorded flood events all occurred in years with unusually large tides (Talke et al., 2018). For example, the Blizzard of 1978 (the storm tide of record), happened to coincide with the year that, on average, had the largest-magnitude high waters over the past century (represented by the right-most blue curve in Fig. 2.2b and highlighted with a red arrow in Fig. 2.5). Thus, the GPD_{ST} method in part overestimates Boston flood hazard because it does not account the Blizzard of 1978's 3.05-meter flood having had a lower probability of occurrence during any of the other 97 winters of record.

2.7.3 Extended Boston record and GPD threshold sensitivity

Comparing the Boston qn-SSJPM and GPD_{ST} winter storm tide exceedance curves (Fig. 2.2b) to exceedance curves fit to the Talke et al. (2018) extended 200-year storm tide record also highlights the stability of the qn-SSJPM relative to the GPD_{ST} method. Gray curves in Figure 2.4 show five GPD_{ST} fits to the 1921–2018 NOAA record using five different GPD thresholds, ranging 2.25 to 2.44 meters (the 99.5^{th} to 99.9^{th} percentiles of measured winter storm tides; Appendix B, Tab. S2). For the 100-year NOAA record, the five exceedance curves begin to diverge below the 0.03 exceedances/year level, demonstrating the sensitivity of the GPD_{ST} method to threshold selection. The red shaded region in Figure 2.4 shows GPD_{ST} curves fit to the extended 1825–2018 Boston record (un-bias corrected Data Set S3 from Talke et al., 2018) using both a 2.40-meter threshold (the value used by Talke et al., 2018) and a 2.31-meter threshold (the value used in Fig. 2.2b that provides the best match to empirical

exceedances). In contrast to the NOAA-record curves, the narrowness of the red shaded region indicates that the longer, 200-year dataset makes the GPD_{ST} method stable down through the 0.002 exceedances/year level.

The blue shaded region in Figure 2.4 shows the qn-SSJPM fit to the NOAA record using five different thresholds for the GPD fit to skew surges (99.5^{th} through 99.9^{th} percentiles; Appendix B, Tab. S2). The small variability among the five curves (i.e. the narrowness of the blue shaded region) shows that with the shorter NOAA record, the qn-SSJPM can achieve the same stability with respect to GPD threshold selection as the GPD_{ST} fit to the 200-year record. Finally, the agreement at low exceedance levels between the qn-SSJPM and 200-year exceedance curves is further evidence that the qn-SSJPM provides a more reliable characterization of extreme storm tide frequencies than the GPD_{ST} method based on the 100-year NOAA record.

2.7.4 Interannual variation in storm tide frequency

Interannual variation in tides forces changes in flood hazard on annual-to-decadal timescales that should be considered in coastal management practices tied to storm tide frequency estimates. We quantify the tidal modulation of flood hazard over the past century in Eastport, Portland, and Boston using the annual time series of winter storm season storm tides at the 0.01 exceedances/year level (hereafter referred to as $ST_{0.01}$) taken from the qn-SSJPM curves (Fig. 2.5). To represent the three dominant sources of interannual tidal variability in the region (see Ray & Foster, 2016), we fit a harmonic function to the time series with an 18.6-year period, a 4.4-year period, and a linear trend, where $ST_{0.01}$ values are relative to annual MSL, so the linear trend is the increase in tides

above SLR. The ranges (twice the amplitudes) of the 18.6 and 4.4-year harmonics represent the magnitudes of the tidal cycles' forcing of flood hazard.

Table 2.2 compares 18.6 and 4.4-year modulations of $ST_{0.01}$ and of the highest predicted tide (the highest tide in a 6-month interval), which are computed directly from harmonic constants at the gauges. The 18.6 and 4.4-year cycles' forcing of $ST_{0.01}$ is perhaps smaller than that of the highest predicted tide because $ST_{0.01}$ is calculated from observations rather than predictions. Observed water level data include atmospheric effects, which introduce variability that could interfere with tidal modulations. The exclusion of summer-season tides in the winter $ST_{0.01}$ values also likely reduces 4.4-year periodicity in predicted water levels (e.g. Talke et al., 2018). Finally, Peng et al. (2019) showed that the 18.6-year modulation of tides is greater for more extreme high waters (for example, the modulation of monthly maximum high waters is greater than that of monthly 99^{the} percentile high waters). Similarly, modulation of $ST_{0.01}$ potentially reflects less extreme tidal levels than what would be obtained using the 6-month maximum.

The secular increase in tides observed in the M_2 tidal constituent (e.g. Ray & Talke, 2019) has driven roughly a 0.6 mm/y increase in $ST_{0.01}$ in Eastport and Portland. In Boston, however, there is a slight negative linear trend in $ST_{0.01}$ of -0.08 mm/y. Thus, the increase in tides has had a minimal decadal-timescale impact on $ST_{0.01}$ compared to other forcings; however, in Eastport and Portland, the total secular increase in $ST_{0.01}$ over the length of the tide gauge record is comparable to decadal nodal variability. There is likely to be a future increase in high water levels with SLR (Greenburg et al., 2012; Pelling & Green, 2013; Schindelegger et al., 2018) and increasing tidal range (Greenberg et al., 2012), but there are no detailed projections for Gulf of Maine tides that consider

additional forcing mechanisms, such as changes in stratification and flooding (Haigh et al., 2020).

The significance of the 4.4 and 18.6-year tidal modulations of $ST_{0.01}$ can best be illustrated by converting the tidal cycle forcing ranges to rates and comparing them to rates of SLR. In Eastport, for example, the average range in 18.6-year forcing of $ST_{0.01}$ is 126 mm (Fig. 2.5). The 18.6-year forcing can be positive or negative, so over any half nodal period in Eastport, the average rate of nodal forcing of $ST_{0.01}$ is ±126 mm per 9.3 years, or ±13.5 mm/year. Applying the same calculation to Portland and Boston, the average 18.6-year tidal forcing rates are ±4.0 mm/year and ±5.9 mm/year, respectively. 4.4-year tidal forcing rates are a slower ±3.0 mm/year in Eastport and Boston and ±4.0 mm/year in Portland. In practice, however, interannual variation in winter MSL (which has historically been on the order of tens of mm) would drown out this shorter-period 4.4-year tidal modulation.

Figure 2.6 provides a visualization of the impact of 18.6-year forcing in the context of SLR. On decadal timescales, the natural variability in $ST_{0.01}$ (and therefore flood hazard) driven by the nodal cycle at the three Gulf of Maine sites has historically been larger than non-stationarity driven by the ~100-year average rate of SLR (black triangles versus asterisks in Fig. 2.6). In the future, even as SLR accelerates to equal or exceed rates of $ST_{0.01}$ nodal forcing, the nodal cycle will continue to force significant decadal-scale variability in the rate that flood hazard will increase. We illustrate this effect through 2100 by adding the $ST_{0.01}$ nodal forcing rate to the projected mean rate of SLR over 9.3-year periods when nodal forcing will be trending positively (i.e. moving from a minimum toward a maximum). Over 9.3-year periods when the nodal cycle will

be trending negatively, we subtract nodal forcing from projected SLR. We use Kopp et al. (2014) probabilistic local SLR projections, but we modify the ice sheet contributions by replacing the Church et al. (2013) likely ranges with Oppenheimer et al. (2019) likely ranges.

The nodal cycle is currently in its negative phase in the Gulf, and until it reaches its minimum in 2025, negative nodal forcing will counteract the SLR-induced increase in flood hazard. Between 2025 and 2034 (and in all decades when the nodal cycle is moving from a minimum to a maximum), however, positive nodal forcing will accelerate the flood hazard increase. Thus, it is critical to consider SLR and nodal cycle forcing together in planning for the transition to chronic flooding that will be driven by SLR in many coastal regions over the next century (e.g. Ray & Foster, 2016; Buchanan et al., 2017; Kopp et al., 2017; Talke et al., 2018; Oppenheimer et al., 2019).

2.7.5 Limitations

We demonstrate that the qn-SSJPM provides more precise and stable storm tide exceedance estimates than the commonly used GPD fit to measured storm tides. However, there are sources of uncertainty in the method, and there are additional forcings of interannual storm tide variation that we do not account for. The skew surge GPD is a significant source of uncertainty, as GPD parameters are sensitive to both the choice of threshold (e.g. Coles, 2001; Arns et al., 2013) and the largest observed skew surge values (e.g. Tawn and Vassie, 1989; Tawn, 1992; Haigh et al., 2010). We show that the qn-SSJPM is stable against a range of skew surge GPD thresholds for Boston through the 0.002 exceedances/year level (Fig. 2.4), and this should always be tested. Furthermore,

the accuracy of skew surge values depends on the accuracy of tidal predictions. The r_t_tide software does not include minor constituents (for example, our Boston r_t_tide predictions use 67 constituents, compared to the 108 used by Ray and Foster, 2016), and our calculations do not include tide prediction errors. The errors, however, are small; for example, M_2 amplitude errors are on the order of 0.1% (~0.001–0.003 meters).

The qn-SSJPM also does not incorporate climatic variability that may impact storm tide hazard relative to annual MSL. For example, the North Atlantic Oscillation drives interannual variation in New England sea levels via northeasterly wind stress anomalies on the upper ocean (Goddard et al., 2015). In the future, increasing sea surface temperatures and changing atmospheric circulation patterns may also drive changes in storm intensity and frequency, but there is low confidence in site-specific projections of future storm behavior (e.g. Knutson et al., 2010; Emanuel et al., 2013), making it difficult to incorporate storm non-stationarity into flood hazard assessment.

Finally, the qn-SSJPM does not consider the impact of wave processes on flood hazard and is therefore most suitable for wave-sheltered harbors and embayments. During flood events, wave set-up elevates the time-averaged water level, and wave run-up periodically further raises water level (Stockdon et al., 2006; O'Grady et al., 2019). These processes must be included for hazard analyses to be reliable at wave-exposed coastlines; for example, Lambert et al. (2020) demonstrate that neglecting waves can lead to overestimating the time it will take for sea-level rise to double the frequency of a given extreme water level. Furthermore, our analysis does not explicitly account for water level oscillations just below wind-wave frequencies in the infragravity spectrum, generally defined between 0.04 and 0.004 Hz (Bertin et al., 2018). Infragravity waves are not only

an important component of wave-induced run-up along open coasts (Stockdon et al., 2006), but can also contribute to flooding in harbors, particularly when amplified by resonance (e.g. Rabinovich, 2010; Bertin et al., 2015).

2.8 Conclusions

We present a new quasi-nonstationary skew surge joint probability method for calculating storm tide exceedances and apply it along the Gulf of Maine coast, where tides are large and vary year-to-year. In addition to providing separate statistical treatment of tides and surge, the qn-SSJPM calculates distinct annual storm tide exceedance curves that account for interannual variation in tides. Each year's curve is a convolution of 1) predicted high water probabilities, which are known based on that year's tide predictions, and 2) skew surge probabilities determined from a GPD fit to all skew surges recorded over the length of a tide gauge record.

We use a Monte Carlo validation and a GPD threshold sensitivity test to compare the qn-SSJPM to the commonly used method of fitting a GPD to times series of measured storm tides. We find that the qn-SSJPM provides more precise and stable storm tide frequency estimates because it is less susceptible to being biased by the largest few events within the observational period, and it is more stable with respect to GPD threshold selection. We also show that in Boston, qn-SSJPM-derived storm tide frequency estimates based on the 100-year NOAA record match those based on the extended, 200-year Talke et al. (2018) record.

At all three Gulf of Maine sites, we find that interannual variation in tides significantly impacts design-relevant flood levels, such as winter storm tides at the 0.01

exceedances/year level ($ST_{0.01}$). The 18.6-year nodal cycle forces decadal oscillations in $ST_{0.01}$ at a rate of 13.5 mm/year in Eastport, 4.0 mm/year in Portland, and 5.9 mm/year in Boston. In comparison, the average historical rate of local SLR over the past century has been between 1.89 and 2.86 mm/year at the three sites. Nodal forcing is currently counteracting the SLR-induced increase in flood hazard; however, in 2025, the nodal cycle will reach a minimum and then begin accelerating flood hazard increase as it moves toward its maximum phase over the subsequent decade.

SLR is driving a transition to severe chronic flooding in many coastal regions (e.g. Oppenheimer et al., 2019). Flooding becomes severe when water elevations cross thresholds defined by local topography and flood defense structures, and the nodal cycle entering a positive phase may drive flood heights above these thresholds sooner than SLR would alone. Thus, considering tidal non-stationarity and SLR together is key to long-term municipal planning and emergency management along meso-to-macrotidal coastlines.

2.9 Acknowledgments and Data

H.E.B. was supported by the National Aeronautics and Space Administration (Award NNX16AO24H). We thank two anonymous reviewers whose comments improved the manuscript. Datasets for this research are available in these in-text citation references: Caldwell et al. (2010), Talke et al. (2018), and https://tidesandcurrents.noaa.gov. All of the code we used to produce results is available at https://doi.org/10.5281/zenodo.3898657 with a Creative Commons Attribution 4.0 International license.

Table 2.1. Gulf of Maine NOAA tide gauge station info. The two right-most columns show winter and summer seasons omitted from the qn-SSJPM statistical analysis due to missing more than 25% of water level measurements. Two years are listed for each omitted winter season because we define the season as 31 October through 30 April of the following year. Note that all records extend to the present, but we only use data through 2019 in our calculations.

Station; NOAA station no.	**Approx. location**	**Mean higher high water (m)[a]**	**Great diurnal range (m)[a]**	**Time-span**	**Omitted winter seasons (< 75% complete)**	**Omitted summer seasons (< 75% complete)**
Eastport, ME 8410140	44°54.2'N 66°59.1'W	2.916	5.874	1929–2019	1957/1958, 1962/1963, 1970/1971, 1971/1972, 1974/1975, 1975/1976, 1976/1977, 1977/1978, 1995/1996, 1998/1999	1929, 1957, 1958, 1963, 1971, 1974, 1976, 1978, 1980
Portland, ME 8418150	43°39.3'N 70°14.8'W	1.513	3.019	1910–2019	1910/1911, 1911/1912, 1933/1934, 1945/1946, 1960/1961	1910, 1911, 1956, 1961, 1970, 1971, 1990
Boston, MA 8443970	42°21.2'N 71°3.0'W	1.545	3.131	1921–2019	1944/1945	1921

[a] Tidal datums are relative to 1983-2001 mean sea level

Table 2.2. Ranges of 18.6 and 4.4-year tidal cycle modulations of the storm tides at the 0.01 exceedances/year level ($ST_{0.01}$) and the highest predicted tide.

	18.6-year modulation range (mm)		**Quasi 4.4-year modulation range (mm)**	
	$ST_{0.01}$	**Highest predicted tide**	**$ST_{0.01}$**	**Highest predicted tide**
Eastport	126	196	28	78
Portland	37	66	37	68
Boston	55	72	28	62

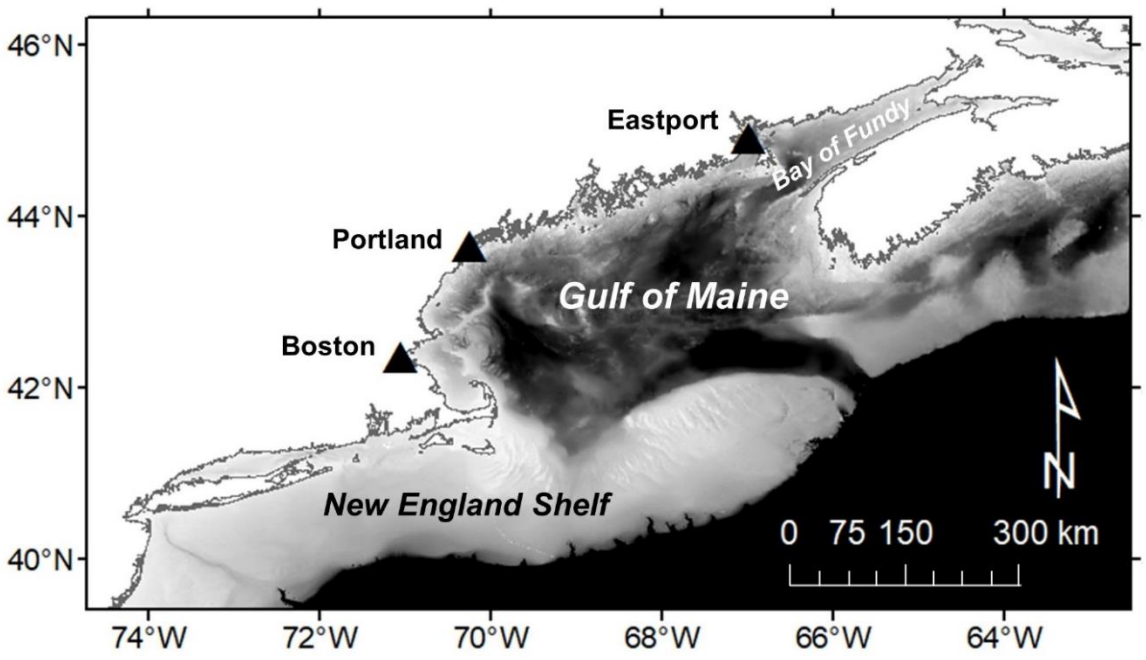

Figure 2.1. Gulf of Maine site map, including gauge locations mentioned in the text.

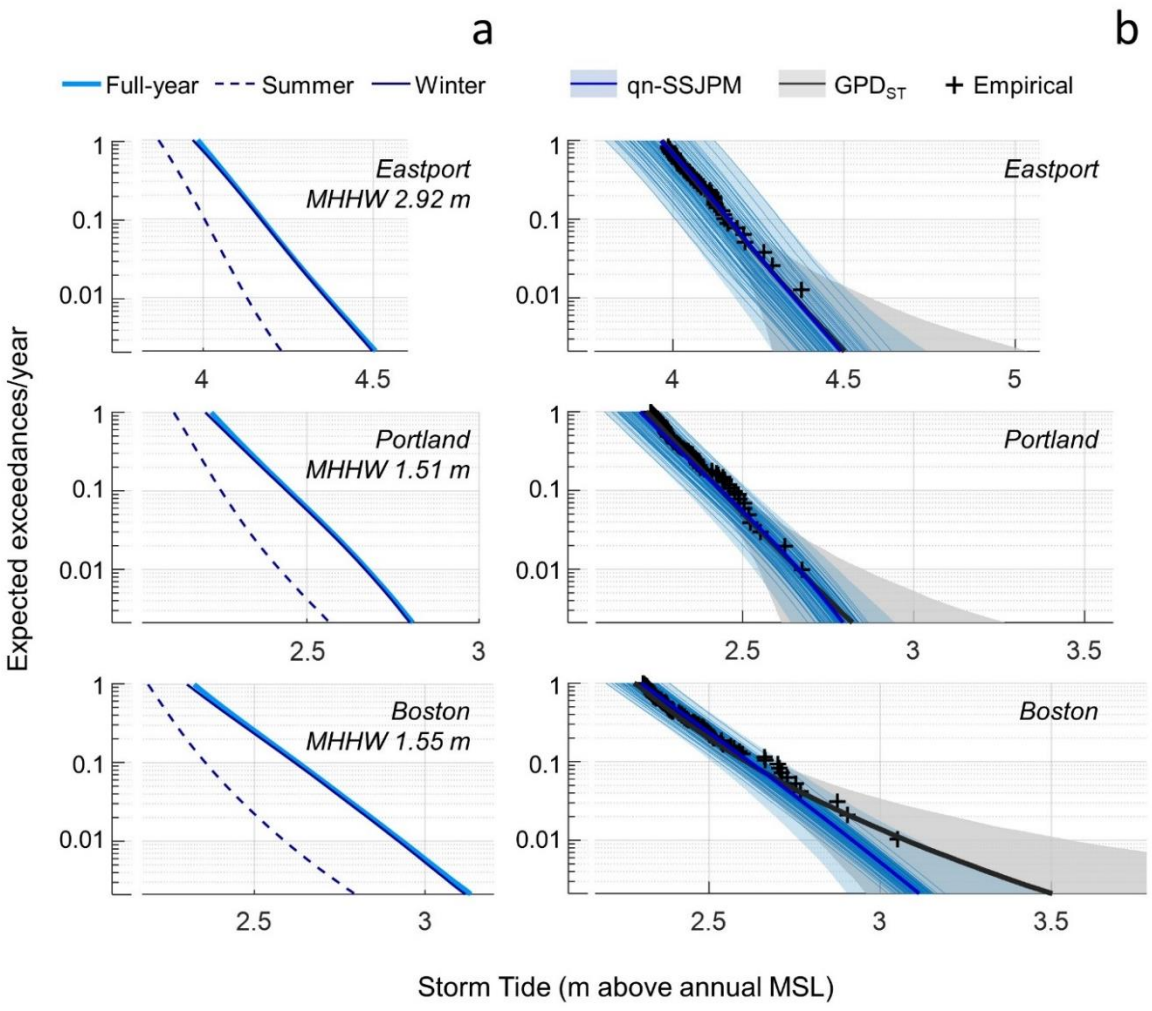

Figure 2.2. Gulf of Maine storm tide exceedance curves. *(a)* Seasonality of flood hazard. Historical time-averaged qn-SSJPM storm tide exceedance curves are compared for the full year (thick solid line), summer season (dashed line), and winter season (thin solid line). *(b)* Comparison of winter-season storm tide exceedance curves for the qn-SSJPM and a GPD fit to measured storm tides (GPD_{ST}). Thin blue curves show qn-SSJPM-derived curves for each winter storm season in the tide gauge record, and bold blue curves are the time-averaged qn-SSJPM curves based on the entire tide gauge record. Black curves are a GPD_{ST} fit to the top 0.3% of storm tides in each tide gauge record, and + signs are empirical exceedances (see equation 2). Lines represent central estimates (50^{th} quantile), and filled regions show the 90% uncertainty range (5^{th}–95^{th} quantiles) for each method.

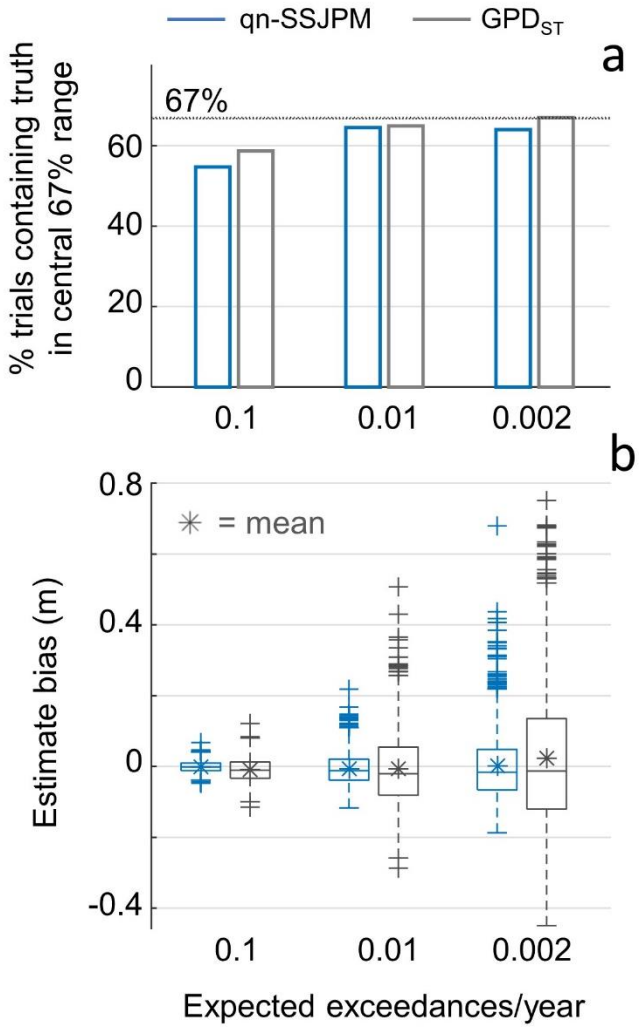

Figure 2.3. Validation results. *(a)* Percent of the 1,000 validation trials that contain the truth (empirical value) within the central 67% range of storm tide estimates at the 0.1, 0.01, and 0.002 exceedances/year levels for the qn-SSJPM method (blue) and the GPD_{ST} method (gray). *(b)* Box plot showing the distribution of qn-SSJPM and GPD_{ST} biases for the 1,000 validation trials at the 0.1, 0.01, and 0.002 exceedances/year levels. Biases are calculated as the difference between the truth (based on the empirical distribution calculated from the 10,000-year synthetic record) and the central qn-SSJPM estimates (blue) or GPD_{ST} estimates (gray). Central marker is the median (with the * symbol showing the mean), and bottom and top box edges are the 25th and 75th quartiles. Values plotted as outliers (+ markers) fall outside the central 99.3% range.

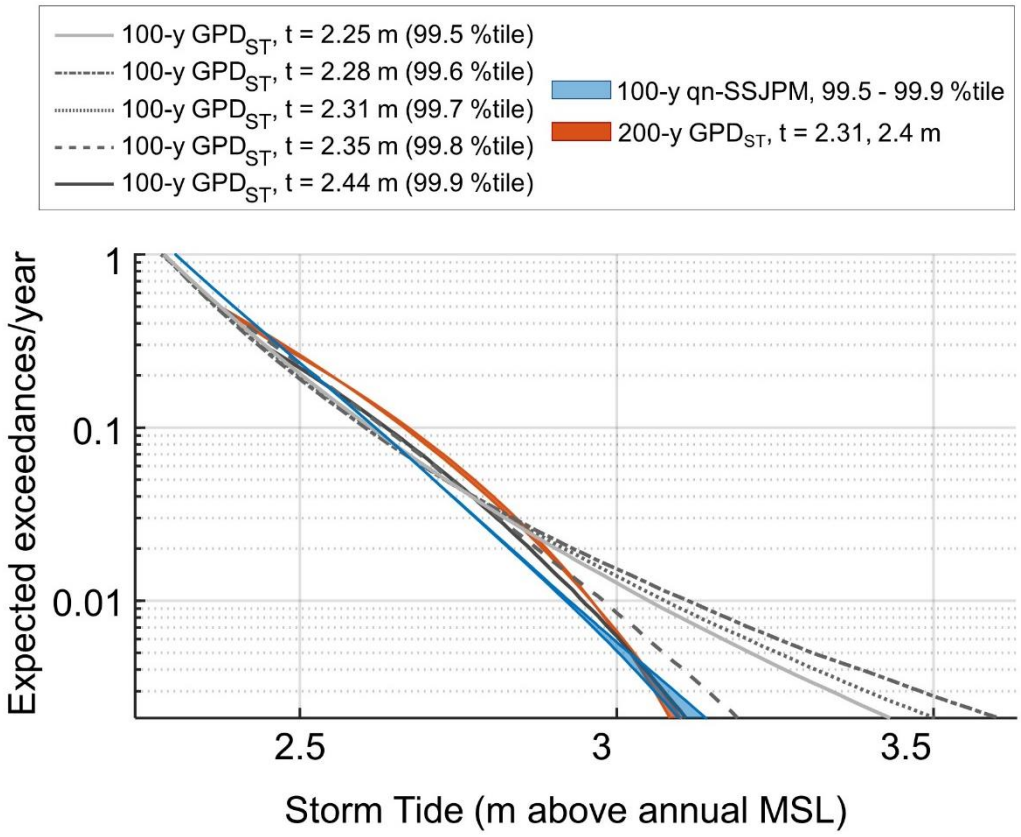

Figure 2.4. Sensitivity of Boston winter storm tide exceedance curves to GPD threshold selection and comparison to the extended, 200-year Talke et al. (2018) record. The five gray storm tide exceedance curves are calculated using a GPD fit to measure storm tides in the 100-year NOAA record (GPD_{ST} method) with the threshold set as the 99.5th, 99.6th, 99.7th, 99.8th, and 99.9th percentile of measured storm tides. The red shaded region shows GPD_{ST} exceedance curves fit to the 200-year Talke et al. (2018) record using a 2.31-meter threshold (same as Fig. 2b) and a 2.4-meter threshold (value used by Talke et al.). The blue shaded region shows five qn-SSJPM exceedance curves fit to the 100-year NOAA record, with the skew surge GPD threshold set as the same five percentiles of skew surges (99.5th–99.9th percentiles).

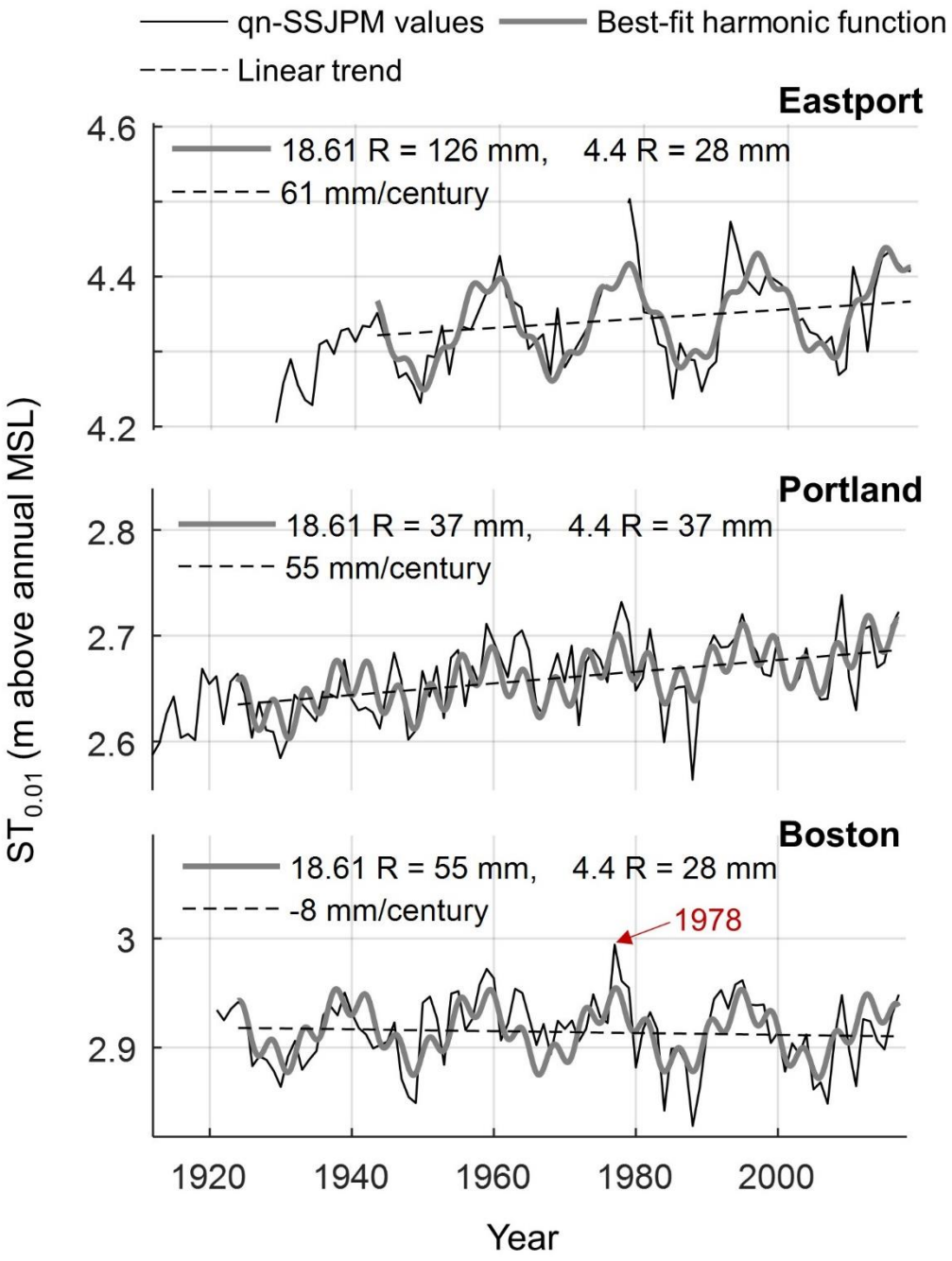

Figure 2.5. Interannual variation in the winter storm tides at the 0.01 exceedances/year level ($ST_{0.01}$). Time series of qn-SSJPM-derived annual $ST_{0.01}$ values (black line) with a least squares best-fit harmonic function that represents the region's dominant tidal forcings (gray curve), which includes an 18.6-year period, a 4.4-year period, and a linear trend. Legends show the ranges (i.e. double the amplitude) of the best-fit sinusoids and the slopes of the linear trends. Note the gap in the Eastport $ST_{0.01}$ time series where winter seasons were omitted due to less than 75% data completeness (see Tab. 2.1).

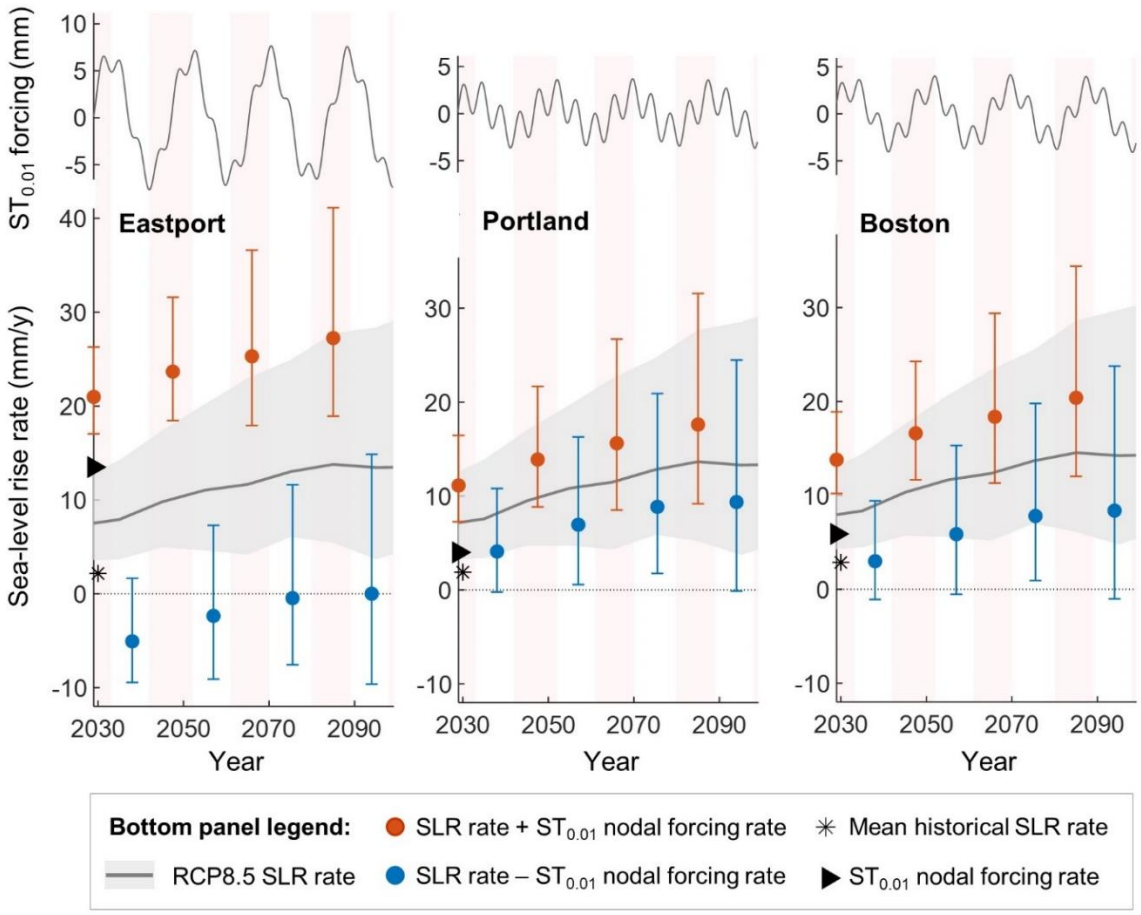

Figure 2.6. Joint impact of tidal forcing and sea-level rise on future flood hazard increase. *(Top panel)* 18.6 and 4.4-year components of the best-fit harmonic function to the winter $ST_{0.01}$ time series from Fig. 5. *(Bottom panel)* Gray curves show projected rates of local RCP8.5 SLR modified from Kopp et al. (2014) (line = 50th quantile of samples, shading = central 90% range). Over 9.3-year-intervals where the nodal cycle is moving from a minimum to a maximum (indicated by red shading), the average nodal forcing rate (black triangle on y-axis) is added to the average projected rate of SLR over the same 9.3 years (red circles, with bars representing SLR uncertainty). Over intervals when the nodal cycle is trending negatively, nodal forcing is subtracted from the rate of SLR (blue circles and bars). The historical rate of SLR over the past century is also shown for reference (black asterisk on the y-axis).

CHAPTER 3

SOURCES, MECHANISMS, AND TIMESCALES OF SEDIMENT OF SEDIMENT DELIVERY TO A NEW ENGLAND SALT MARSH

3.1 Abstract

The availability and delivery of an external clastic sediment source is a key factor in determining salt marsh resilience to future sea level rise. However, information on sources, mechanisms, and timescales of sediment delivery are lacking for most marsh systems, particularly those in wave-protected mesotidal estuaries. Here we show that marine sediment mobilized and delivered during coastal storms is a primary source to the North and South River, a mesotidal bar-built estuary typical to New England. On the marsh platform, deposition rates, clastic content, and dilution of fluvially-sourced contaminated sediment by marine material all increase down-estuary toward the estuary inlet, consistent with a dominantly marine-derived sediment source. Marsh clastic deposition rates are also highest in the storm season. We observe that periods of elevated turbidity in channels and over the marsh are concurrent with storm surge and high wave activity offshore, rather than with high river discharge. Flood tide turbidity also exceeds ebb tide turbidity during these storm events. Timescales of storm-driven marine sediment delivery range from 2.5 days (5 tide cycles) to 2 weeks, depending on location within the estuary; therefore the phasing of storm surge and wave events with the spring-neap cycle determines how effectively post-event suspended sediment is delivered to the marsh platform. This study reveals that sediment supply and the associated resilience of New England mesotidal salt marshes involves the interplay of coastal and estuarine processes,

underscoring the importance of looking both up- and downstream to identify key drivers of environmental change.

3.2 Plain Language Summary

Salt marshes need an external supply of mineral sediment to survive. Understanding sources and physical mechanisms of sediment delivery is therefore critical to effective salt marsh management. Sediment can be sourced from land and delivered to marshes through rivers, or it can come from the ocean during high tides and storm surges; however, the relative importance of these sediment sources is uncertain for most marshes. Here, we show that ocean sediment mobilized and delivered during coastal storms is the primary source to the North/South River estuary, a typical New England salt marsh system. Within the marsh platform, mineral sediment is most abundant near the ocean, and we find little river-derived sediment beyond the most landward region of the estuary. In estuary channels, we also observe the greatest amounts of suspended sediment when incoming tides flood the estuary during coastal storms. In contrast, we do not observe elevated suspended sediment when river flow is high. Our work shows that coastal and marine processes influence sediment supply and the associated resilience of New England salt marshes, underscoring the importance of looking both up- and downstream to identify key drivers of environmental change.

3.3 Introduction

Tidal salt marshes are critical protectors of the coastal; they buffer against erosion and flooding (Möller et al., 2014), sequester carbon (Chmura et al., 2003), provide habitat to juvenile species and migratory birds (Boesch & Turner, 1984; Hughes, 2004), and filter pollutants and excess nutrients (Sousa et al., 2010). Coastal wetland maintenance involves complex biophysical feedbacks between clastic (i.e. inorganic) sediment supply, nutrients, plant growth, and flooding (Deegan et al., 2012; Kirwan & Megonigal, 2013). Deposition of clastic sediment in the form of clays, silts, and sands allows marshes to accrete faster than would be possible via in-situ organic production alone; thus, the availability and delivery of clastic sediment is a key factor in determining salt marsh resilience to erosion and future sea level rise (e.g. Donatelli et al., 2018; Fagherazzi et al., 2012; Ganju et al., 2017; Ganju, 2019; Kirwan et al., 2010; Liu et al., 2021; Morris et al., 2016; Redfield, 1972).

Clastic sediment can be supplied by external fluvial and marine sources, or it can be derived internally from erosion of tidal flats and the marsh platform. In microtidal embayments (tide range < 2 m) where the marsh edge is exposed to open water, storm surge and waves are dominant agents of erosion of tidal flat and marsh edge sediment and subsequent delivery to the marsh platform (Cahoon, 2006; Fagherazzi & Priestas, 2010; Fagherazzi et al., 2013; Mariotti & Fagherazzi, 2013; Reed, 1989; Turner et al., 2006). In contrast, wave-protected mesotidal marshes (tide range 2-4 m), which account for ~25% of marshes globally, fringe dendritic creek networks rather than large embayments; thus tides, fluvial processes, and channel morphology are additional important controls on sediment distribution (e.g. Fitzgerald et al., 2020a; Hopkinson et al., 2018; Leonard,

1997; Reed, 1999; Ward, 2004). In these mesotidal estuaries, uncertainty around sources, mechanisms, pathways, and timescales of sediment delivery through estuary channels and onto the marsh platform is widely recognized as an impediment to assessing marsh resilience to future sea level rise (Fagherazzi et al., 2018).

Sediment sourcing and delivery mechanisms are especially uncertain in mesotidal Northeastern United States marshes given the heterogeneity of the region's post-glacial coastline (e.g., FitzGerald & van Heteren, 1999; Woodruff et al., 2021) and the substantial history of human impacts, including damming, deforestation (e.g. Foster & Motzkin, 2003), and coastal construction (e.g. groins, jetties, bulkheads, and revetments). The few existing studies of sediment sourcing to Northeastern marshes have widely ranging conclusions. Kirwan et al. (2011) and Braswell et al. (2020) proposed that deforestation by European colonists provided an upland sediment source that drove Northeastern marsh expansion in the 18th and 19th centuries. At the Webhannet River Estuary in Maine, Ward (2004) also concluded that the uplands were a significant modern-day sediment source based on observations of higher suspended sediment concentrations in the upper estuary channel than in the lower estuary.

In contrast, at the Plum Island Sound estuary in northern Massachusetts, Hopkinson et al. (2018) found that the watershed only supplied 8% of the clastic sediment required for the marsh to build elevation at the rate of present-day sea level rise. Marsh edge erosion supplied an additional 31%. Thus, they inferred that sediment input from tidal flat resuspension and marine environments were likely the most significant sources. Most recently, Fitzgerald et al. (2020a, 2020b) found that sediment-laden ice rafted onto the marsh surface during the winter storm season was a significant source to

Great Marsh in Barnstable, MA (for example, a January 2018 Nor'easter delivered the equivalent of 15 years of clastic sediment).

Here, we combine sub-hourly turbidity observations with measurements of seasonal and centennial-timescale marsh platform clastic deposition to the mesotidal North and South River estuaries in Marshfield and Scituate, Massachusetts. Primary study goals include assessing: 1) the relative significance of marine, fluvial, and internally derived sediment sources; 2) the mechanisms and timescales of sediment delivery to the estuary; and 3) the role of tides and storms in modulating sediment delivery to the tidal creek network and marsh platform. We hypothesize that marine sediment is the primary clastic sediment source to the North and South River estuaries. New England watersheds have relatively low sediment yields (e.g. Meade, 1969; Millman & Farnsworth, 2011; Ralston et al., 2021; Weston, 2014), while high erosion rates along the coastline adjacent to the North and South Rivers (Theiler et al., 2013; U.S. Air Force, 2014) likely provide an important yet to date understudied sediment source. Moreover, we hypothesize that coastal storms combined with high spring tides are the most significant mechanisms of sediment delivery to the system because they drive the greatest flow velocities and water depths in the channel and over the marsh platform.

3.4 Methods

3.4.1 Site description

The North/South River system is ideal for investigating marsh sediment sourcing in New England (Fig. 3.1). The paired estuaries are connected to Massachusetts Bay via a shared barrier beach inlet. The 1898 Portland Gale shifted the inlet 5.6 km to the north (to

its present location) such that the North River estuary was shortened by over 25% (Johnson, 1925), and the elevation of mean high water instantaneously increased 25 cm in the vicinity of the new inlet (Freitas & Ball, 1995; Yellen et al., in prep.). In an accompanying paper, Yellen et al. (in prep.) find that marsh sediment deposition rates near the new inlet have been roughly double the rate of local relative sea level rise since 1898. Some abundant sediment source thus enabled the marsh to rapidly build elevation in response to a sudden increase in high water elevation.

The North River and South River channels are well-defined and constrained by high marsh platform for most of their courses. Channel widths are approximately 100 meters within their seaward reaches and narrow up-estuary. Average thalweg depth is 5 m in the main channel. In the system's current configuration, the North River estuary has an 11-km salinity reach, a 20-km tidal reach (Fig. 3.1), and contains 6.1 km^2 of tidal marsh (USFWS, 2013). The South River estuary is shallower and shorter, with thalweg depths of 2-4 m, 5.2 km^2 of tidal marsh, an 11-km salinity reach, and a 13-km tidal reach. The system has partially progressive, semidiurnal tides. Tide range at the inlet ranges 2 to 3.5 m (Kranenburg et al., 2019), and tidal attenuation results in the elevation of mean high water (MHW) decreasing by roughly 3.5 cm/km up-estuary (Yellen et al., in prep.).

The coastline adjacent to the North and South River estuaries is eroding. Shoreline recession rates range from 0.1 to 0.5 m/year over the past century (Theiler et al., 2013), and approximately 1,150 m^3 of sediment per year has been eroding from Fourth Cliff, the 0.5 km of coastline south of the North/South River inlet (Fig. 3.1; U.S. Air Force, 2014). On the upland side, the relatively small 210 km^2 North River watershed is 38% urbanized (NLCD classes 21-24), with 20% water and wetland cover and 42%

forest cover (USGS, 2016). The even smaller, 60 km^2 South River watershed is less urbanized (29%) with greater forest and wetland cover (64% and 22%, respectively).

In the estuary, low salt marsh areas are dominated by *Spartina alterniflora*, and high salt marsh is primarily *Spartina patens.* The tidal freshwater marsh is primarily *Typha angustifolia*. The marsh platform is also generally lower elevation in the North River than the South River. Marsh inundation depths are 30-80 cm at mean high water in the North River and 20-50 cm in the South River (Yellen et al., in prep.). Sediment deposition rates vary throughout the estuary. In the South River salt marsh, 100-year average deposition rates are generally equivalent to the 100-year average sea level rise rate at the Boston NOAA tide gauge (2.9 mm/year). In the North River salt marsh, 100-year average deposition rates increase to between 5 and 10 mm/year (Yellen et al., in prep.).

Both tropical and extratropical cyclones impact the region, and the most extreme storm surges reach 1.3 meters (Talke et al., 2018). Extratropical cyclones have historically been the dominant flooding mechanism, as they are more frequent (25-30 tracks crossing northern New England per year; Fitzgerald et al., 2020a) and have longer durations more likely to intersect with high tides (e.g. Baranes et al., 2020; Kirshen et al., 2008; Talke et al., 2018). The 1898 Portland Gale, which drove one of the top-ten storm tides recorded in Boston since 1825 (2.8 m, with a 1.2-m skew surge; Talke et al., 2018) and moved the North/South River inlet 5.6 km to the north, likely represents the storm of record with respect to historical geomorphic alterations to the North/South River system (Fitzgerald, 1993).

3.4.2 Field measurements

3.4.2.1 Field measurements overview

Field measurements from 2018 and 2020 include salt marsh sediment cores; seasonal sediment traps on the salt marsh platform; and water level, velocity, and turbidity measurements from both the channel and the marsh platform (Tab. 3.1, Fig. 3.1). Locations with the subscript "N" are in the North River, and locations with the subscript "S" are in the South River. Distances for North and South Rivers are reported up-estuary from the confluence of the two estuaries at New Inlet (Fig. 3.1).

3.4.2.2 Water column observations

We deployed channel instruments in the spring (March 13-April 20) and fall (October 4-December 6) of 2018. In the spring, pressure transducers for measuring water depth and optical-backscatter turbidity sensors (OBS) were deployed in the North River at 0.1 km and 2.9 km (ch_OBS1_N and ch_OBS2_N, respectively; Fig. 3.1). A Lowell Instruments tiltmeter for measuring water velocity at approximately 0.5 m above bottom was deployed in the South River at 3.6 km (ch_U_S; Fig; 3.1). Measurements of atmospheric pressure were collected with an additional pressure transducer deployed in a nearby parking lot. Elevations of water level loggers deployed on rebar in shallow water were measured with a Real Time Kinematic (RTK) GPS. For deeper moored sites, sensor elevations were determined by measuring water surface elevation with a Post-Processing Kinematic GPS over the mooring for one minute and then subtracting the average sensor-measured water depth during the same time interval.

Over the fall 2018 deployment period, we used the same pressure transducer and optical-backscatter turbidity mooring setup in the South River channel 2.4 km from the mouth (ch_OBS_S; Fig. 3.1). We also deployed a bottom mounted Aquadopp acoustic Doppler current profiler (2 MHz) in the North River 0.8 km from the inlet (ch_U_N). It provided velocity data at 20 cm increments from 0.6 m above bottom to 1 m below the water surface.

We used significant wave heights from the Boston wave buoy located ~20 km north of the estuary (NDBC buoy 44013) as a proxy for wave activity on the seaward side of the inlet and North River discharge at USGS gauge 01105730 (Fig. 3.1) as proxy for freshwater input to the North and South Rivers. North River discharge is a reasonable proxy for temporal variation in South River discharge given their spatial proximity.

3.4.2.3 Marsh platform observations

In spring 2018, we collected sediment cores at six locations on the North River marsh between 1.3 km and 15.9 km ($C1_N$-$C6_N$; Fig. 3.1) and four locations on the South River marsh between 2.4 km and 11.8 km ($C1_S$-$C4_S$; Fig. 3.1). At each location, we collected a transect of cores perpendicular to the marsh edge using a 6.3-cm-diameter gouge corer. We observed minimal sediment compaction during collection (see also Yellen et al., in prep.).

During the 2020 field seasons, we measured water level, turbidity, and seasonal sedimentation rates on areas of the marsh platform 1.7 km up-estuary from the inlet in the North River and 4.6 km from the inlet in the South Rivers (Fig. 3.1). Sediment traps and sensors were placed within 5 m of the marsh edge such that they would capture a strong

suspended sediment signal when the marsh was flooded from the channel. We mounted Onset HOBO U20L-04 pressure transducers and RBRsolo^3 OBS sensors on rebar and sunk the rebar into marsh sediment such that the pressure transducer vents and OBS window were 4 cm above the marsh platform. We placed a 0.09 m^2 ceramic tile underneath the sensors to prevent grass from obstructing the OBS (see Fig. D.1 for a photo of the sensor setup). A field test of two RBR Solo^3 OBS deployed in the same location with and without anti-fouling wipers showed that OBS on the marsh platform that go dry every low tide returned similar, high-quality measurements and thus generally did not require wipers. Pressure transducers recorded at a 10-minute interval, and OBS recorded at a 5-minute interval from March 18 through December 9, 2020. Records have one-day lapses on May 29 and September 9 when we serviced and redeployed the instruments. As with the channel measurements, we deployed an additional subaerial pressure transducer to record atmospheric pressure, and we used an RTK GPS to measure the marsh platform elevation at all sediment traps and sensors.

Seasonal sediment traps consisted of 2.7-cm diameter 50 mL plastic centrifuge tubes with ¼-inch plastic mesh secured over their openings with rubber bands to keep out macrofauna such as crabs (Fig. D.1). Three to five replicate traps were sunk into the marsh surface ~10 cm apart such that the lip of each tube was 1 cm above the marsh surface. Results from early deployments showed that measurements were sufficiently reproducible to deploy three tubes per location. We collected and redeployed traps to measure spring (3/18/20–5/29/20), summer (5/29/20–9/9/20), and fall (9/9/20–12/9/20) sedimentation. We could not deploy traps or instruments in the winter due to water freezing in sediment traps and around sensors. Thus, winter sedimentation was not

assessed, and our study excludes sediment delivered to the marsh via ice rafting (Argow et al., 2011; Fitzgerald et al., 2020b).

3.4.3 Sedimentary analyses

We assessed sediment cores for downcore chemical variations via X-ray fluorescence (XRF) core scanning (Croudace et al., 2006) then selected one core from each location for further analyses. The selected cores were between 10 and 50 m from the marsh edge and representative of average marsh stratigraphy away from the edge. Proximity to the channel and bank slumping can drive anomalously high sedimentation rates (e.g. Coleman et al., 2020; Mariotti et al., 2016; Reed, 1999; Temmerman et al., 2003). We measured mass fractions of water, organic material, and inorganic sediment at 10 cm intervals in each core via loss on ignition (LOI; Dean, 1974). Sediment core age models were based on visual stratigraphic constraints and downcore profiles of short-lived radionuclides via gamma spectroscopy (see Yellen et al., in prep. for a detailed description).

We measured downcore lead (Pb) concentration in North River cores after XRF profiles revealed a traceable horizon of high Pb counts (Yellen et al., in prep.). In brief, Pb concentrations were measured following USEPA Method 3050B using a hot-plate strong acid digestion. The digestate was diluted with 18.2 MΩ deionized water and analyzed with a Shimadzu 2030 Inductively Coupled Plasma-Mass Spectrometer. Every 25 samples included a duplicate, a standard reference material (NIST 2711b Montana Soil), and a digestion blank. Digestion blank Pb concentrations were < 0.05 ng g^{-1} measured concentrations, duplicates were within 12%, and NIST Montana Soil 2711b

recoveries were between 87–96% of their certified values. We derived a relationship between XRF counts and Pb concentration via a linear regression of all measurements to estimate the full downcore profile of Pb concentrations from XRF counts (Fig. D.2; DiScenza et al., 2014).

Centrifuge tube sediment traps were capped in the field and brought to the laboratory for measuring clastic deposition rate over each seasonal deployment. We decanted and rinsed samples twice to remove salt, combusted them at 550° C, and weighed them to determine clastic mass via LOI. Clastic deposition rates were calculated as clastic mass divided by sediment trap cross-sectional area, divided by deployment time. To account for variability in the number of spring-neap tide cycles within each deployment, we normalized by the number of days the sediment trap site was inundated (determined via water level loggers deployed adjacent to the traps).

3.4.4 Moored data analyses

Measured pressure in the channel and on the marsh were converted to water depth (d, in m) by:

$$d = (P_W - P_A) / (\rho_W * g)$$

where P_W is water pressure, P_A is atmospheric pressure, ρ_W is seawater density (assumed as 1029 kg m^{-3}), and g is gravitational acceleration (9.81 m s^{-2}). For channel data, we calculated the non-tidal residual using a 33-hour low-pass filter.

To clean channel OBS data, we first manually removed time intervals where turbidity rapidly fluctuated between low and anomalously high values. We then ran a wild-point editor ten times that removed outliers greater than 4 standard deviations from

a moving average. To clean marsh platform OBS data, we first used water levels from the same location to set turbidity to zero whenever the sensor was dry. We then manually removed time intervals when the sensor was clearly fouled or blocked, indicated by rapid fluctuations between high and low measurements or background turbidity gradually increasing without dropping back to zero when the sensor was dry at low tide. Turbidity often spiked to high values when the water surface crossed the sensor window on the flood or ebb tide, likely due to floating material at the water surface held by surface tension. We found that applying a 5-point median filter to the 5-minute marsh platform turbidity data removed this effect.

3.5 Results

3.5.1 Channel velocity and turbidity

3.5.1.1 North River channel

We compared the timing of distinct increases in channel turbidity to freshwater discharge and offshore wave height to identify the likely mechanistic driver of sediment delivery to the estuary and tidal marsh. In spring 2018, the time intervals with the highest observed turbidity in the North River at the ch_OBS2$_N$ station (2.9 km from the inlet; Fig. 3.1) were all concurrent with high offshore wave activity and a positive non-tidal residual, likely associated with storm surge (March 13-15, March 21-23, March 25-28, and April 15-17; Figs. 3.2a-b). Overall, the onset and timescale of high-turbidity intervals in the North River channel were better aligned with 2 to 3-day coastal storms than with the longer period 2-week spring-neap cycle. River discharge was also elevated during storms over the spring 2018 deployment; however, the timing of high turbidity aligned

closely with increases in offshore wave heights but not spikes in discharge. For example, the onset of high waves and high turbidity occurred on the same day during the March 21 storm and were followed by a more subtle increase in river discharge on March 22. Furthermore, there was no discernable turbidity response to high river discharge April 3-5, whereas all wave events over the deployment were concurrent with high turbidity.

Only the March 13 storm was recorded at the estuary inlet before the ch_OBS1_N sensor was buried on March 16. For three tide cycles during the storm, there was a strong pulse of turbidity on the flood tide that was greater in magnitude and arrived earlier at ch_OBS1_N relative to ch_OBS2_N 2.8 km up-estuary (Fig. 3.2d). Over the subsequent three tide cycles, turbidity declined steeply at ch_OBS1_N and more gradually at ch_OBS2_N such that turbidity at ch_OBS2_N began to exceed that at ch_OBS1_N on March 15.

We also examined turbidity as a function of tide hour over various time intervals at the ch_OBS2_N station. For reference, Figure 3.3a shows velocity for a typical tide cycle at ch_OBS2_N; peak velocity was slightly higher on the flood tide (0.79 m s^{-1}) than on the ebb (-0.76 m s^{-1}), but high flow velocities were more prolonged on the ebb. Figure 3.3b shows ch_OBS2_N turbidity as a function of tide hour for individual tide cycles during time intervals labeled in Figure 3.2. Intervals 1A and 2A were concurrent with storm surge (i.e. a positive non-tidal residual) for the March 13 and 21 storms, while intervals 1B and 2B spanned the time from the end of surge until the beginning of the next storm. We could not calculate the non-tidal residual for the March 13 storm with a low-pass filter because it fell at the beginning of the deployment; thus we assumed an equivalent 4-tide-cycle surge timescale for the March 13 and 21 storms. Flood tide

turbidity significantly exceeded ebb tide turbidity during surge (intervals 1A & 2A) and became more balanced on the flood and ebb when surge ended (intervals 1B & 2B). Turbidity also remained high over the four tide cycles concurrent with storm surge and began to decline as soon as surge ended.

At the beginning of interval 3, two smaller coastal storms between March 25 and 27 also drove high flood-tide turbidity in the North River channel. Again, we observed turbidity declining when storm surge conditions ended on March 28. Interval 4 captured an extended period of lower wave activity, during which flood and ebb-tide turbidity measurements were roughly symmetric. Interval 5 was defined by a coastal storm with moderate wave heights and a rapid increase in river discharge to the highest values observed during the spring deployment. Turbidity during this period was elevated relative to the prior quiescent interval during both flood and ebb tides.

3.5.1.2 South River Channel

We also compared turbidity and water level observations collected from the South River channel during fall 2018 to offshore waves and river discharge (Fig. 3.3). Turbidity and wave heights were generally low over the first three weeks of the fall deployment (October 5-27). An October 12 high discharge event that was equivalent to the peak discharge event observed during the spring deployment did not drive a discernible turbidity increase in the South River channel (Fig. 3.3c). In contrast, a coastal storm on October 28 was concurrent with two tide cycles of anomalously high turbidity and marked a transition to stormier conditions (with wave events beginning October 28 and November 10, 16, and 25) and high turbidity in the South River channel that persisted

through the remaining 5 weeks of the deployment. This prolonged high turbidity differs from spring North River observations, where turbidity dropped directly following surge and wave events (Figs. 3.2, 3.3b).

Figure 3.3 shows South River velocity and turbidity as a function of tide hour. At the moored locations, South River velocity was roughly half that observed in the North River (Fig. 3.3a). Peak ebb velocity (-0.39 m s^{-1}) exceeded peak flood velocity (0.33 m s^{-1}), and high flow velocities were more prolonged on the ebb. There were extended periods within the South River deployment where turbidity measurements were noisy, likely due to organic material being trapped on the sensor window; thus, we limit our discussion of turbidity to intervals with high data quality. In the turbidity versus tide hour panels (Fig. 3.3c), Interval 1 represents the period prior to the October 28 storm event when offshore wave heights and turbidity remained relatively low. Within each tide cycle over this initial quiescent interval, the highest turbidity was consistently at the end of the ebb tide. Intervals 2A-B represent observations following the October 28 storm (note that we exclude the two tide cycles concurrent with peak wave activity because turbidity values peaked above 300 NTU, likely due to obstruction of the sensor). Turbidity generally remained elevated and higher on the flood tide than the ebb tide for 5 days following the storm (Interval 2A, 10 tide cycles) before further decreasing and becoming more symmetric on the flood and ebb (Interval 2B). Intervals 3A-B and 4 show turbidity during and following the wave events that began November 16 and 25, respectively. For both events, storm surges (indicated by the positive non-tidal residual in Fig. 3.4) did not align with large turbidity pulses (Intervals 3A, 4); however, a distinct turbidity peak

persisted on the flood tide for 11 days following the November 16 storm (Interval 3B) and 10 days following the November 25 storm (Interval 4).

3.5.2 Marsh platform turbidity and seasonal deposition

We complement 2018 water column observations from the North and South River channels with similar observations from the marsh platform in 2020 (Fig. 3.5). Water depths measured on the North and South River marsh show that the platform was inundated twice per day during spring tides and remained dry during neap tides (gray and light green filled regions in Fig. 3.5b). Flood depths were generally within a few centimeters at the two sensors, but the South River site was inundated more frequently by low-amplitude high tides. At the location of the South River sensor, which was ~4 km farther up-estuary from the inlet than the North River sensor, tidal amplitude is smaller (due to tidal attenuation). Although marsh platform elevation is generally higher in the South River than the North River, the marsh is 15 cm lower at the particular location of the South River sensor (1.11 m NAVD88) than the North River sensor (1.26 m NAVD88).

The time intervals with the highest measured turbidity on the North River marsh platform aligned with concurrent wave and high discharge events on April 3 and 27 (Figs. 3.5a-b; intervals 1 and 2). During both events, a strong pulse of high turbidity was observed over the North River marsh for 3-5 high tides (approximately the duration of storm surge), after which turbidity declined to background levels within one week (Fig. 3.5c). Sediment delivery to the marsh over this one-week post-event period differed for the April 3 and 27 storms: the April 3 storm occurred immediately before spring tides, so

high spring tides continued driving high turbidity over the marsh directly following storm surge. Conversely, the April 27 event occurred during neap tides, so the marsh was only occasionally inundated over the subsequent five days, and turbidity had returned to lower background values by the following spring tides. The turbidity response during the April 3 and 27 events was more dispersed on the South River marsh than the North River marsh. Initial increases in over-marsh turbidity during these events were lower at the South River site, but the duration of elevated turbidity was longer, extending through the end of the following spring tides (Fig. 3.5c). This corresponded to nine total days of elevated turbidity during and after the April 3 event and fourteen days during and after the April 27 event.

Following these two storms, wave heights and river discharge were generally low mid-May through mid-August of 2020 (Fig. 3.5a). During this quiescent summer interval, turbidity was usually higher over the South River marsh than the North River marsh, particularly over time periods when South River inundation depths were greater (e.g. late-May and mid-July).

Two fall wave events on September 23 and October 30 again drove a greater turbidity response over the North River marsh than the South River marsh (Figs. 3.5a-b). River discharge during the first of these wave events remained low, consistent with wave-induced mobilization and delivery of marine sediment to the estuary rather than fluvial sediment delivery (similar to findings from 2018 observations from the main channel). Both the September 23 and October 30 wave events occurred at the end of spring tides, and we observed no discernable turbidity response beyond the timescale of these events. In contrast to the previous four wave events discussed, offshore wave peaks on December

1 and 5 caused higher turbidity at the South River marsh sensor than the North River marsh sensor. Both these early-winter events were short in duration (1 tide cycle) and occurred during neap tides. Sensors were retrieved for the winter before capturing the post-event response during the spring tide following these December storms.

We complement the 2020 marsh time series data (Fig. 3.5) with seven seasonal sediment traps deployed over the same time intervals (Table 3.2). Integrated seasonal accumulation of clastic material from these traps was consistent with higher sedimentation rates on the marsh platform in the spring and fall relative to the quiescent summer season. Spatial variability in sedimentation rates among the trap locations was influenced by their relative distances from the marsh edge, marsh elevation, and along-channel distance from the sediment source (Temmerman et al., 2003).

3.5.3 Sediment core clastic content and Pb concentration

The clastic fraction of marsh platform sediment was highest near the inlet and decreased in the up-estuary direction (Fig. 3.6). At $C1_N$ (1.3 km from the inlet), the surficial 50 cm of the marsh was on average 42% clastic, 5% organic, and 53% water by mass. The clastic mass percent then gradually decreased up-estuary to 6% at $C6_N$, 15.9 km from the inlet. Clastic content was similar at equivalent distances from the inlet in the South River.

A concurrent horizon of high Pb concentration dating to the early 1900s (Yellen et al., in prep.) was traceable in North River marsh at all core locations (Fig. 3.7). Concentrations were highest in the upper estuary and decreased significantly in the mid and lower estuary. In the upper estuary landward of the salinity reach, the maximum

measured Pb concentrations in the horizon were 4160 parts per million (ppm) at $C6_N$ (15.9 km from the inlet) and 3740 ppm at $C5_N$ (12.4 km). In the mid to lower estuary, concentrations monotonically decreased from 690 ppm at $C4_N$ (8.4 km) to 310 ppm at $C1_N$ (1.3 km). In the South River, we also found an early-1900s Pb horizon at $C3_S$, (8.1 km) and measured a maximum concentration of 260 ppm in the layer. The depth to the concurrent Pb horizon in each core illustrates along-estuary variation in marsh sedimentation rate. North River sedimentation rates near the inlet are roughly double those in the upper estuary, and the lowest sedimentation rates are in the South River (see also Yellen et al., in prep.).

3.6 Discussion

3.6.1 Marine sediment sourcing

Marsh platform and channel observations both support our hypothesis that marine sediment is the primary clastic sediment source to the North and South River estuaries. In estuary channels, we directly observe coastal storms (indicated by periods of high waves and a positive non-tidal residual) rather than periods of elevated river discharge, driving the highest measured turbidity over the 2018 channel deployments. The highest-turbidity time intervals in the North River channel align with high offshore waves and storm surge (Fig. 3.2a-b, Intervals 1a, 2a & 3) and are characterized by higher turbidity on the flood tide than the ebb tide (Fig. 3.3). During the March 13-15 storm, before the ch_OBS1_N sensor was buried at the inlet (Fig. 3.1), we also observe large flood-tide turbidity peaks at the inlet that appear two hours later and are smaller in magnitude at ch_OBS2_N 2.8 km up-estuary (Fig. 3.2d). This delay and damping of turbidity are consistent with marine

sediment entering through the inlet and being advected up-estuary on the flood tide. In the South River channel, turbidity does not fluctuate on the timescale of individual storm events, but a series of storms beginning on October 28 are concurrent with a prolonged 5-week period of high turbidity (Fig. 3.4, intervals 2-4). Throughout the North and South River channel deployments, discharge is also often elevated during storms; however, high discharge intervals that do not align with coastal storms (e.g. April 3 and October 12) do not drive a significant turbidity response in the channels relative to the wave event response. Furthermore, the initial pulse of high turbidity during the March 21 (Fig. 3.2c) and October 28 (Fig. 3.4c) storms clearly precedes the rise in discharge.

We were unable to measure turbidity or suspended sediment concentration on the seaward side of the inlet during storms; however, a pair of cloud-free Landsat 8 satellite images of the North/South River estuary from October 16 and November 17, 2018, clearly show waves elevating offshore turbidity (Fig. 3.4d). The October 16 image falls within the initial low-wave, low-turbidity, high-discharge period of our fall 2018 deployment. Ocean water is relatively clear, and the dark ebb plume, indicating higher concentrations of dissolved organic matter and lower concentrations of suspended sediment exiting the estuary through the inlet (e.g. Chen et al., 2020; Martinez et al., 2009), are consistent with our observation that discharge events do not deliver large sediment loads to the estuary. The November 17 image immediately follows high offshore waves and storm surge on November 15 to 16 and falls within a period of high turbidity in the South River channel (Fig. 3.4). Coastal waters are filled with light-colored suspended sediment, and again, a dark ebb plume is visible exiting the estuary. These images further support coastal and near-shore erosion as the primary sediment source

during storms, rather than upland sediment delivered via rivers or sediment derived internally from tidal flat and marsh edge erosion.

We had also hypothesized that storms and high spring tides would both be dominant mechanisms of sediment delivery to the North/South River estuary. We observe storms driving high turbidity in the channels, but we do not see evidence for two-week-timescale turbidity fluctuations that align with the spring-neap tidal cycle. This finding that storms deliver sediment to the North/South River estuary is significant because past observations (Fagherazzi & Priestas, 2010) and conceptual theory (Fagherazzi et al., 2013) have shown that storms driving strong tidal currents can also export significant amounts of sediment. We do not attempt the complex endeavor of quantifying sediment flux in tidal channels during storms (e.g. Ganju et al., 2013, 2017), but multiple lines of evidence support storms primarily being a mechanism for sediment delivery to the North/South River estuary. First, time intervals with the highest measured channel turbidity align with coastal storms (Figs. 3.2 & 3.4) and are characterized by higher turbidity on the flood tide than the ebb (Fig. 3.3b-c). The November 17 satellite image is consistent with storms not exporting significant amounts of sediment in showing a dark ebb plume entering sediment-laden coastal waters immediately following the November 15-16 storm (Fig. 3.4d). Lastly, clastic deposition rates on the marsh are higher in the stormy spring and fall seasons than the quiescent summer season (Tab. 3.2).

Marsh platform stratigraphy reinforces channel observations in supporting the hypothesis that marine sediment is a significant source to the North and South River estuaries. The early-1900s Pb contaminant horizon traces the limited spatial extent of fluvial sediment contributions. A former munitions manufacturing, testing, and disposal

facility (called “The Fireworks Site”) located on a tributary to the North River in Hanover, MA is the most likely Pb source (Fig. 3.1). The Fireworks Site began operations during World War I (1914-1918) and is known to have used Pb and mercury in its manufacturing processes (Town of Hanover, 2008) that has since been found in high concentrations in surrounding surface water, sediment, and fish tissue (Tetra Tech, 2005). We observe high Pb concentrations (~4000 ppm) in the upper North River estuary freshwater tidal marsh platform above the salinity reach at $C5_N$ and $C6_N$ (Fig. 3.7). In the mid-to-lower estuary, the combination of declining Pb concentration (Fig. 3.7), increasing clastic content (Fig. 3.6), and increasing sedimentation rates (Fig. 3.7; Yellen et al., in prep.) suggests significant dilution of contaminated fluvial sediment by a dominating marine clastic sediment source. In the South River marsh, we also observe an increase in clastic content toward the inlet that is consistent with marine sediment sourcing. Compared with the North River, the early-1900s Pb peak is more subtle in the South River, further supporting The Fireworks Site as the probable Pb source (Fig. 3.7).

The relatively minor contribution of fluvial sediment in the North/South River estuary is consistent with findings at the Plum Island Sound estuary (~60 km to the north) that rivers only supply 8% of the clastic sediment required for the marsh to maintain its elevation relative to present sea level rise (Hopkinson et al., 2018). We do not measure fluvial suspended sediment concentrations, but sediment yields are relatively low throughout the New England region (e.g. Meade, 1969; Millman & Farnsworth, 2011; Ralston et al., 2021; Weston, 2014), and the North and South River watersheds have similar characteristics to the watersheds supplying Plum Island Sound in that they are low relief with relatively high freshwater wetland and forest land cover. By process of

elimination, Hopkinson et al. (2018) infer that the combination of external marine and internal tidal flat sediment is the most significant sediment source to the Plum Island Sound estuary; however, they do not provide observational evidence for or delineate between the two sources due to the hydrodynamic complexity of the inlet (Zhao et al., 2010). In the smaller North-South River estuary, it is simpler to constrain transport and show that external marine sediment is the system's primary source, resulting in what we believe is the first observational study from the region to confirm marine sourcing.

3.6.2 Sediment delivery timescales and marsh platform deposition

The spring-neap cycles is a dominant influence on sediment delivery from estuary channels to the marsh platform. Both in the channel and over the marsh, measured storm turbidity peaks are higher-magnitude and shorter in duration from sensors in the North River when compared to those deployed in the South River. In the North River channel, turbidity rapidly declines over 1-2 days after surge ends (e.g. Fig. 3.3, intervals 1b & 2b). As a result of this short duration of elevated sediment concentrations in the channel, the phasing of storm surge with the spring-neap cycle determines whether post-event suspended sediment is delivered to the marsh platform. For example, during spring tides we measure high turbidity at the North River marsh platform sensor for ~3 days following the April 3 storm (Fig. 3.5b, interval 1). In contrast, the April 27 storm occurred during neap tides, and by the time spring tides returned to inundating the marsh platform on May 2nd, turbidity had dropped to background levels (Fig. 3.5b, interval 2).

At the South River sensors, we observe high turbidity persisting for 5-11 days following storms in the channel (Fig. 3.4, intervals 2a-b, 3a-b & 5) and 9-14 days on the

marsh (Fig. 3.5b), albeit at roughly half the turbidity values observed at our North River channel location. This longer period of elevated turbidity makes sediment delivery to the marsh platform less dependent on the phasing of events with the spring-neap cycle. In the case of the April 27 storm, high turbidity persists over the South River marsh platform for the entire spring tide following the storm (in contrast to the North River site), despite the storm occurring during neap tides.

Understanding the geomorphic drivers of the varying turbidity timescales between the North and South Rivers would require a greater spatial distribution of moored observations over concurrent deployments. However, we hypothesize that the lower elevation of the North River marsh relative to mean high water is a potential explanation. When the 1898 Portland Gale shifted the North/South River inlet 5.6 km to the north, North River mean high water elevation instantaneously increased because the truncated length of the estuary reduced tidal attenuation. Although North River sedimentation rates have been roughly double those observed in the South River since the inlet switch, the system is still adjusting (Yellen et al., in prep.). It is well established that greater marsh platform inundation depths enhance deposition (e.g. Bricker-Urso et al., 1989; Marion et al., 2009; Pethick, 1981; Temmerman et al., 2003), so higher inundation depths on North River marsh platform may shorten the duration of high suspended sediment concentrations the channel due to enhanced trapping on the marsh. The relatively higher marsh elevations in the South River estuary lower the rate of sediment trapping. Storm-induced pulses of sediment should therefore be expected to remain in the South River channel for longer, explaining the longer storm response timescale of suspended sediment. The higher marsh platform also may explain the greater relative ebb turbidity

in the South River under non-storm conditions. If less sediment is trapped on the marsh platform, more sediment must be exported to the ocean during non-storm conditions to approach a net sediment balance.

3.6.3 Implications of coastal armoring

An implication of externally derived marine sediment supplying the North and South River estuaries is that coastal and nearshore sediment supply and erosion rates influence marsh accumulation. In New England, surficial sediment sources in coastal and nearshore regions are primarily glacial-fluvial and glacial-lacustrine deposits (e.g. Woodruff et al., 2021). In the case of the North and South Rivers, adjacent shoreline recession (Theiler et al., 2013) and the rapid erosion of Fourth Cliff (Fig. 3.1; U.S. Air Force, 2014) are potentially significant sediment sources.

Human decision-making impacts erosion at the coast and thus has the potential to impact marsh sediment supply. As of 2013, nearly 27% of the Massachusetts coastline was armored by some form of coastal protection (Fontenault et al., 2013). The impact of armoring on sediment budgets of adjacent estuaries has not been documented, but our findings show that armoring could reduce the ability of marshes to keep pace with future sea level rise in systems like the North/South River estuary that rely on an external marine sediment supply.

3.7. Conclusions

This study provides clear evidence that marine sediment is the major clastic sediment source to marshes in a small, mesotidal estuarine system characteristic of the

New England coastline. Spatial variation in marsh sediment clastic content and fluvially-sourced Pb pollution show that marine-sourced clastic sediment has been the primary external sediment source in the mid-to-lower North and South River estuaries. We also observe sediment advected through the inlet during coastal storms as the primary driver of high turbidity in estuary channels and over the marsh platform. Thus, our observations are among the first to show external marine sediment mobilized during storms as the primary sediment source to the estuary, rather than terrestrial sediment delivered via rivers or internally derived sediment resuspended from tidal flats or eroded from the mash edge.

Suspended sediment in the estuary is a highly non-stationary quantity, with timescales of sediment delivery range from 2.5 days to 2 weeks depending on the location within the estuary. In locations with shorter sediment residence times, the extent of sediment delivery from the channel to the marsh platform is dependent on timing of storms relative to the spring-neap tide cycle. This study reveals that sediment supply to and associated resilience of New England mesotidal salt marshes involves the interplay of coastal and estuarine processes, underscoring the importance of looking both up- and downstream to identify key drivers of environmental change.

3.8 Acknowledgments

Funding for this research was primarily provided by the Northeast Climate Adaptation Science Center (Award G20AC00071). H.E.B. was supported by a Northeast Climate Adaptation Science Center graduate fellowship. The authors would like to thank

N. Randall, F. Griswold, D. Beach, S. Wenczel, K. McKeon, J. Casey, W. Lau, C. Ladlow, and A. DiTroia for help with field work and laboratory analyses.

Table 3.1. Timetable of channel and marsh platform measurements. Black bars are North River measurement locations, and white bars are South River locations (see Fig. 3.1).

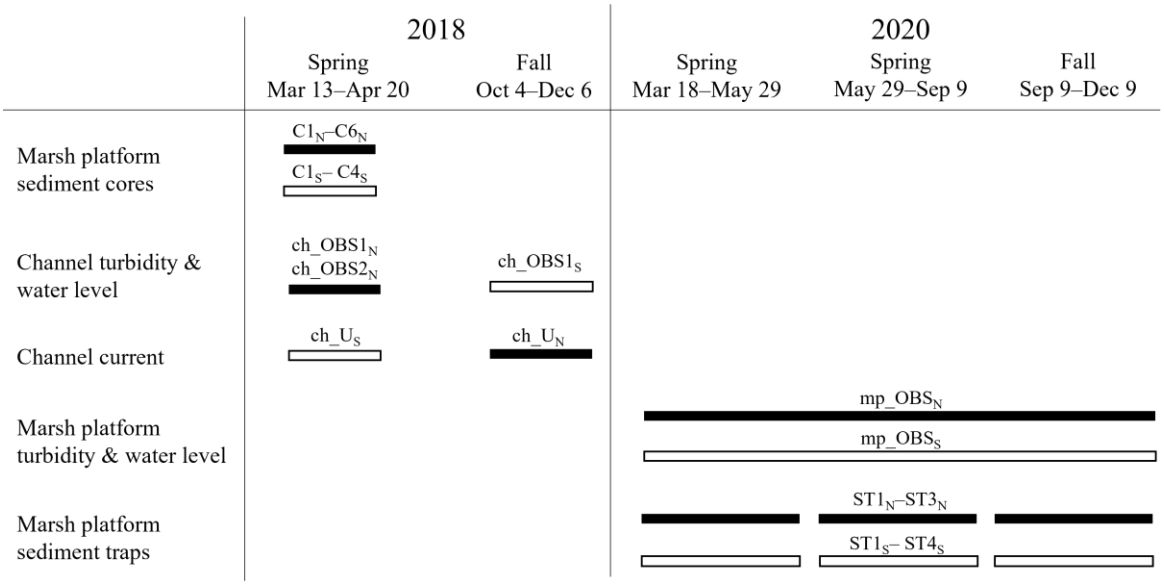

Table 3.2. Seasonal clastic sedimentation rates on the marsh platform edge measured by sediment traps. See Fig. 3.1 for locations.

		Clastic sedimentation rate ($g/cm^2/y$)		
	Site	**Spring**	**Summer**	**Fall**
North River	**$ST1_N$**	1.27	0.20	0.94
	$ST2_N$	0.79	0.37	1.40
	$ST3_N$	0.19	0.16	0.20
South River	**$ST1_S$**	0.40	0.15	0.74
	$ST2_S$	*not recovered*	0.25	0.48
	$ST3_S$	0.26	0.11	0.24
	$ST4_S$	0.25	0.11	0.85

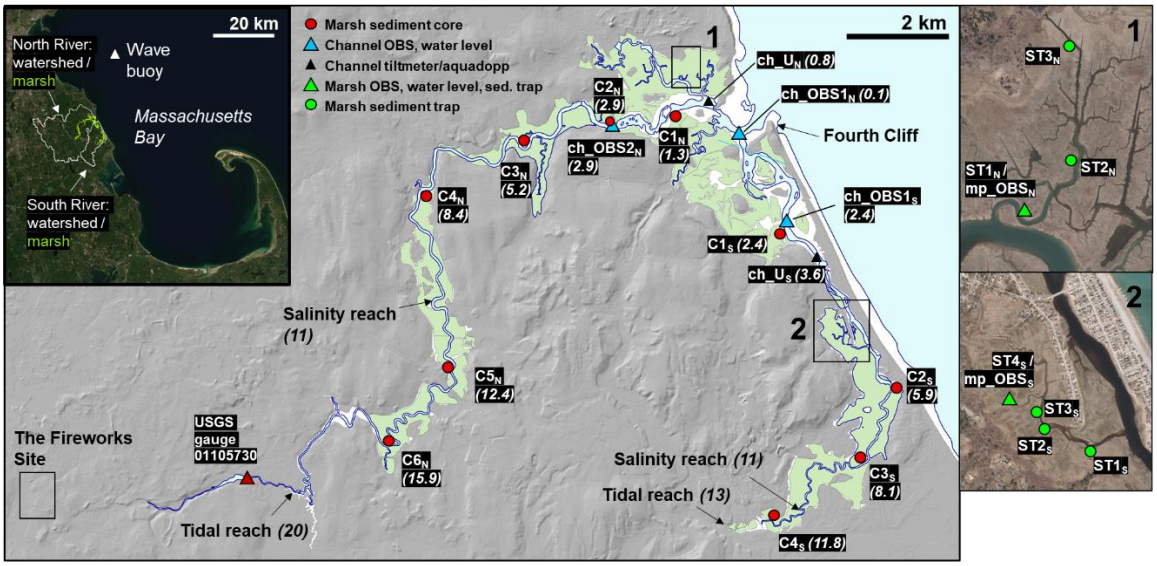

Figure 3.1. North and South River estuaries site map, showing locations of all field measurements. Italicized numbers in the parentheses following measurement location names indicate the distance up-estuary from the inlet in kilometers.

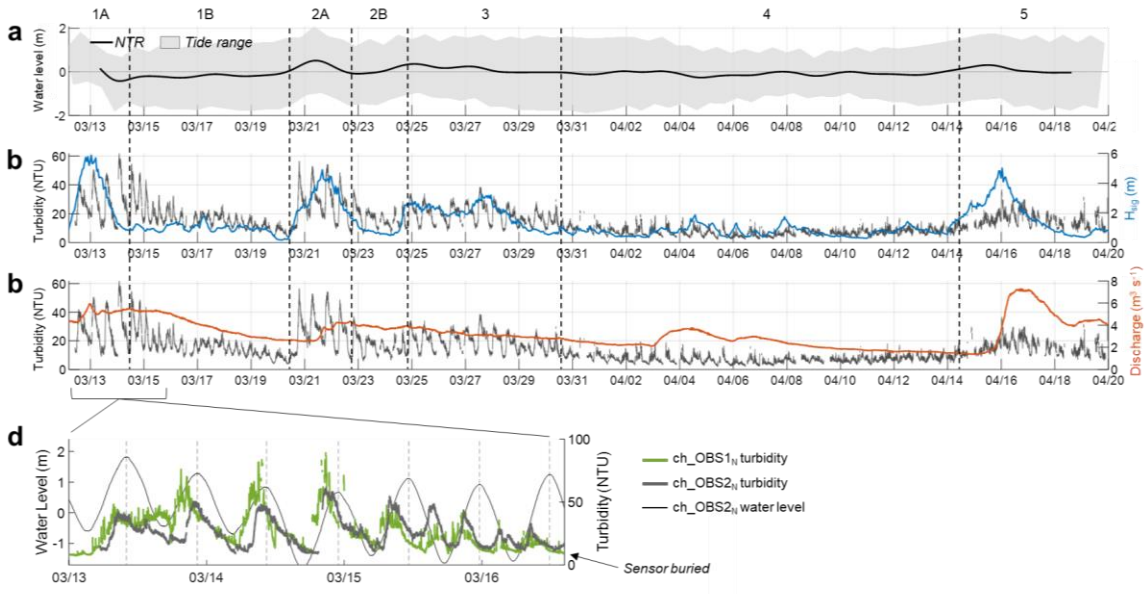

Figure 3.2. North River channel measurements for the spring 2018 deployment at ch_OBS2$_N$. Vertical dashed lines and labels above panel ***a*** mark time intervals in Figure 3.3. (a) Tide range (gray shading) and the non-tidal residual (black line) calculated from the water level time series. (b) Channel turbidity (gray line) relative to offshore significant wave height at the Boston wave buoy (blue line; see Fig. 3.1 for buoy location). (c) Channel turbidity relative to North River discharge measured at the USGS gauge (red line; see Fig. 3.1 for gauge location). (d) Close-up of the March 13 coastal storm, which was the only event recorded at ch_OBS1$_N$ (0.1 km from the inlet) before the sensor was buried, showing turbidity at ch_OBS1$_N$ (green line) and ch_OBS2$_N$ (gray line) along with ch_OBS2$_N$ water level (black line). Vertical dashed lines mark high water for each tide cycle.

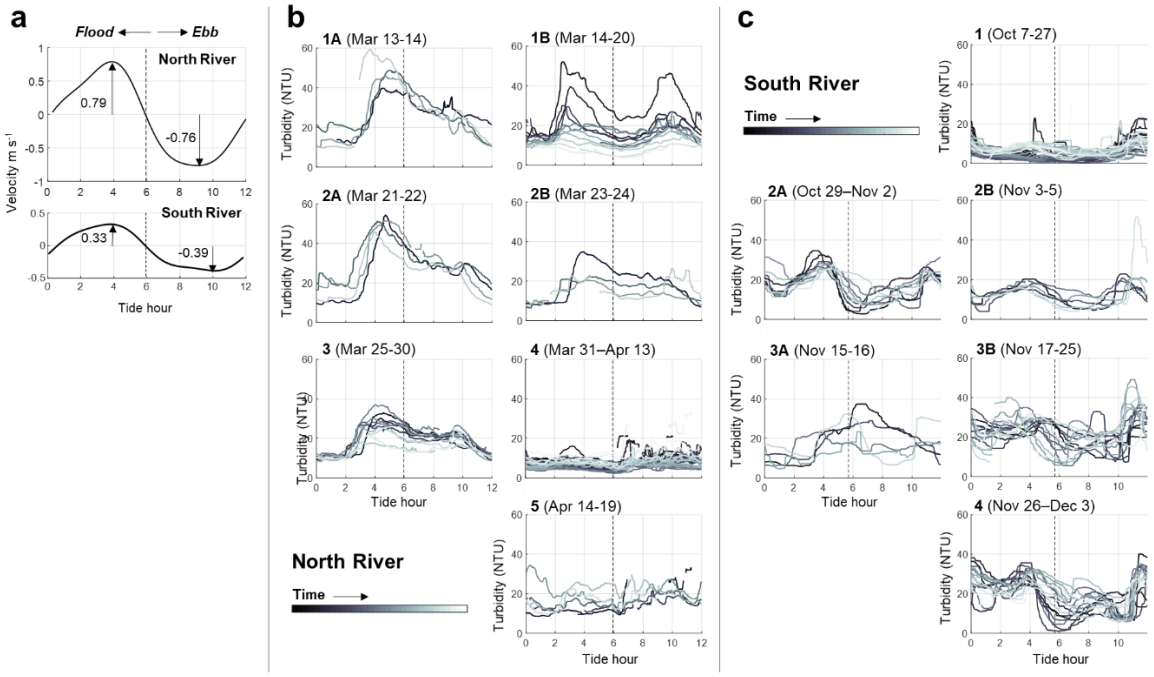

Figure 3.3. Turbidity and velocity versus tide hour at the ch_OBS2$_N$ (North River) and ch_OBS$_S$ (South River) sensors. (a) Velocity versus tide hour for a typical tide cycle at each sensor location, derived via harmonic analysis of water levels. Tide hour 0 is the beginning of flood tide at the inlet, and maximum and minimum velocities within the tide cycle are labeled. (b) North River ch_OBS2$_N$ turbidity versus tide hour, where panels correspond to time intervals labeled in Figure 3.2. Each curve represents one tide cycle; the first tide cycle over each time interval is black, and lines get progressively lighter over subsequent tide cycles. The vertical dashed line in each panel delineates the flood and ebb tide. (c) South River ch_OBS$_S$ turbidity versus tide hour, where panels correspond to time intervals labeled in Figure 3.4.

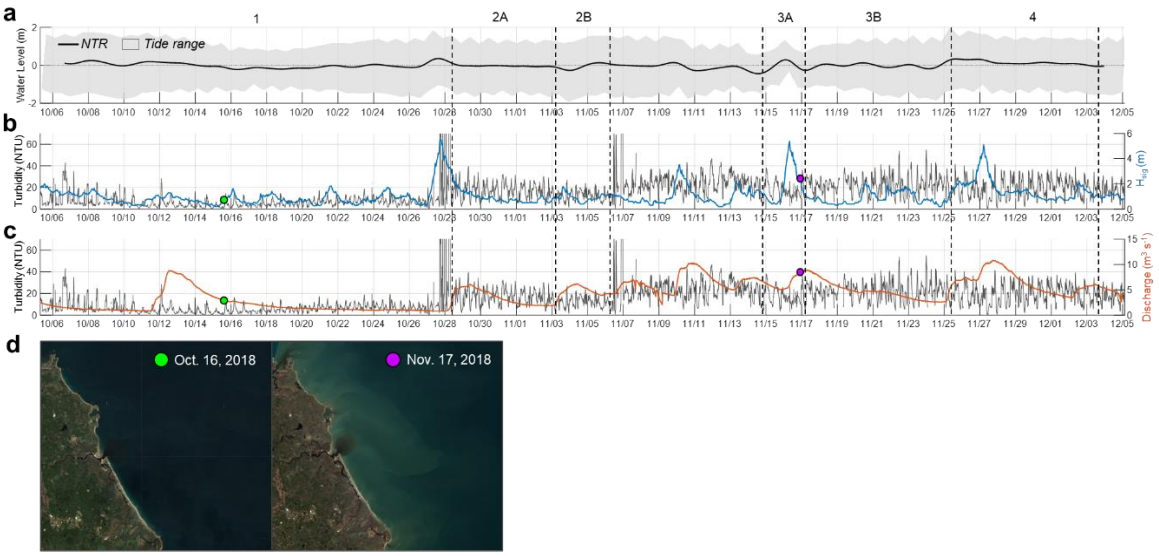

Figure 3.4. South River channel measurements for the fall 2018 deployment at ch_OBS$_S$. Vertical dashed lines and labels above panel a mark time intervals in Figure 3.3, and green and purple circles in panels ***b-c*** mark timing of satellite images in panel ***d***. (a) Tide range (gray shading) and the non-tidal residual (black line). (b) Channel turbidity (gray line) relative to offshore significant wave height at the Boston wave buoy (blue line). (c) Channel turbidity relative to North River discharge measured at the USGS gauge (red line). (d) Landsat 8 satellite images of the North and South River estuaries during non-storm (left) and storm (right) conditions.

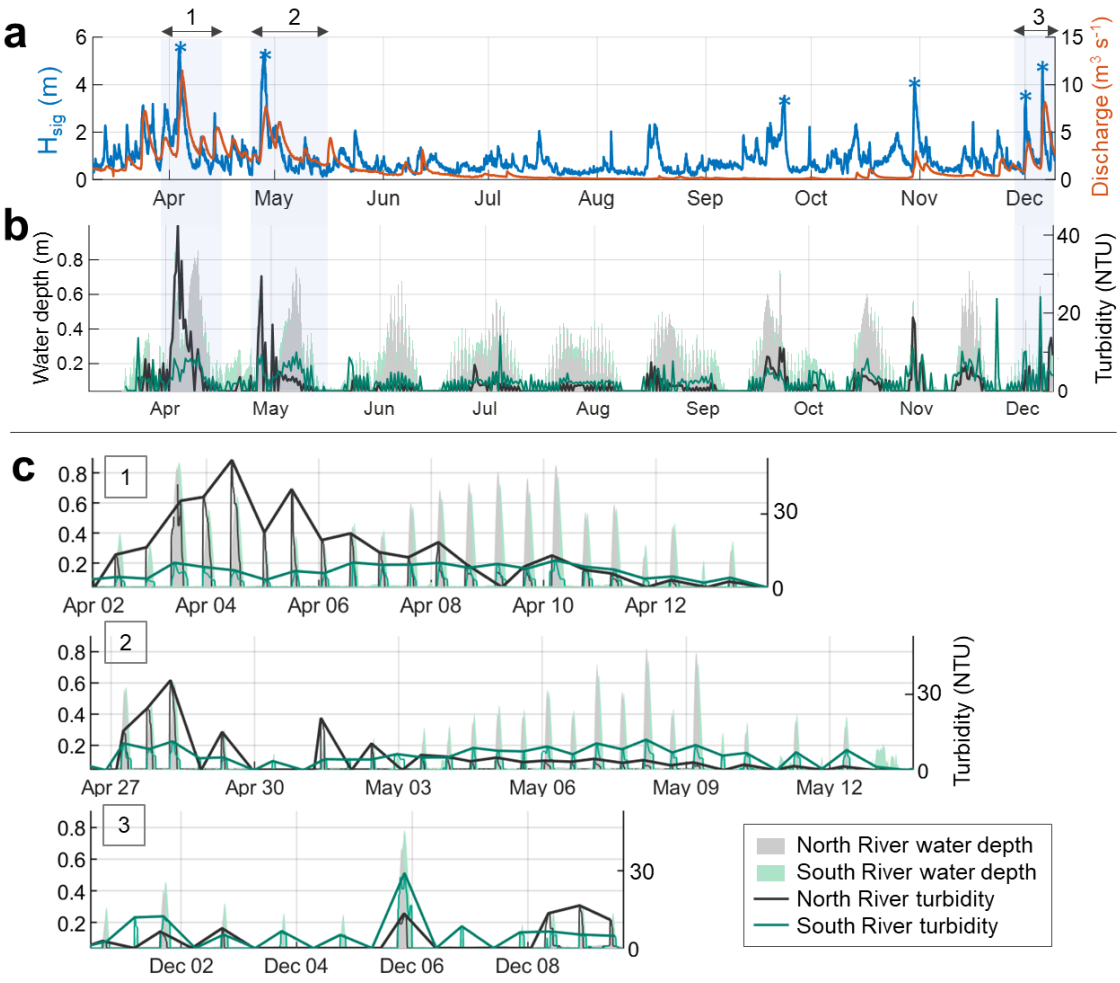

Figure 3.5. 2020 marsh platform moored observations at mp_OBS_N and mp_OBS_S. (a) Offshore wave heights at the Boston wave buoy (blue line) and North River discharge at the USGS gauge (red line). (b) Water depths over the North and South River marsh platforms (gray and green filled regions, respectively) and the maximum turbidity value measured over each tide cycle (black and green lines). Laboratory calibrations of these turbidity sensors show suspended sediment concentrations are roughly 1.8 times measured turbidity. (c) Enlarged time series for three offshore wave and high discharge events, with number labels corresponding to panels ***a-b***. Note that the thin black and green lines show the full turbidity time series.

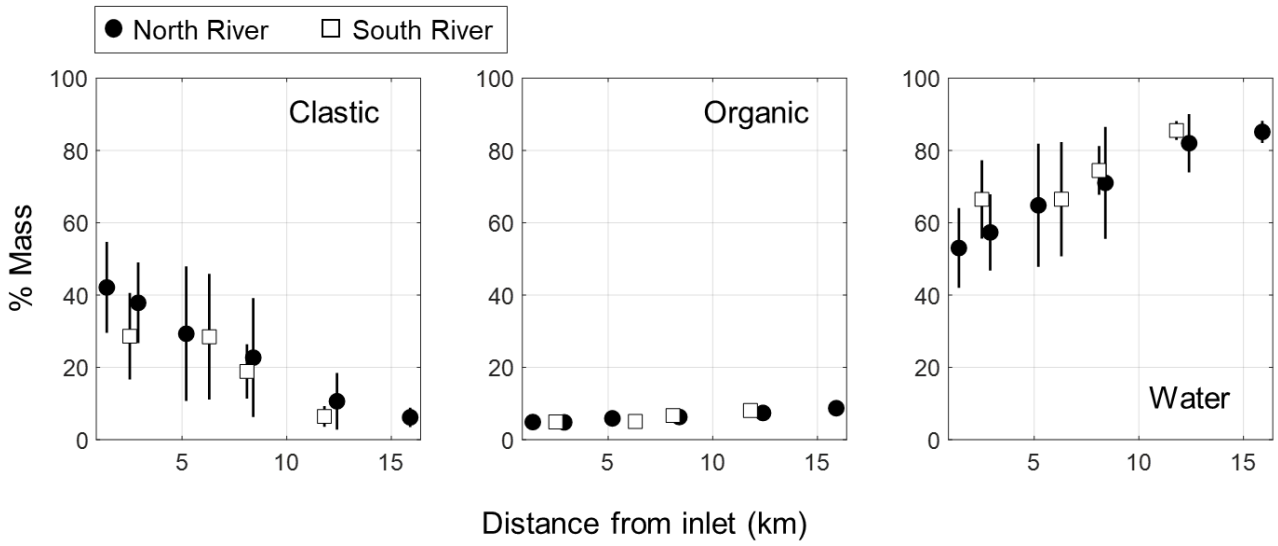

Figure 3.6. Variation in marsh platform sediment composition in percent mass with distance from the inlet in the North River (circles) and South River (squares). Point markers show mean mass percent of clastic sediment, organic material, and water, determined by loss-on-ignition of roughly 5 samples from the upper 50 cm of each core. Lines are one standard deviation of the mass percent data at each location.

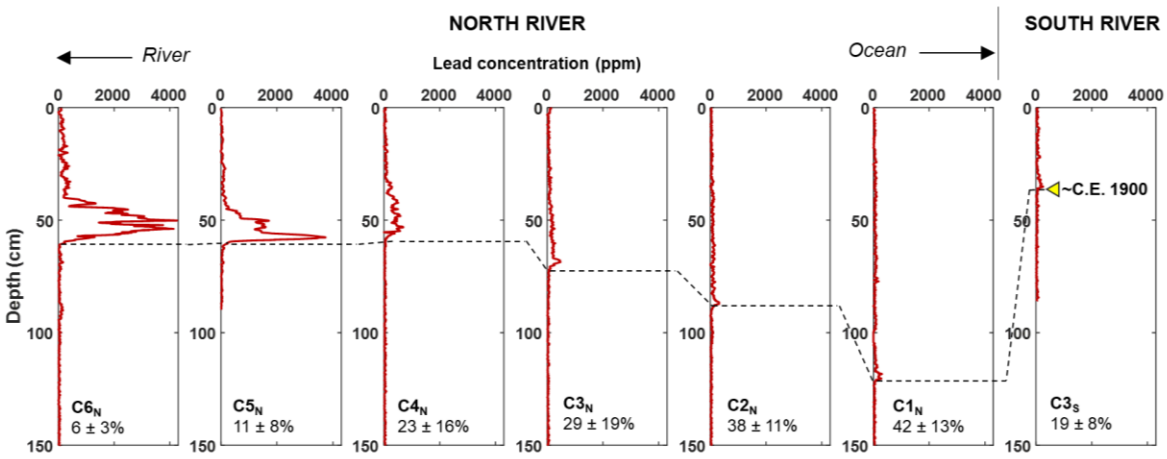

Figure 3.7. Pb concentration depth profiles from six representative North River cores (left six panels) and one South River core (rightmost panel) collected on the marsh platform. Concentrations are derived from an XRF counts-to-concentration calibration (Fig. D.2), and the dashed line marks the onset of and early-1900s contaminant horizon in each core (see Yellen et al., in prep. for age models). For reference, the mean and standard deviation percent clastic mass in the upper 50 cm of each core (relative to total wet mass) is listed below the core name in each panel.

CHAPTER 4

REFLECTIONS AND FUTURE DIRECTIONS

4.1 Chapter one

Humans live in the physical footprint of natural hazards on most of Earth; thus the study of natural hazards is closely connected with and often cannot be separated from human vulnerability. Conducting research around natural hazards far from one's own community and without strong ties to the vulnerable population is therefore challenging. Our demonstrated method for constructing earthquake models by scaling coupling to slip has broad applicability; however our finding that localized subsidence may drive high tsunami hazard in northwestern Shikoku (close to the island's sole nuclear power plant) has significant implications for local risk management. Given our minimal connections to the local decision-makers and community members, our research team was not equipped leverage our finding toward risk mitigation action.

Climate change is driving and unprecedented increase coastal risk globally, and there is an urgent need for actionable coastal hazard assessments. As I continue in this field, I will aim to shape and conduct my research in collaboration with vulnerable communities so that I can better contribute to the urgent need for building resilience at the coast.

4.2 Chapter two

The quasi-nonstationary skew surge joint probability method (qn-SSJPM) presented in Chapter 2 has exciting implications for improving flood hazard assessments

along the Gulf of Maine coast. The primary limitation of the method as it exists is that it can only be used to calculate flood exceedance curves at locations with long-term tide gauges. For example, the method provides improved flood hazard assessment at the location of the Boston NOAA tide gauge in the Seaport area of the city, but results cannot be extrapolated to East Boston, the Massachusetts South Shore, or any location not in the immediate vicinity of the tide gauge. Spatially continuous flood projections require hydrodynamic simulations; however, it takes tremendous human and computational resources to develop flood simulations that include statistically representative sets of storms, tides, and sea level rise scenarios.

The qn-SSJPM could be adapted and used in combination with hydrodynamic modeling results to provide flood projections with unprecedented accuracy for the Gulf of Maine. The U.S. Army Corps of Engineers (USACE) as a part of their North Atlantic Coast Comprehensive Study (NACCS) provides flood statistics under present-day conditions and 1 meter of sea level rise from Virginia to Maine. Publicly available NACCS model results include simulated storm surge and wave setup for 100 historical extratropical cyclones and 1,050 synthetic tropical cyclones; one month of simulated tides; and a parameterization of non-linear effects due to sea level change (Nadal-Caraballo et al., 2015; results available on the Coastal Hazards System data portal).

NACCS flood statistics were obtained by combining storm simulations with 96 tidal alignments over just one month in September 2010. Joint tide-surge probability assessments indicate that this 1-month duration is far too short to adequately assess flood frequencies for meso-to-macrotidal regions like the Gulf of Maine. As an example, at the location of the Eastport, ME tide gauge, September 2010 tides fail to capture the largest

2% of tides over a complete nodal cycle. As a result, the NACCS model underpredicts flood levels by nearly 0.5 meters for most return periods when compared to both unbiased (i.e. empirical) return periods calculated from the Eastport tide gauge record and Baranes et al. (2020) statistics, which have been extensively validated.

We have tested a technique for combining NACCS modeled surge plus wave setup distributions with predicted water levels over a full nodal cycle, following a modified qn-SSJPM methodology. This pilot technique combines the efficiency of the qn-SSJPM with spatial coverage from hydrodynamic simulations, and the preliminary resultant flood hazard curve at the Eastport gauge nearly overlaps with independent, unbiased observations. We plan to develop this methodology further and apply it throughout the Gulf of Maine.

4.3 Chapter three

Spatially heterogenous channel and marsh platform morphology are a primary challenge working in salt marsh estuaries. It is difficult to choose representative locations where measurements can be used to make broad, system-wide interpretations. I underappreciated this challenge early on and prioritized long deployment periods at fewer locations over shorter deployment periods at more locations. If I were to redesign the study, I would have measured turbidity at a minimum of two locations (but ideally three or four) in both the North and South Rivers.

Looking ahead, we plan to geographically expand this research. Our findings in Chapter 3 are the first to document and confirm marine sediment sourcing to a New England salt marsh. Conducting similar studies at regional estuaries with varying

oceanographic conditions (e.g. tide range, storm conditions, wave climate), geologic settings, and marsh-channel morphologies contribute to answering the following questions relevant to coastal management: How much control does sediment supply have on the ecological integrity and resilience of New England marshes? Across various oceanographic and geologic settings, what are the primary sources and mechanisms of sediment delivery? What limits sediment supply? What is the impact of upland and coastal human modifications (e.g. tidal restrictions, coastal armoring, damming, and land use change)? What are the implications for sediment-based restoration techniques? Despite the elementary state of scientific knowledge around these questions, managers are already investing in sediment-based restoration techniques. With close monitoring, ongoing projects provide potential opportunities for investigating sediment sourcing.

APPENDIX A

CHAPTER 1 SUPPORTING INFORMATION

A.1 Introduction

Text S1-S5 contain detailed descriptions of methods for constructing coupling-based rupture scenarios, setting up and running tsunami inundation simulations, and evaluating historical observations. Figure A.1 shows topography and bathymetry grids used in tsunami inundation simulations. A dataset containing ground surface displacement grids for the four coupling-based rupture scenarios is available with the online publish manuscript (Dataset S1).

A.2 Interseismic coupling-based rupture models (Text S1)

We generate four coupling-based rupture models by assuming that coseismic slip is proportional to estimated interseismic coupling. We use the trench-coupled and trench-creeping ISC distributions from Loveless and Meade (2016) (Figure 1.1c), which are constrained by GEONET GPS observations from 1996-2015 (Geodetic Observation Center, 2015; Sagiya et al., 2000) and estimated using an elastic block model. The Nankai subduction interface is represented by 1,902 triangular dislocation elements (TDEs) embedded in a homogenous elastic half-space that capture its geometry from 0-50 km depth, based on slab contours from Furuse and Kono (2003). A coupling fraction, defined as the ratio of slip deficit to relative plate motion between the Philippine Sea Plate and southwest Japan forearc, is estimated for each TDE, where coupling fractions range from -0.96 to 1.62 for the trench-coupled case and from -0.37 to 1.37 for the

trench-creeping case. TDEs with negative values represent sections of the trench that are slipping aseismically. Some elements have coupling fractions >1 or <0 because when estimating slip deficit rates, rather than applying bounds to the rates, Loveless and Meade (2016) chose a smoothing constraint that resulted in no more than 10% of TDEs having slip deficit rates exceeding the plate convergence rate.

When scaling coupling to slip, we assign a slip magnitude of 0 to all elements with coupling fractions ≤ 0.3, guided by the spatial correlation between coupling fractions ≥0.3 and the extent of rupture of the 2011 M_W 9.1 Tohoku-oki earthquake (Loveless & Meade, 2011). We then apply a linear scaling for TDEs with coupling fractions between 0.3 and the maximum (1.62 for the trench-coupled case or 1.37 for the trench-creeping case, where Loveless and Meade (2016) limit coupling values >1 to isolated TDEs in the geometrically complex northeast region of the Nankai subduction interface). We create our set of four coupling-based rupture models by using two methods to determine the rake of slip (as described in the main text) for both the trench-coupled and trench-creeping coupling distributions. The two rakes are similar on strongly-coupled TDEs, but partially-coupled elements feature differing slip deficit and relative plate motion rakes. For each of the four rupture scenarios, we run tsunami simulations for a range of peak slip values, and we choose the value that produces the best match between modeled tsunami heights and historical observations of the 1707 tsunami (explained below).

A.3 Earthquake sources for tsunami simulations (Text S2)

We simulate the resultant tsunami inundation for the Hyodo et al. (2014) scenario (H14) and the four coupling-based rupture scenarios. Initiating a tsunami simulation from an earthquake model requires calculating vertical displacement of the earth's surface from coseismic slip. For the H14 scenario, the 1-arc-minute resolution topography displacement file used to initiate tsunami simulations was provided by the authors (Figure 1.1b). For the coupling-based scenarios, we calculate partial derivatives relating unit strike-slip and unit dip-slip on each TDE to horizontal and vertical displacement at the surface of a homogeneous elastic half-space (Meade, 2007). We then multiply the slip on each TDE by the partial derivatives to analytically calculate vertical coseismic surface displacement on a grid that matches the H14 displacement grid (Figure 1.1d). Ground surface displacements for the four coupling-based models are in Dataset S1.

A.4 GeoClaw numerical model (Text S3)

We perform tsunami inundation simulations using version 5.3.0 of the open source tsunami model GeoClaw (Berger et al., 2011; Clawpack Development Team, 2015; Mandli et al., 2016), which is a subset of Clawpack. GeoClaw models flow over varying topography using high-resolution finite volume methods to solve the nonlinear shallow water equations and has undergone extensive validation testing with real events and synthetic test problems (Arcos & LeVeque, 2015; González et al., 2011; LeVeque & George, 2008; LeVeque et al., 2011). The Manning coefficient (n), which is determined by surface roughness, is the only adjustable parameter in the model's governing

equations. We use the constant value of $n = 0.025\ m^{-1/3}$ for the seafloor, which is common in tsunami modeling (Arcos & LeVeque, 2015).

All GeoClaw simulations are initiated by instantaneously displacing the ocean floor, following the distributions of vertical coseismic surface deformation described above and illustrated in Figures 1.1b and 1.1d. As the tsunami propagates across the ocean, GeoClaw uses a block-structured adaptive mesh refinement (AMR) algorithm that increases grid resolution and decreases the time step around the tsunami (LeVeque et al., 2011). We use a 0.5° (~50 km) grid resolution at the coarsest level, and four nested AMR levels increase resolution to ~100 m around the Kyushu, Shikoku, and Honshu coasts. Around Lake Ryuuoo, we add one additional level that increases resolution to ~5 m. Bathymetric data sources are provided in the topographic model section below. GeoClaw automatically refines the timestep to achieve a Courant number of 0.75.

Initial low-resolution model runs revealed that the first wave consistently produces the largest inundation depth within 2 hours of model initialization, so we run all of our simulations for 3 hours. We use GeoClaw's fixed grid monitoring tool to output maximum water surface elevations around the Pacific coastlines of Kyushu, Shikoku, and Honshu (Figure 1.2). We also place model gauges that monitor water surface elevation around Ikata Power, Uwajima, and Lake Ryuuoo (Figure 1.3).

A.5 Topographic model (Text S4)

We merge seven topography and bathymetry datasets to create uniformly spaced, rectangular land surface elevation grids at the four different resolutions within the tsunami simulation domain of 129 to 141°E and 30 to 37°N (Figure S1). All topography

and bathymetry data are adjusted in reference to mean sea level. A 1-arc-minute (~1,600 m) grid, created from the 1-arc-minute ETOPO1 global topography and bathymetry model (Amante & Eakins, 2011), covers the entire computational domain. We add two sets of finer grids with 0.005° (~500 m) and 0.001° (~100 m) resolution around the Kyushu, Shikoku, and Honshu coastlines. For the 0.005° grids, we merge the J-EGG500 500 m resolution bathymetric grid, published by the Japan Oceanographic Data Center, with the Global 30 Arc-Second Elevation (GTOPO30) topography dataset, available from the U.S. Geological Survey. For the 0.001° grids, we merge charts from the M7000 map series, which are sets of digital bathymetric contours provided by the Marine Information Research Center (MIRC) of the Japan Hydrographic Association (JHA), with version 2 of the 1-arc-second (~30-m) Advanced Spaceborne Thermal Emission and Reflection Radiometer Global Digital Elevation Model (ASTER GDEM). ASTER GDEM is a product of NASA and METI. Around Lake Ryuuoo, we also create a 0.00005° (~5 m) grid in order to resolve inundation of the lake's barrier in detail. We use high-resolution bathymetric data from a C3D multi-beam survey performed by Arc Geo Support Co., Ltd. on July 21, 2014 and merge it with a 5 m digital elevation model published by the Geospatial Information Authority of Japan.

When merging and interpolating gridded topography and bathymetry datasets onto a new grid for tsunami modeling, it is important to preserve the coastline's location. For the 0.005°, 0.001°, and 0.00005° grids we use to resolve inundation in our simulations, the coastline is better-defined by the topography data; thus, before interpolating onto the final combined grid, we extract the 0-m-elevation contour from the topography. We then convert the 0-m contour and all of the gridded topography and

bathymetry data to XYZ point data (all referenced to mean sea level), combine the point data into a single set of X, Y, and Z vectors, and interpolate the point data onto the final combined topography/bathymetry grid used in our simulations.

A.6 1707 Hōei tsunami historical observations (Text S5)

We compare our simulated tsunami heights to historical observations of tsunami inundation from the 1707 Hōei earthquake. Historical seismologists have compiled descriptions of sites inundated by past tsunamis from old documents and monuments and conducted leveling surveys to determine historical flood elevations. We compare our simulations to a subset of historical observations from a compiled list of all observations from Hatori (1974), Hatori (1985), and Murakami et al. (1995), provided by Dr. Kentaro Imai. We only use observations that are within 1 km of the shoreline in order to avoid issues related to complexities in modeling overland flow. When multiple observations are clustered within 1 km of one another, we remove them if they differ by 100% or more, and we average them if they are generally consistent. For cases where one observation is located directly inland of another, we use the observation closer to the shoreline. To account for uncertainty in observation locations relative to grid positioning, we find all simulation grid points that are along the coast and within 1 km of each observation. This yields a set of ~5-10 model tsunami heights from each rupture scenario for comparison with the observation.

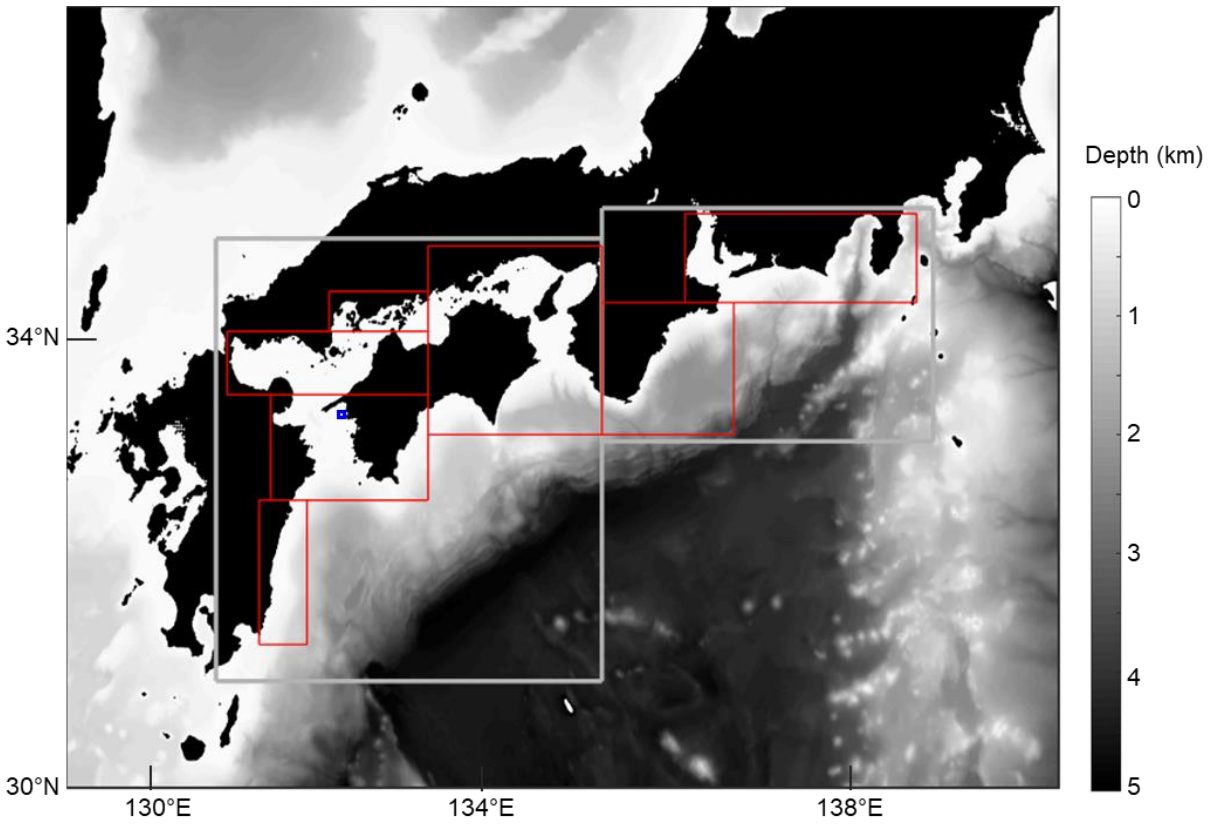

Figure A.1. Tsunami simulation domain and topography grids. A ~1,600 m-resolution topography grid covers the entire simulation domain, and resolution gradually increases to ~500 m (gray rectangles), ~100 m around the coastlines (red rectangles), and ~5 m around Lake Ryuuoo (blue rectangle).

APPENDIX B

CHAPTER 2 SUPPORTING INFORMATION

Table B.1 contains results of the Kendall's tau correlation test for the top 1% of skew surges and their associated predicted high waters (following Williams et al., 2016). Table B.2 contains details of the GPD threshold sensitivity test described in the main text.

Table B.1. Results of Kendall's tau correlation test, using the top 1% of skew surges and their associated predicted high waters.

	Summer		Winter	
	tau	p-value	tau	p-value
Eastport	0.02	0.59	-0.02	0.58
Portland	-0.01	0.80	-0.08	0.03
Boston	0.05	0.14	0.01	0.75

Table B.2. Threshold values and number of observations included in threshold sensitivity test (see Fig. 4 in main text).

Threshold percentile	Skew GPD (qn-SSJPM)		Storm tide GPD (GPD_{ST})	
	Threshold (m)	# Values above threshold	Threshold (m)	# Values above threshold
99.5	0.57	170	2.25	155
99.6	0.60	134	2.28	128
99.7	0.63	101	2.31	94
99.8	0.68	69	2.35	60
99.9	0.77	33	2.44	32

APPENDIX C

GREATER-BOSTON RESEARCH ADVISORY GROUP COASTAL FLOODING PROJECTIONS

C.1 Key Findings

- Most of Greater Boston's extreme flooding events are caused by winter storms (extratropical cyclones) coinciding with anomalous high tides. Recent studies have not found significant evidence for future changes in Greater Boston storm surge linked to changing storm climatology; however, sea level rise will substantially increase the frequency of extreme coastal flooding in the 21st century, regardless of the emissions scenario followed.
- Under all emissions scenarios, what is now a one in 10-year winter storm flood will likely become an annual event by mid-century. Flood projections begin to diverge under different emissions pathways around 2050. Beyond 2050, greenhouse gas emissions will determine if increasing flood hazard plateaus toward the end of the century (RCP2.6) or continues to accelerate. The equivalent of today's one in 100-year flood event will likely become an annual event by 2100 under RCP8.5.
- The height of the tide largely controls the severity of flooding during a given storm in Greater Boston. Tide range (the difference between low and high tide) varies year-to-year in the region as a function of natural planetary cycles, dominated by the 18.6-year lunar nodal cycle related to motion of the moon's elliptical orbit. Eight of Boston's top-ten historic flood events over the past 200 years (including two record-setting Nor'easters in January and March of 2018) occurred during a peak in this 18.6-year

cycle, demonstrating the need for tidal variability to be considered in Greater Boston flood projections.

- Future increases in flood hazard driven by sea level rise will plateau during decades when the lunar nodal cycle is in a negative phase and the reduced tide range counteracts sea level rise (2019-2017 and 2037-2046). However, as the nodal cycle enters a positive phase in the following decade (2028-2036 and 2047-2055), the larger tide range combined with sea level rise will accelerate the increase in flood hazard. Beyond mid-century, the influence of these tidal variations on flood projections becomes less important, as background sea level rise becomes the dominate control on flooding.
- Boston Harbor will see an increasing number of high tide 'nuisance' flooding days, defined as days when at least one hourly water level measurement exceeds local flooding thresholds defined by NOAA (215 cm above 2000 mean sea level for minor flooding or 241 cm for moderate flooding). Based on projections by Thompson et al. (2021), Boston's minor flood threshold will be exceeded on roughly half the days of each year by the early-2050s under the NOAA Intermediate sea level rise scenario (which is between median RCP4.5 and RCP8.5 sea level projections provided in this report). Under the NOAA Intermediate Low sea level rise scenario (similar to median RCP2.6 projections in this report), this will occur between 2070 and 2090. Boston's moderate flood threshold will be exceeded on half of days around 2070 under the NOAA Intermediate sea level rise scenario, but will only reach 48-87 exceedance days per year (10th-90th percentile range) by the end of the century (2100).
- Seasonal to decadal timescale sea level fluctuations unrelated to background sea level rise cause inevitable extreme months of clustered high tide flooding. Over 5-year

periods in Boston, the peak flooding month often experiences more than double the number of high tide flooding days than the average month. Thus, we reinforce that planning for the "typical" future month or year leads to substantial underestimation of flood hazard in the occasional, yet inevitable, periods of severe flooding, when cyclical contributions to sea level constructively interfere

C.2 Introduction

Relative sea level rise is increasing the frequency of coastal flooding on a global scale (e.g. Oppenheimer et al., 2019). Even under a regime of slow and steady sea level rise (SLR), flood frequency increases rapidly because lower-magnitude events with higher probabilities (i.e. routine storms that commonly impact the region) can cross flood thresholds on top of a higher baseline sea level (see Fig. C.1 for an illustration of this nonlinear response). Much of the discussion on specific mechanisms of coastal flooding in the 2016 BRAG report remains valid. Here, we use recent advances in flood hazard research to provide updated flood projections that incorporate the new probabilistic sea level rise scenarios presented above. Advances since the 2016 report include a reconstruction of Boston tidal and extreme water level measurements extending back to 1825 (Talke et al., 2018); statistical methods that incorporate the impact of Boston's large and time-varying tides on extreme flood frequencies (Baranes et al., 2020); updated extreme flooding projections for all of Massachusetts based on hydrodynamic modeling from Woods Hole Group; an improved understanding of mechanisms driving minor high tide flooding (also called "nuisance" flooding) in Boston (Ray & Foster, 2016); high tide flooding projections for Boston (Thompson et al., 2019; Sweet et al., 2018, 2020); and

regional projections for the impacts of future changes in storm climatology on flood heights for both extratropical (Lin et al., 2019) and tropic al cyclones (Marsooli et al., 2019).

Here, we 1) outline mechanisms of extreme coastal flooding in the Boston region; 2) describe the impacts of climatic and tidal variability on flood hazard; 3) provide context for two extreme flood events that impacted the region in January and March of 2018; and 4) provide projections of extreme flooding through 2100 at the location of the Boston tide gauge by combining the Baranes et al. (2020) methodology with probabilistic sea level rise projections. Lastly, we discuss mechanisms and recent projections of high tide "nuisance" flooding in Boston (e.g., Thompson et al. 2019; Sweet et al. 2020).

C.3 Mechanisms of coastal flooding

Extreme sea levels are caused by the combined impacts of rising sea level, high tides, storm surge, and waves. Storm surge is the rise in water level above the predicted tide, caused by storms centered off the coast driving ocean water toward land. Low atmospheric pressure, wave set-up, wave run-up, and rainfall can further contribute to observed storm-induced increases in water elevation (Harris and Bureau, 1963). The term storm tide refers to the combined impact of storm surge and the astronomical tide. Note the difference between peak measured high water and peak predicted high tide is defined as skew surge, which is often employed for developing flood statistics because the more standard storm surge term can include a partial dependence on tidal stage (e.g. (Williams et al., 2016).

The largest storm surge recorded in Boston over the last 100 years is 1.9 meters (e.g., (Catalano and Broccoli, 2018), and the largest recorded skew surge is 1.3 meters (Talke et al., 2018); however, the 3.1-meter rise and fall of sea level twice per day due to tides is significantly larger. Most of Boston's extreme coastal flooding events are therefore caused by the overlap of storm surge with an anomalously high tide (Baranes et al., 2020; Kirshen et al., 2008; Talke et al., 2018). This is in contrast to the south-facing shoreline of Massachusetts and New York City, where tide range is smaller and the most extreme storm surges are greater due to coastal orientation and morphology (Boldt et al., 2010; Castagno et al., 2020; Orton et al., 2012). Comparing the relatively minor flooding in Boston caused by Hurricane Sandy in 2012 to severe flooding during the January 4, 2018 Nor'easter (which set the record for highest water level recorded at the Boston tide gauge in 100 years) illustrates the relative impacts of high tide and storm surge on total flood height (Fig. C.2). Maximum storm surge during Hurricane Sandy was 50 cm higher than the 2018 event, yet maximum storm tide was 70 cm lower. This is because storm surge peaked around low tide during Sandy, whereas in 2018, peak surge coincided with a significantly larger-than-average high tide.

While multiple conditions can produce storms across the northeastern United States, the primary drivers of coastal flooding are large, synoptic-scale (hundreds of miles) atmospheric disturbances, or cyclones, with surface winds that rotate counter-clockwise around low-pressure centers. Cyclones can originate from various dynamic processes. Tropical cyclones (TCs) form at low latitudes over warm water where atmospheric conditions are favorable to convection. Near-surface winds spiral inward toward a low-pressure center and draw moisture from the ocean upward into the cyclone.

In the North Atlantic, tropical cyclones are called hurricanes once they reach a sustained wind speed of more than 74 mph. Extratropical cyclones (ETCs) form at mid-latitudes and are generally driven by latitudinal (north-south) temperature gradients that give rise to strong winds between cold and warm air masses. The term Nor'easter is commonly used in the Northeast to describe ETCs because the most damaging winds often come from the northeast on the western side of the passing low.

TCs impact the Northeast between August and October, while ETCs are most common in the cold-season months of November through April. ETCs have historically been the dominant flooding mechanism in Boston and the rest of northern New England, as they are 1) more frequent, 2) follow tracks more favorable to intense flooding north of Cape Cod, and 3) generally have longer durations that make them more likely to overlap with high tides (e.g. (Kirshen et al., 2008; Talke et al., 2018)). Along the south-facing shorelines of Massachusetts, Rhode Island, Connecticut, and New York, ETC-induced flooding is also most common for all but the most extreme flood events (Catalano and Broccoli, 2018). However, TCs have caused the largest historical flood events for locations like New York City (Talke et al., 2014), because of the region's coastal morphology, position relative to direct TC landfalls, and significantly smaller tidal range.

C.4 2018 Nor'easters

Extreme coastal flooding caused by two Nor'easters in 2018 illustrate the primary influence of tides in determining flood severity around Boston. Table C.1 describes the January 4th and March 3rd floods by various metrics; notably, the two storms caused the highest and third-highest water levels recorded within the ~100-year-long record from the

Boston National Oceanic and Atmospheric Administration (NOAA) tide gauge. Although sea level rise has increased the frequency of extreme flooding over the past century (Talke et al., 2018), adjusting the 100-year NOAA water level time series to annual MSL (i.e. comparing storm tides) only decreases the 2018 flood ranks from first and third to second and third (with the Blizzard of 1978 beating out the January 2018 Nor'easter in the annual MSL-adjusted storm tide time series). The metrics in Table C.1 also show that storm surge was not the primary cause of the record-breaking flooding, particularly for the January storm. The 0.85-meter January surge ranks 79th within the NOAA record (close to the annual storm), and the 1.08-meter March surge ranks 20th.

It was the unusually high tides coinciding with the storms that caused severe flooding in 2018. The two storms' timing was unfortunate in three respects: 1) they occurred in 2018, near the peak of the 18.6-year nodal cycle (Fig. C.3); 2) the January and March storms coincided with the 3rd and 12th-highest tides of the 2018 storm season respectively, which were 0.55 m and 0.43 m above the year's mean higher high water (MHHW; the average of the higher high tide for each day (Table C.1)); and 3) the timing of peak surge was nearly aligned with the timing of high tide during both events (Fig. C.2). Using the Baranes et al. (2020) methodology, which accounts for the known high tides in 2018, we calculate that there was only a 0.056% chance of both events occurring during that storm season; thus, although the storms themselves were not record-breaking, their timing relative to the anomalously large tides was unprecedented.

C.5 Climate-driven changes in extratropical and tropical cyclone characteristics

While there is evidence for future changes in ETC and TC activity globally, most recent studies have not found statistically significant evidence for future changes in Boston storm surge linked to either changing ETC (Lin et al., 2019) or TC (Marsooli et al., 2019) climatology.

Marsooli et al. (2019) uses a well-vetted hurricane and hydrodynamic model to generate a large number of representative North Atlantic TCs and resulting storm tides under both present (1980-2005) and late-21st-century (2070-2095, RCP8.5) conditions. These TC ensembles include changes in TC frequency, intensity, and size. Future changes in flood heights due solely to projected TC activity are compared to changes associated with both TC activity and future regional sea level rise based on the sea level rise projections by Kopp et al. (2014). TC contributions to increasing flood heights are found to be substantial along the Gulf and southern East Coast of the US; however, their contribution decreases northward along the eastern seaboard, particularly for points north of Cape Cod, where TC impacts become minimal. Specific to coastal counties in the greater-Boston region, changing TC activity accounts for roughly 1% of the total increase in the 100-yr flood height, with the remaining 99% due to projected sea level rise. The exception to this result is Plymouth County, where TC contributions increase to roughly 9%, mainly due to the fraction of the county being located south of Cape Cod at the head of Buzzards Bay, where the morphology and southern-facing orientation of the coast substantially enhances TC-induced storm surges (Boldt et al., 2010; Cheung et al., 2007; Redfield and Miller, 1957). TC-related contributions were found to be less for higher-

frequency events impacting Plymouth county, including a contribution of 2% to the 10-yr flood height.

Lin et al. (2019) investigates future climate-driven changes in ETC storm surge by comparing hydrodynamic simulations of Boston flooding for the historical (1979-2012) and mid-to-late-21st-century (2054-2079) periods. Results suggest a modest 5% increase in the 10-year storm surge height and a 1% increase in the 50-year storm surge height between the historical and future time periods due to changing ETC climatology. However, depending on the climate model used to define future ETC characteristics, results vary significantly with a range of -2% to +21% for the 10-year storm surge and -11% to +20% for 50-year storm surge.

C.6 Tidal variability and extreme flooding

Natural planetary cycles cause tidal magnitude (the vertical distance between high and low tide) to vary year-to-year in Boston, enhancing flood hazard in years when tides are larger (Baranes et al., 2020; Eliot, 2010; Haigh et al., 2020; Peng et al., 2019; Ray and Foster, 2016; Talke and Jay, 2020; Talke et al., 2018; Woodworth et al., 2019). The moon's elliptical orbit revolving in space (the lunar nodal cycle) causes Boston's largest high tides to cyclically increase and decrease by ~7 cm (just under a quarter foot) every 18.6 years (Ray and Merrifield, 2019), which is roughly equivalent to 25% of the total relative sea level rise that has occurred in Boston over the last 100 years. Eight of Boston's top-ten storm tides over the past 200 years have occurred during decades when the 18.6-year nodal cycle's positive phase forces a larger tidal range (Fig. C.3; Talke et al., 2018).

There has also been a secular increase in tide range throughout the Gulf of Maine (the basin between Cape Cod and the Bay of Fundy), widening the difference between low and high tide elevations by a few (~ 4cm) in Boston over this past century (Godin, 1992, 1995; Ray, 2006; Ray and Foster, 2016; Ray and Merrifield, 2019). The increase in tides has increasing impact north of Boston toward the Bay of Fundy. In Greater Boston, future flood risk is dominated by projected rates of background sea level rise followed by secondary impacts associated with the nodal cycle (Baranes et al., 2020).

Recent work by Baranes et al. (2020) focusing on Boston and the greater Gulf of Maine region presents a new statistical approach for assessing flood hazard that accounts for tidally driven interannual variability associated with the 18.6-year nodal cycle. The technique demonstrates the effect of the nodal cycle in driving significant historical oscillations in flood hazard metrics, such as the height of the 100-year flood. Interaction between the nodal cycle and sea level rise also has significant implications for future flood hazard in Boston. Currently (in 2020), the negative phase of the nodal cycle is counteracting the sea level rise-induced increase in flood hazard; however, in 2025, the nodal cycle will reach a minimum in the region and then begin to accelerate flood hazard as it moves toward its maximum over the subsequent decade when both sea level rise and larger tides are constructional.

C.7 Future Flooding

C.7.1 Methods

Similar to the 2016 BRAG report, the frequency of extreme coastal flood heights at the Boston tide gauge are projected under three future RCP emission scenarios:

RCP2.6, RCP4.5, and RCP8.5. Probabilistic sea level rise projections for each scenario are combined with future predicted high tides and tide gauge-derived extreme value statistics of skew surge. Like many tide gauges, the Boston gauge is located in a wave-sheltered harbor and measures the contributions of storm surge, tides, and mean sea level to flood level but excludes direct wave impacts. Thus, the projections provided here are for extreme still water levels and do not include waves. These projections also do not include seasonal-to-decadal fluctuations in sea level caused by temperature, salinity, wind, atmospheric pressure, and ocean currents (see the "Minor High Tide Flooding" section for a more in-depth discussion of these drivers of sea level variability).

We substantially improve upon the 2016 BRAG projections by applying a quasi-nonstationary joint probability approach (Baranes et al., 2020) that 1) provides more accurate estimates of annual flood exceedances, which is the expected number of times extreme sea levels will exceed a given height in a year; and 2) yields an annually varying flood height–annual exceedance relationship (hereafter referred to as a "flood exceedance curve") that changes based on the predicted tides for each year. Note that exceedances/year is the inverse of recurrence interval (or return period); for example, the storm tide with a 100-year recurrence interval has 0.01 expected exceedances/year.

We also separate winter and summer season projections because the region's large storm events mostly occur in the winter season (Talke et al., 2018), while summertime tide levels are larger on average (Ray and Foster, 2016). At present, the summer season contribution to annual extreme flood hazard is negligible (Fig. C.4; Baranes et al., 2020), so it is important to view full-year flood exceedance curves for Boston with that caveat in mind. We define the winter storm season as October 31 to

April 30 and the summer season as May 1 to October 20 (consistent with Talke et al., 2018 and Baranes et al., 2020).

The joint probability approach employed here fits separate probability distributions to predicted high tides and the 100-year record of skew surge from the Boston NOAA tide gauge following methods in Baranes et al. (2020). The joint tide-surge distribution thus accounts for the possibility of storm surges aligning with any tidal condition. Projections are quasi-nonstationary because each future year's flood exceedance curve is calculated by combining projected mean sea level and tides specific to that year with the probability distribution fit to all historical skew surges observed over the 100-year NOAA record. Annual tide predictions at the Boston gauge for 1921-2100 are from Ray and Foster (2016). Thus, we allow tides and sea level to vary through time but consider storm characteristics to be stationary. This approach reflects our assessment that 1) future impacts to the Boston region by changes in extratropical and tropical cyclone activity are at present considered minimal, albeit with ongoing uncertainty (see above); and 2) the largest drivers of future change in coastal flood hazard are sea level rise and natural tidal cycles.

Uncertainty ranges in our projections include both statistical uncertainty in the skew surge distribution that characterizes their probabilities based on a limited 100-year record of observations, and probabilistic uncertainty in sea level rise projections. As discussed in Douglass et al. (2016), using probabilities of sea level rise in flood risk assessment is extremely important because uncertainty in background sea level increases the median estimate of extreme flood levels. Steady sea level rise forces a nonlinear increase in flood hazard (Fig. C.1), so the number of additional flood exceedances

introduced by the possibility of larger-than-expected sea level rise is greater than the reduction in flood exceedances due to smaller-than-expected sea level rise.

Statistical uncertainty in the skew surge distribution is represented by 1,000 Generalized Pareto Distributions (GPDs) with equal probabilities, while sea level rise uncertainty is represented by 10,000 scenarios with equal probabilities under each RCP. For each season (summer and winter) and for each RCP, we 1) use a Latin hypercube sampling scheme to sample 1,000 sets of skew surge GPDs and sea level rise scenarios, 2) add the 1,000 selected sea level rise scenarios to future predicted tides, and 3) calculate annually varying flood exceedance projections for each of the 1,000 selected GPD and sea level rise projection sets (Baranes et al., 2020).

C.7.2 Flood projections

Fig. C.5 shows historical (1921-2019) and projected (2020-2100) winter and summer season flood heights for the 10-year flood (0.1 expected exceedances/year) and the 100-year flood (0.01 expected exceedances/year). An illustration of the 18.6-year tidal modulation of storm tides is plotted below the flood height curves in each panel of Fig. C.5. Tables C.2 and C.3 show present-day and projected flood heights, averaged over each nodal cycle phase (labeled present, 1-, 1+, 2-, etc. in Fig. C.1; with minus and plus signs denoting negative and positive nodal phases). Note that present-day flood levels are determined by averaging over 2000–2019, a 19-year period that encompasses a full 18.6-year nodal cycle. All flood heights are relative to 2000 MSL.

Sea level rise has clearly been driving an accelerating increase in flood hazard since the early-20th century. Flood projections do not begin to diverge under different

emissions pathways until about 2050, after which human decision-making determines whether the increase in flood hazard plateaus at the end of the century (RCP2.6), or continues to accelerate (RCP8.5). The decadal, cyclical variation in flood heights through 2100 also demonstrates the impact of the 18.6-year nodal cycle on flood hazard. Importantly, the long-term increase in flood hazard driven by sea level rise temporarily plateaus during decades when the nodal cycle is in a negative phase, and the smaller tide range counteracts sea level rise. However, as the nodal cycle enters a positive phase in the following decade, the increased tide range on top of sea level rise leads to a more rapid increase in flood hazard. Progressing forward from present (year 2020), the nodal cycle will be in a negative phase until 2027, so flood hazard will remain steady compared to the previous decade even though sea level is continuing to rise. However, one should expect flood hazard to increase more rapidly over the 2028-2036 decade when the nodal cycle switches to its positive phase. Fig. C.5 also shows a 4.4-year cycle of variation in the 10 and 100-year flood heights. This is also due to predictable interannual variation in the magnitude of Boston's tides, caused by perigean spring tides coinciding with the winter or summer solstice on a 4.4-year cycle (see Ray & Foster, 2016 for a detailed explanation). We do not focus on this 4.4-year effect because in practice, it would be drowned out by inter-annual variability in MSL, which has historically been on the order of several cm (Baranes et al., 2020).

Tables C.4 and C.5 provide guidance on the annual exceedances of future flood levels (we use 2.6–3.0 m for the winter season and 2.4–2.7 m for the summer season relative to 2000 MSL) that currently have recurrence intervals between ~10 and ~100 years under low and high-emissions scenarios. The tables show the central 66% “likely”

range of projected annual exceedances (where, for example the 100-year flood has 0.01 expected annual exceedances), and do not extend beyond exceedances of 1 (i.e. the annual event). As an example, it is projected that for the period between 2047-2055 (nodal cycle "2+"), the present-day winter season 100-year flood (at ~3 m above 2000 MSL) will likely have a recurrence interval of 6-to-33 years under the low-emissions RCP2.6 scenario (0.03-0.18 annual exceedances), and 3-to-20 years under the RCP8.5 high-emissions scenario (0.05-0.38 annual exceedances), where recurrence interval is the inverse of annual exceedances (Tab. C.4). By 2100, this same 3-m flood level will likely be the annual event under RCP8.5 (0.85 to >1 annual exceedances), or between the annual and 14-year event under RCP2.6 (0.07 to >1 annual exceedances). Note that the projected range of exceedances in Tables C.2 and C.3 can be wide because at extreme flood levels in Boston, small changes in flood height lead to large variation in exceedances (Buchanan et al., 2016).

C.7.3 Comparison with BRAG

Table C.6 compares projections of the winter 100-year flood height from this report to projections from the 2016 BRAG report (Table 2-1 in Douglas et al., 2016). The winter season flood exceedance curve almost exactly matches the annual curve (Fig. C.4), supporting our comparison of winter season results to the annually derived statistics in BRAG. It is important to note that the 2016 report provided mean projected flood heights, whereas in Tables C.2 and C.3, we provide median (50th percentile) flood heights. As explained above, the number of additional flood exceedances introduced by the possibility of larger than expected sea level rise is not offset by the reduction of

exceedances introduced by the possibility of smaller than expected sea level rise, even if the sea level rise distribution is near-normal; thus, those additional positive exceedances will cause mean projected flood heights to exceed the median. Differences between median and mean values are generally within a few cm, reaching a maximum of 4 cm at the end of the 21st century under RCP8.5.

Our present-day 100-year flood height estimate is slightly higher in part due to our including the two 2018 nor'easters in our extreme value statistical analysis. Through 2050, our projected flood heights are higher than the 2016 projections (2–16 cm higher under RCP4.5 and 5-26 cm for RCP8.5), whereas in 2100, our projections are lower (16-20 cm lower for RCP4.5 and 8-59 cm for RCP8.5). As discussed above, these differences are mainly caused by our revised GBRAG baseline sea level projections that use updated land ice contributions provided by IPCC SROCC (Oppenheimer et al., 2019). In 2030 and 2050, the nodal cycle is in its positive phase which also contributes to higher GBRAG flood projections.

C.7.4 Hydrodynamic models

In this report, we estimate extreme flood frequencies by fitting probability distributions to measured skew surges at the Boston tide gauge and combining those distributions with tide predictions and probabilistic sea level projections. Flood frequencies can also be estimated from hydrodynamic model simulations of water levels (Lin et al., 2019; Marsooli et al., 2019). Hydrodynamic modeling has the advantages of 1) providing spatially continuous flood elevations and flow velocities down to the spatial scales (<1 m) relevant to specific infrastructure such as roads and bridges, 2) explicitly

modeling wave impacts, 3) accounting for nonlinear impacts on tides and surge from rising sea level, and 4) considering potential changes in storm climatology. However, these models are computationally intensive (particularly when implemented at the infrastructure scale), and as is the case with most numerical models, rely on uncertain parameterizations, bathymetry, and assumptions (Lin et al., 2010; Vousdoukas et al., 2016). Furthermore, generating a modeled flood exceedance distribution requires an ensemble of many simulations representing essentially all possible flood scenarios. Thus, individual flood statistics at infrastructure and community scales for the entire Greater Boston region is currently only feasible by combining hydrodynamic modeling ensembles with a limited set of tidal conditions and discrete sea level scenarios, rather than full sets of probabilistic sea-level projections.

The Massachusetts Coast Flood Risk Model (MC-FRM) is currently the most sophisticated hydrodynamic model for assessing future changes in flood hazard along the Massachusetts coastline due to the combination of sea level rise and changing storm climatologies. The MC-FRM was developed by Woods Hole Group for the Massachusetts Department of Transportation and is an expansion of the Boston Harbor Flood Risk Model (Bosma et al., 2015). MC-FRM simulations are in progress, and results are being distributed through MassDOT, Massachusetts CZM, and MassGIS as they become available. The U.S. Army Corps of Engineers North Atlantic Coast Comprehensive Study (NACCS) also provides hydrodynamic modeling-based flood statistics for the greater-Boston area (Nadal-Caraballo et al., 2015). However, the NACCS only considers a 1-m sea level rise scenario, and its domain includes Virginia

through Maine, so the model is not optimized for Massachusetts like the MC-FRM. Thus, we focus our discussion on the MC-FRM.

The MC-FRM is a coupled ADCIRC-UNSWAN model that includes the impacts of sea level, tides, storm surge, wave setup, riverine flows, and dam operations on coastal flooding. Its domain includes all Massachusetts coastlines and estuaries and has spatial resolution reaching 5-10 feet in populated overland regions. The model also includes dynamic run-up and accounts for overtopping of coastal structures such as seawalls. MC-FRM results provide flood heights and flood frequencies across the model domain for the present-day and for future horizons in 2030, 2050, and 2070.

The model uses 99.5^{th} percentile RCP8.5 relative sea level rise projections because it evaluates MassDOT critical infrastructure, such as Boston's central artery highway/tunnel system. Baseline sea level projections used in the MC-FRM analysis are shown in Table C.6 and are the same as those in Kopp et al. (2017). For practitioners using both MC-FRM flood projections (as they become available) and the GBRAG projections provided here, we compare baseline sea levels at 2030, 2050, and 2070 relative to both the MC-FRM and GBRAG vertical datums (feet above NAVD88 and meters above 2000 MSL, respectively). We offer this comparison of baseline sea levels because GBRAG sea level projections are considerably higher than those used by the MC-FRM beyond 2030. Note, however, that it is not appropriate to compare the two sets of flood projections, as the MC-FRM is designed to give a detailed assessment of a few discrete scenarios, whereas GBRAG projections are designed to describe all possible scenarios at a single location.

For each future climate horizon, the MC-FRM evaluates flooding from both TCs and ETCs. Modeled ETCs are based on storms observed within instrumental and historical records, an approach that is consistent with our evaluation of there being no clear evidence for future changes in extratropical frequency or intensity. Modeled TCs, however, are drawn from a set of over 500,000 synthetic storms with characteristics that vary over time as climatological conditions change, following a similar methodology to Marsooli et al., (2019). MC-FRM and Marsooli et al. (2019) are consistent in their projections for future increases in tropical cyclone activity contributing to the increase in future flood hazard along Massachusetts' south-facing shorelines, where TCs are the primary cause of severe flooding.

For ETC simulations, the MC-FRM randomly phases storms with the tidal cycle such that flood projections account for the possibility of peak storm surge occurring over a range of tidal levels. However, the modeled tides used in the MC-FRM are from a single month in 2008. The 2018 Nor'easters demonstrated that the height of high tide on the particular day a storm hits is an important determination of flood severity. Therefore, proper statistical representation of 2018-type events requires sampling from a full nodal cycle (18.6 years) of tidal conditions. This is not computationally feasible for a hydrodynamic modeling study with a storm set as large as the MC-FRM's.

Compared with hydrodynamic model-based projections, the tide gauge-based flood projections (Fig. C.5, Tables C.2-C.5) have the advantages of 1) incorporating full probability distributions of sea level rise under multiple emissions scenarios, 2) providing a statistically robust treatment of tides, and 3) being grounded in observations. However, the analysis only provides flood hazard information at a single wave-sheltered location

(the Boston tide gauge). These GBRAG tabulated flood heights can be used for decision-making near the tide gauge and as validation for hydrodynamic flood modeling. The MC-FRM results also have the potential to provide complementary guidance on the impact of waves and spatial variability in flood magnitude between the Boston tide gauge and specific locations of interest within the Greater Boston domain. At present, there are no flood projections that are both spatially continuous and fully probabilistic. Synthesizing computationally expensive hydrodynamic model output with more complete (statistically based) tidal and sea level rise distributions is an ongoing area of research that will improve flood projections in the future.

C.7.5 Minor high tide flooding

High tide flooding, also often called "nuisance" flooding, is defined as more routine, low-magnitude flooding that is not a serious threat to public safety, but can overwhelm stormwater drainage systems, close roads, and deteriorate infrastructure not designed to be submerged or exposed to salt (Moftakhari et al., 2015; Sweet et al., 2020; Sweet et al., 2018; Sweet and Park, 2014; Thompson et al., 2021). In Boston, the NOAA-defined threshold for minor high tide flooding is 63 cm above the present mean higher high water (MHHW) datum (where "present" is the 1983-2001 average), or 215 cm above 2000 MSL[1]. The Boston moderate flooding threshold is 89 cm above present MHHW.

[1] This threshold is based on an empirical relationship between tide range and high tide flooding, which was developed by NOAA for consistently determining minor flood thresholds across U.S. tide gauges (Sweet et al., 2018). The estimated 62.5-cm Boston threshold for nuisance flooding is used in recently published projections (Thompson et al., 2019; Sweet et al., 2020); however, an observation-based Boston minor flood threshold of 68 cm above MHHW has also been established by the NOAA National Weather Service (NWS) Weather Forecasting Office (WFO) based on available flood observations for the city. This 68-cm threshold is used in Sweet et al. (2014), Spanger-Siegfried et al. (2014), and Ray & Foster (2016); however,

Astronomical (i.e. tidal) and climatic processes that modulate sea level over seasonal to decadal timescales control the frequency of high tide flooding. In Boston, the relative amplitudes of the major tidal constituents cause high tide flooding events to occur most often around the summer solstice (see Ray & Foster, 2016 for a detailed explanation). On interannual timescales, the 18.6-year nodal cycle (Fig. C.3) and the 4.4-year cycle of lunar perigee, caused by perigean spring tides coinciding with the winter or summer solstice twice per 8.85 years, also cause high tide flood events to cluster in certain years when the two cycles constructively interfere to increase high tide levels (Ray and Foster, 2016; Thompson et al., 2019, 2021). Interannual and higher-frequency fluctuations in temperature, salinity, wind, atmospheric pressure, and ocean currents also change sea level and impact the timing of flooding (e.g. Thompson et al., 2021). For example, at the Boston Harbor tide gauge, the present amplitude of the seasonal sea-level cycle is ~3.5 cm (such that June sea level is ~7 cm higher than January sea level). On decadal timescales, Boston sea level can vary by an additional 10-15 cm. However, it is difficult to attribute this longer-timescale variability to a particular forcing mechanism because multiple, interacting processes are at play (Sweet et al., 2009).

The long-term secular increase in sea level rise underlies all above-mentioned cyclical variations in water level and is accelerating the frequency of high tide flood events (see Fig. C.1 for an explanation of the nonlinear flood response). In Boston, 2011 was the first year that spring high tides alone exceeded the city's local nuisance flood threshold without the additional influence of storms. Using the empirical, 63-cm

NOAA prefers the empirically derived, nationally consistent threshold because local thresholds are often only valid in particular parts of a city (Sweet et al., 2018).

threshold, Sweet et al. (2020) found that in 2017, near the peak of the 18.6-year nodal cycle, Boston experienced a record-breaking 22 high tide flood events. In 2019, the nodal cycle entered its negative phase, and they found that high tide flood events were reduced to 7 flood days in 2019 and a projected 11-18 flood days in 2020.

Thompson et al. (2021) provide the best available projections of future high tide flooding at 89 U.S. tide gauge locations, including Boston. They combine three discrete sea level rise scenarios with localized ensemble projections of 21st century monthly mean sea level and astronomical tides. Sea level projections are the NOAA Intermediate Low, Intermediate, and Intermediate High local relative sea level rise scenarios for Boston, which include local effects of glacial isostatic adjustment and gravitational and rotational effects from ice melt (Sweet et al., 2017; Supplemental dataset 1). In comparison with updated projections provided in this report, the NOAA Intermediate Low scenario is similar to our median (50th percentile) RCP2.6 projections, and the NOAA Intermediate and Intermediate High scenarios fall between our median RCP4.5 and RCP8.5 projections. Thompson et al. (2021) high tide flooding projections therefore account for sea level rise and daily-to-decadal timescale sea level variability driven by tides, atmosphere-ocean dynamics, and internal climatic variability. Note that the projection ensembles do not represent the full range of uncertainty in flooding given that each ensemble only considers a single sea level rise scenario (rather than a set of probabilistic projections, such as those provided in this report).

Figure C.6 shows projections of high tide flooding days per year (i.e. days where at least one hourly sea level value exceeds a flood threshold) at the location of the Boston tide gauge. Projections for the NOAA Intermediate Low and Intermediate sea level rise

scenarios are included for both the NOAA minor and moderate flood thresholds (Supplemental dataset X contains tabulated annual projections and includes the additional NOAA Intermediate High sea level rise scenario). Under all sea level rise scenarios, Boston can expect an acceleration in the number of high tide flooding days throughout the century. Boston's minor flood threshold will be exceeded on roughly half the days of each year by the early-2050s under the NOAA Intermediate sea level rise scenario. Under the Intermediate Low scenario, this will occur between 2070 and 2090. Boston's moderate flood threshold will be exceeded on half of days around 2070 under the Intermediate sea level rise scenario, but will only reach 48-87 exceedance days per year (10^{th}-90^{th} percentile range) by the end of the century (2100).

Thompson et al. (2021) define the year of inflection as the year marking a transition from a regime of gradually increasing flooding to one of rapidly increasing flooding. They identify the decade that experiences a quadrupling or more of the number of high tide flooding days compared to the prior decade, based on the 50^{th} percentile curve from each projection ensemble. The year of inflection divides these two decades, and Thompson et al. suggest that it should be a decision point for updating policy and management strategies to prepare for future rapid increases in flooding.

Under the NOAA Intermediate Low sea level rise scenario, the year of inflection is 2041 for the minor flood threshold and 2059 for the moderate flood threshold. The number of high tide flooding days per year increases by 39 days for the minor threshold and 22 days for the moderate threshold in the decade following the year of inflection. Under the NOAA Intermediate sea level rise scenario, years of inflection are 2023 for the minor threshold and 2041 for the moderate threshold. Annual high tide flooding days

increase by 46 days per year for both thresholds in the decade following the year of inflection. In Boston, the 18.6-year nodal cycle strongly modulates interannual variation in high tide flooding (Fig. C.6). Years of inflection for all scenarios therefore occur near nodal cycle minima, where tide range is near its minimum and will increase over the subsequent decade.

Seasonal to decadal timescale sea level fluctuations unrelated to background sea level rise cause inevitable extreme months of clustered high tide flooding (Thompson et al., 2019, 2021). Given that high tide flooding impacts are cumulative in nature (Moftakhari et al., 2017, 2018; Ghanbari et al., 2020), only considering projected high tide flooding days per year (or per some longer time interval) for decision-making will underestimate flood impacts during extreme months (Thompson et al., 2021). In addition to annual projections, Thompson et al. therefore also provide projections of high tide flooding days per month for both an average month and the most extreme month in each future 5-year period (Fig. C.7; Supplemental Data X). Over 5-year periods in Boston, the peak flooding month often experiences more than double the number of high tide flooding days than the average month. Thus, we reinforce that planning for the "typical" future month or year leads to substantial underestimation of flood hazard in the occasional, yet inevitable, periods of severe flooding, when cyclical contributions to sea level constructively interfere (Thompson et al., 2019, 2021).

C.8 Outlook and Ongoing Challenges

Sea level and flooding projections continue to evolve as illustrated by the difference between this GBRAG assessment and the previous BRAG report.

Reliable flood projections in Greater Boston must properly account for tidal variation while incorporating the most up-to-date sea level guidance. We provide such projections at a single location (the Boston Harbor tide gauge); however, these projections have three important disadvantages: 1) they become less reliable with increasing distance from the tide gauge, 2) the methodology is not directly applicable to wave-effected areas, and 3) they do not account for nonlinear impacts on tides and storm surge from rising sea level.

Meteorologic-hydrodynamic models can provide spatially continuous flood hazard information at fine spatial scales, while accounting for waves and nonlinear interactions among tides, surge, and sea level. However, they are too computationally intensive to incorporate probabilistic sea level rise (i.e. the full range of possible sea level scenarios, rather than a few discrete scenarios) and sufficient assessment of the timing of storms relative to tides. Hybrid methods are required that provide the spatial coverage of detailed hydrodynamic modeling studies, while taking advantage of computationally inexpensive probabilistic approaches that jointly combine tide-surge probabilities with updated sea level rise projections and associated uncertainties.

Table C.1. Metrics describing the two Nor'easters that caused record-breaking flooding on the Massachusetts coast during the winter of 2018.

	January 4, 2018 Nor'easter	March 3, 2018 Nor'easter
Storm tide, m above 2018 MHHW m above 2018 MSL	1.36 m 2.95 m	1.22 m 2.81 m
Storm tide rank, 1921-2020 (i.e. not including SLR)	2	3
Total water level rank, 1921-2020 (i.e. including SLR)	1	3
Maximum storm surge	0.85 m	1.08 m
Storm surge rank, 1921-2020	79	20
Predicted high water at peak storm tide, m above 2018 MHHW m above 2018 MSL	 0.55 m 2.14 m	 0.43 m 2.02 m
Predicted high water rank, 2018 winter storm season	3	12

Table C.2. Projections of 10-year and 100-year **winter** flood heights, averaged across each nodal cycle phase (see Fig. C.4). We show median flood heights and central 90% ranges (values in parentheses). All flood heights are in meters above 2000 MSL.

		Heights for 10-y **winter** flood (m, 2000 MSL)			Heights for 100-y **winter** flood (m, 2000 MSL)		
Nodal period	Years	RCP2.6	RCP4.5	RCP8.5	RCP2.6	RCP4.5	RCP8.5
Present	2000–2018	2.66 (2.61– 2.71)			2.96 (2.88– 3.08)		
1-	2019–2027	2.74 (2.66–2.83)	2.74 (2.66–2.82)	2.75 (2.65–2.86)	3.04 (2.93–3.19)	3.04 (2.94–3.18)	3.05 (2.93–3.21)
1+	2028–2036	2.83 (2.71–2.96)	2.83 (2.72–2.95)	2.85 (2.72–3.00)	3.13 (2.99–3.31)	3.13 (3.00–3.30)	3.15 (3.00–3.34)
2-	2037–2046	2.86 (2.71–3.03)	2.87 (2.74–3.03)	2.91 (2.74–3.11)	3.17 (3.00–3.37)	3.18 (3.02–3.37)	3.21 (3.03–3.44)
2+	2047–2055	2.95 (2.75–3.17)	2.98 (2.80–3.19)	3.04 (2.83–3.31)	3.26 (3.05–3.51)	3.28 (3.09–3.53)	3.34 (3.12–3.64)
3-	2056–2064	2.98 (2.74–3.24)	3.02 (2.80–3.29)	3.11 (2.94–3.46)	3.28 (3.03–3.56)	3.33 (3.10–3.62)	3.42 (3.15–3.78)
3+	2065–2074	3.06 (2.80–3.36)	3.14 (2.87–3.47)	3.27 (2.97–3.72)	3.37 (3.09–3.69)	3.44 (3.16–3.80)	3.57 (3.24–4.04)
4-	2075–2083	3.08 (2.79–3.42)	3.18 (2.86–3.58)	3.36 (3.27–3.92)	3.38 (3.08–3.75)	3.48 (3.15–3.90)	3.67 (3.27–4.24)
4+	2084–2091	3.14 (2.82–3.55)	3.27 (2.90–3.74)	3.51 (3.05–4.19)	3.45 (3.11–3.87)	3.57 (3.20–4.06)	3.82 (3.35–4.50)
5-	2092–2100	3.17 (2.82–3.60)	3.32 (2.91–3.84)	3.61 (3.09–4.40)	3.47 (3.11–3.92)	3.62 (3.21–4.16)	3.92 (3.39–4.72)

Table C.3. Projections of 10-year and 100-year **summer** flood heights, averaged across each nodal cycle phase (see Fig. C.4). We show median flood heights and central 90% ranges (values in parentheses). All flood heights are in meters above 2000 MSL.

		Heights for 10-y **summer** flood (m, 2000 MSL)			Heights for 100-y **summer** flood (m, 2000 MSL)		
Nodal period	Years	RCP2.6	RCP4.5	RCP8.5	RCP2.6	RCP4.5	RCP8.5
Present	2000–2018	2.43 (2.36– 2.50)			2.69 (2.59– 2.85)		
1-	2019–2027	2.50 (2.41–2.59)	2.49 (2.41–2.58)	2.50 (2.40–2.61)	2.75 (2.64–2.93)	2.75 (2.64–2.92)	2.76 (2.63–2.95)
1+	2028–2036	2.58 (2.45–2.72)	2.58 (2.47–2.72)	2.60 (2.46–2.77)	2.85 (2.69–3.05)	2.85 (2.70–3.05)	2.87 (2.70–3.09)
2-	2037–2046	2.61 (2.45–2.79)	2.62 (2.48–2.79)	2.66 (2.49–2.87)	2.88 (2.69–3.11)	2.89 (2.72–3.12)	2.93 (2.73–3.18)
2+	2047–2055	2.71 (2.51–2.93)	2.73 (2.55–2.96)	2.79 (2.59–3.08)	2.98 (2.75–3.24)	3.00 (2.80–3.28)	3.06 (2.83–3.38)
3-	2056–2064	2.74 (2.50–3.00)	2.79 (2.56–3.06)	2.87 (2.61–3.23)	3.00 (2.74–3.30)	3.05 (2.81–3.36)	3.14 (2.87–3.52)
3+	2065–2074	2.82 (2.55–3.12)	2.89 (2.61–3.24)	3.02 (2.69–3.48)	3.09 (2.80–3.42)	3.16 (2.87–3.53)	3.29 (2.94–3.77)
4-	2075–2083	2.84 (2.54–3.19)	2.94 (2.62–3.35)	3.12 (2.74–3.69)	3.11 (2.79–3.48)	3.21 (2.87–3.63)	3.40 (2.99–3.97)
4+	2084–2091	2.91 (2.58–3.31)	3.03 (2.66–3.51)	3.27 (2.82–3.96)	3.18 (2.83–3.60)	3.31 (2.92–3.80)	3.54 (3.07–4.24)
5-	2092–2100	2.92 (2.57–3.36)	3.08 (2.67–3.60)	3.37 (2.85–4.17)	3.20 (2.82–3.64)	3.35 (2.92–3.89)	3.64 (3.09–4.44)

Table C.4. Projections of winter season annual exceedances for flood heights of 2.60 m (roughly the present-day 10-year flood height), 2.80 m, and 3.00 m (roughly the present-day 100-year flood height). Flood heights are relative to 2000 MSL, and ranges of exceedances represent the central 66% "likely" range. Note that "annual" represents an exceedance value greater than or equal to 1.

		2.60 m		2.80 m		3.00 m	
Nodal period	Years	RCP2.6	RCP8.5	RCP2.6	RCP8.5	RCP2.6	RCP8.5
Present	2000–2018	0.13–0.19		0.03–0.04		0.004–0.011	
1-	2019–2027	0.20–0.43	0.19 – 0.47	0.04–0.10	0.04–0.11	0.01–0.02	0.01–0.02
1+	2028–2036	0.32–ann.	0.35–ann.	0.07–0.21	0.08–0.27	0.01–0.05	0.02–0.06
2-	2037–2046	0.35–ann.	0.47–ann.	0.08–0.32	0.10–0.49	0.02–0.07	0.02–0.11
2+	2047–2055	0.57–ann.	annual	0.12–0.81	0.22–ann.	0.03–0.18	0.05–0.38
3-	2056–2064	0.56–ann.	annual	0.12–ann.	0.30–ann.	0.03–0.25	0.07–0.87
3+	2065–2074	annual	annual	0.21–ann.	0.71–ann.	0.05–0.56	0.16–ann.
4-	2075–2083	0.98–ann.	annual	0.21–ann.	annual	0.05–0.72	0.24–ann.
4+	2084–2091	annual	annual	0.29–ann.	annual	0.06–ann.	0.52–ann.
5-	2092–2100	annual	annual	0.31–ann.	annual	0.07–ann.	0.85–ann.

Table C.5. Projections of summer season annual exceedances for flood heights of 2.40 m (roughly the present-day 10-year flood height), 2.55 m, and 2.70 m (roughly the present-day 100-year flood height). Flood heights are relative to 2000 MSL, and ranges of exceedances represent the central 66% "likely" range. Note that "annual" represents an exceedance value greater than or equal to 1.

		2.40 m		2.55 m		2.70 m	
Nodal period	Years	RCP2.6	RCP8.5	RCP2.6	RCP8.5	RCP2.6	RCP8.5
Present	2000–2018	0.09–0.19		0.02–0.05		0.005–0.015	
1-	2019–2027	0.17–0.77	0.17 – 0.98	0.03–0.10	0.03–0.12	0.01–0.02	0.01–0.03
1+	2028–2036	0.37–ann.	0.44–ann.	0.06–0.41	0.07–0.66	0.02–0.06	0.02–0.09
2-	2037–2046	0.48–ann.	0.88–ann.	0.07–0.90	0.11–ann.	0.02–0.11	0.02–0.22
2+	2047–2055	annual	Annual	0.17–ann.	0.47–ann.	0.03–0.58	0.07–ann.
3-	2056–2064	annual	annual	0.18–ann.	annual	0.04–ann.	0.13–ann.
3+	2065–2074	annual	annual	0.41–ann.	annual	0.07–ann.	0.50–ann.
4-	2075–2083	annual	annual	0.47–ann.	annual	0.07–ann.	annual
4+	2084–2091	annual	annual	annual	annual	0.13–ann.	annual
5-	2092–2100	annual	annual	annual	annual	0.13–ann.	annual

Table C.6. Comparison of 10th-90th percentile 100-year flood height projections in BRAG (2016) and GBRAG (2021). BRAG values are reported in feet relative to NAVD88 and meters relative to 2000 MSL while GBRAG values are only reported in meters relative to 2000 MSL. We also compare median (50th percentile) sea level estimates, with positive values indicating higher GBRAG estimates and negative values indicating higher BRAG estimates.

		2016 BRAG 100-y flood height 10th – 90th percentile		2020 GBRAG Winter 100-y flood height 10th – 90th percentile	50th percentile sea level rise difference (GBRAG minus BRAG, m)	Nodal cycle phase
		ft, NAVD88	m, 2000 MSL	m, 2000 MSL		
Present		9.2	2.87	2.88–3.08		
2030	RCP4.5	9.5–10.1	2.96–3.14	3.03–3.28	+0.04	Positive
	RCP8.5	9.5–10.1	2.96–3.14	3.02–3.32	+0.05	
2050	RCP4.5	9.8–10.8	3.05–3.35	3.07–3.51	+0.02	Positive
	RCP8.5	9.8–10.8	3.05–3.35	3.10–3.61	+0.01	
2100	RCP4.5	10.8–14.1	3.35–4.36	3.19–4.16	-0.37	Neutral
	RCP8.5	12.1–17.4	3.75–5.37	3.67–4.78	-0.44	

Table C.7. Comparison of relative sea level rise projections used by MC-FRM (based on (Kopp et al., 2017) and those developed for GBRAG flood projections. Note that sea level projections are not influenced by tides.

Year	MC-FRM sea-level rise RCP8.5, 99.5th percentile		2020 GBRAG RCP8.5, 99.5th percentile		GBRAG percentile of MC-FRM 99.5th percentile SLR (RCP8.5)
	ft, NAVD88	m, 2000 MSL	ft, NAVD88	m, 2000 MSL	
2030	1.2	0.43	1.24	0.44	99.4
2050	2.4	0.79	2.95	0.96	98.6
2070	4.2	1.34	5.34	1.69	98.5

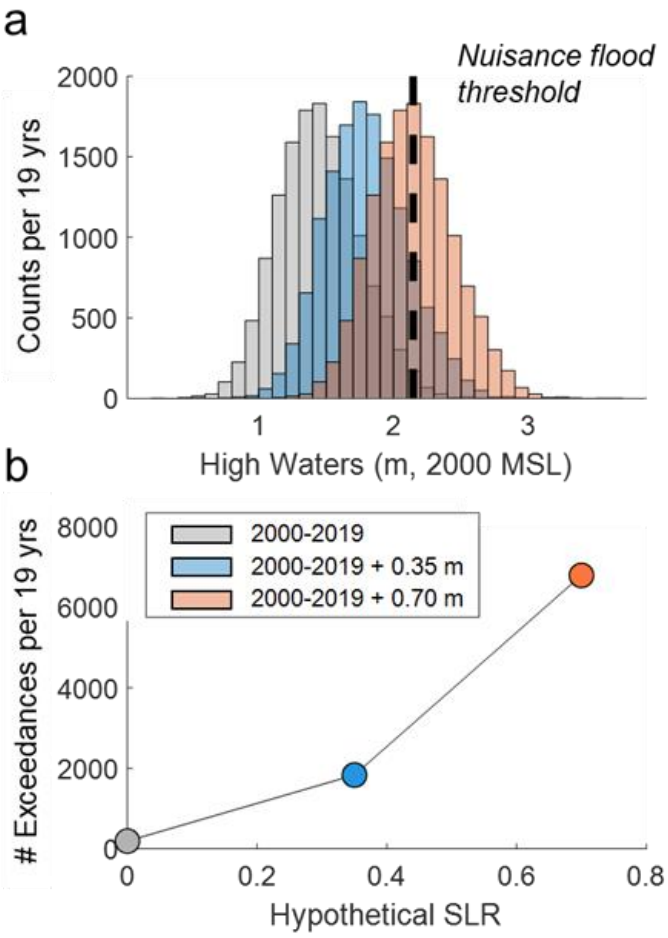

Figure C.1. Illustration of a nonlinear increase in flood hazard driven by relative sea level rise. (a) Binned counts of high-water elevations per 19 years relative to the Boston threshold for high tide flooding (2.15 m above 2000 MSL; (Sweet et al., 2018). 2001-2019 high waters are measured values from the Boston tide gauge (gray-shading). Blue and red shading show hypothetical future high-water elevations with 0.35 and 0.70 meters of sea level rise relative to 2001-2019 (similar to median RCP4.5 projections for 2050 and 2100). Sea level rise causes the high-water distributions to shift to the right, such that each 0.35-meter shift accelerates the number of high waters exceeding the nuisance flood threshold. This non-linear response is represented by an increasingly large area under the curve falling to the right of the flood threshold line. (b) Hypothetical sea level rise versus 19-yr total number of high waters exceeding the nuisance flood threshold (i.e. area under curve to the right of the flood threshold line in a). The steeper slope between the blue and red points illustrates the nonlinear increase in flood hazard driven by a constant rate of sea level rise.

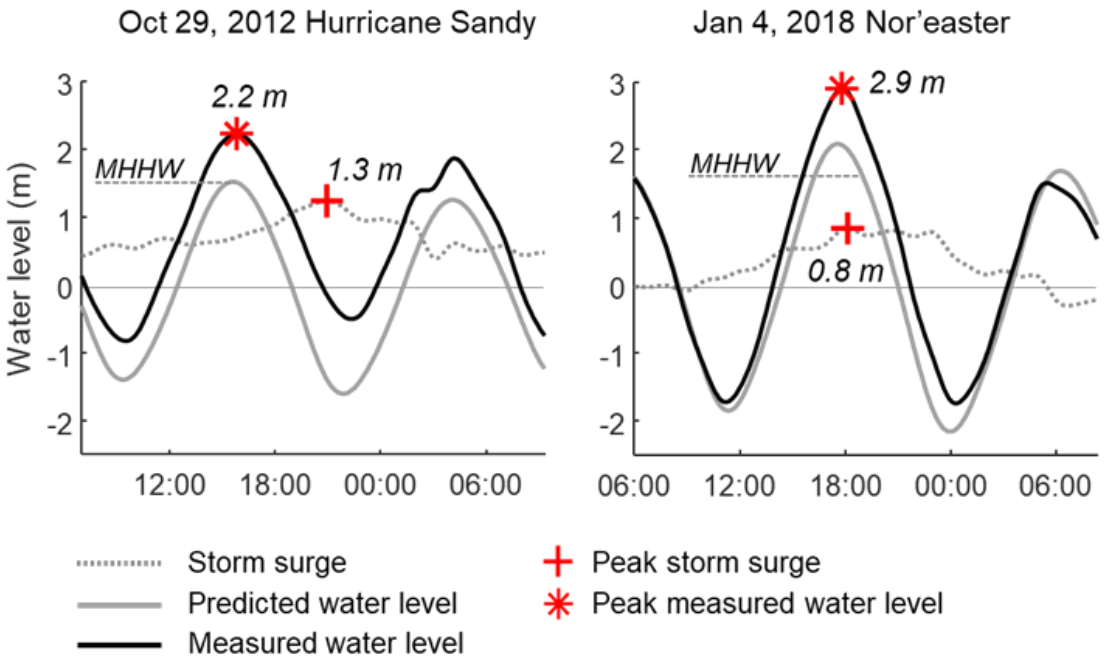

Figure C.2. Comparison of flooding during the record-breaking January 2018 Nor'easter and Hurricane Sandy in 2012. Measured water level relative to annual mean sea level (i.e. storm tide; black curve) is broken down into predicted water level (i.e. the tidal contribution; gray curve) and storm surge (calculated as observed water level minus the predicted tidal level; gray dashed curve). Annual mean higher high water (MHHW) is shown to compare high tide on the day of the storm to average high tide conditions. Water level measurements are from *tidesandcurrents.noaa.gov*.

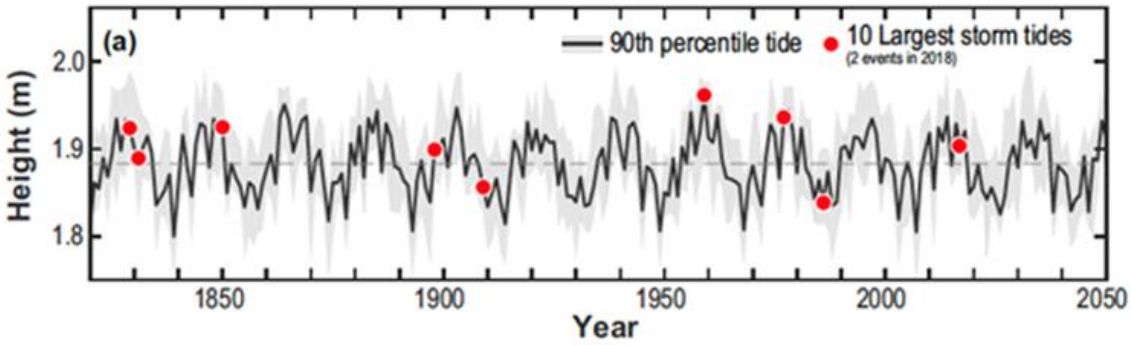

Figure C.3. Timing of Boston's top-ten storm tides relative to the 18.6-year tidal nodal cycle. The annual 90th percentile of high waters relative to annual MSL (black curve) are plotted as a function of time and clearly show the influence of the 18.6-year nodal cycle. Red circles mark the years of the ten largest historical Boston storm tides. Eight of the top ten events (including the two 2018 floods) occurred in years where the nodal cycle was in its positive phase (indicated by red circles falling above the horizontal dashed line; source (Talke et al., 2018)).

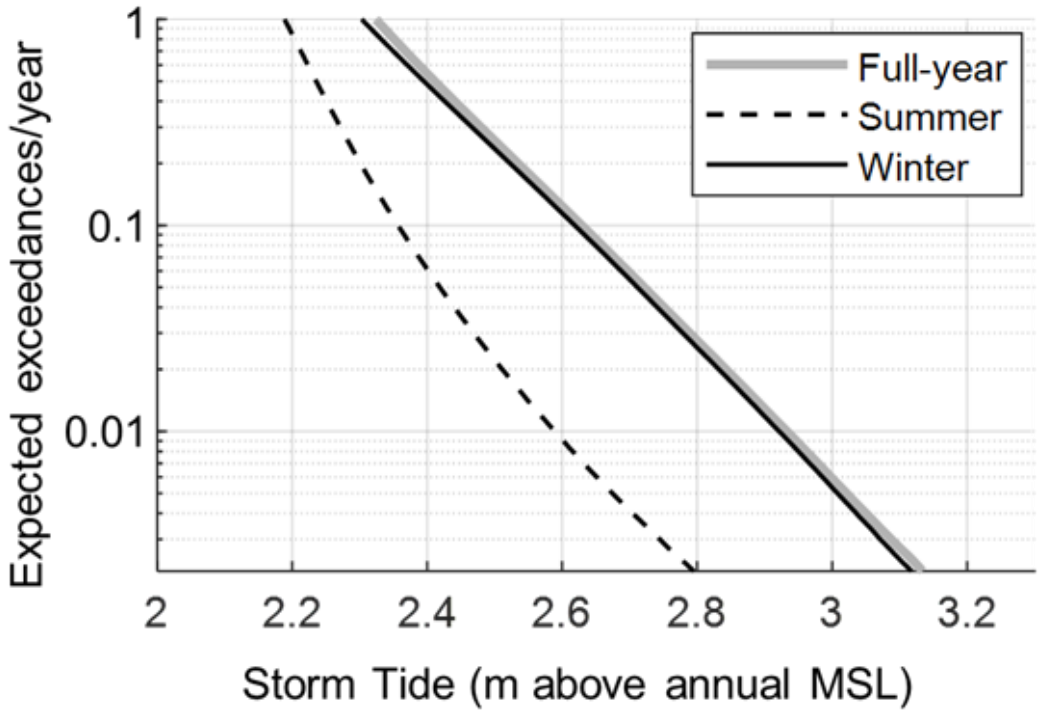

Figure C.4. Seasonal differences and winter dominance in Boston flood hazard. The summer season flood exceedance curve (dashed line) has a negligible contribution to the full-year curve (thick light-gray line), whereas the winter season curve (thin black line) nearly matches the full year. Flood exceedance distributions represent average flood hazard over the past 100 years relative to annual mean sea level and are calculated following Baranes et al. (2020).

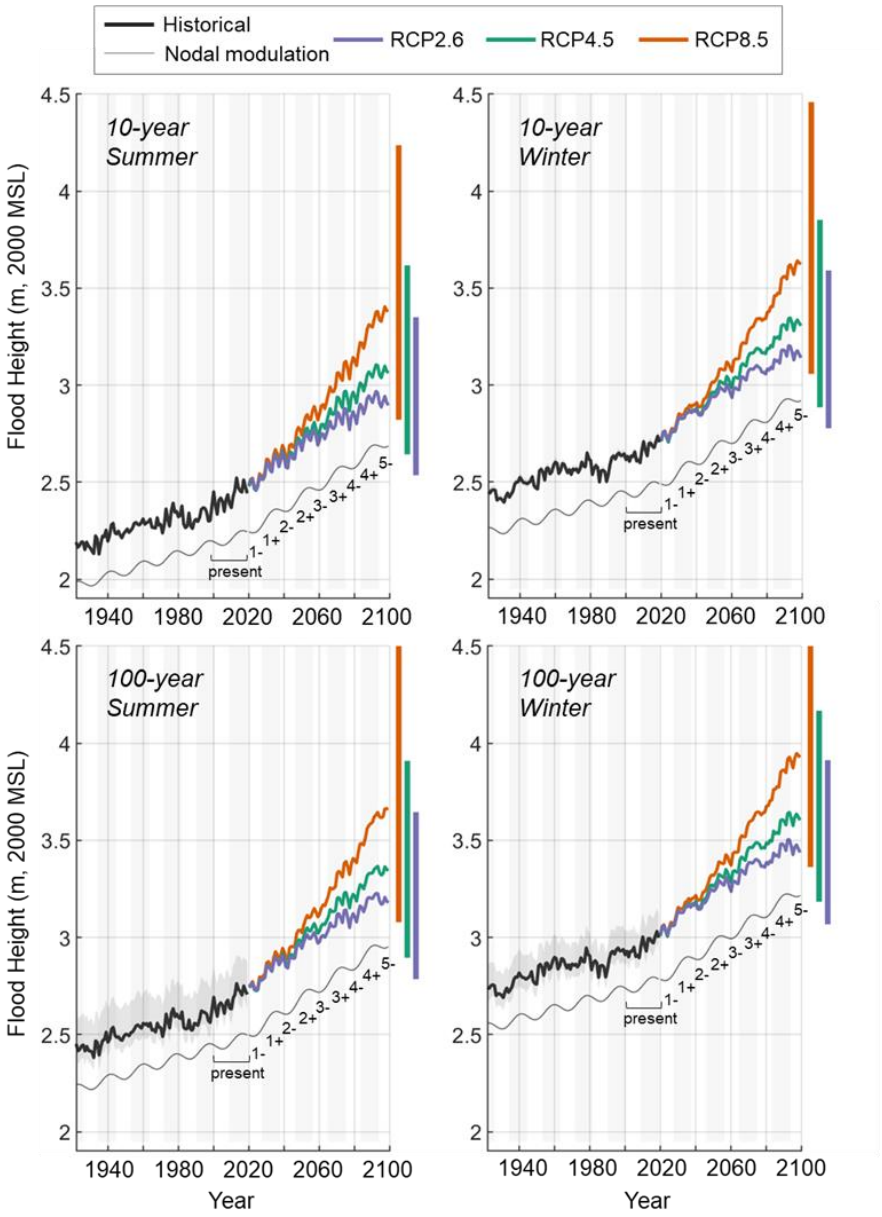

Figure C.5. Historical and projected 10-year (top panels) and 100-year (bottom panels) flood heights in meters above 2000 MSL for the summer (left-hand panels) and winter (right-hand panels) seasons. Purple, green, and orange lines show median projections for RCP2.6, RCP4.5, and RCP8.5 emissions concentration pathways, and bars on the right-hand-side show the central 90% ranges at 2100. These ranges include both statistical uncertainty in storm tides and uncertainty in sea level rise projections. Thick black lines show historical flood heights, and gray shading represents the central 90% range of statistical uncertainty (shading is not visible in the upper panels because there is less uncertainty in estimating the 10-year flood). The thin gray sinusoid is an illustration of 18.6-year nodal cycle amplitude and phase (note that positive-phase years are shaded in gray), offset from the flood height curves for visualization. Nodal cycle phase labels (present, 1-, 1+, etc.) correspond to Tables C.1 and C.2.

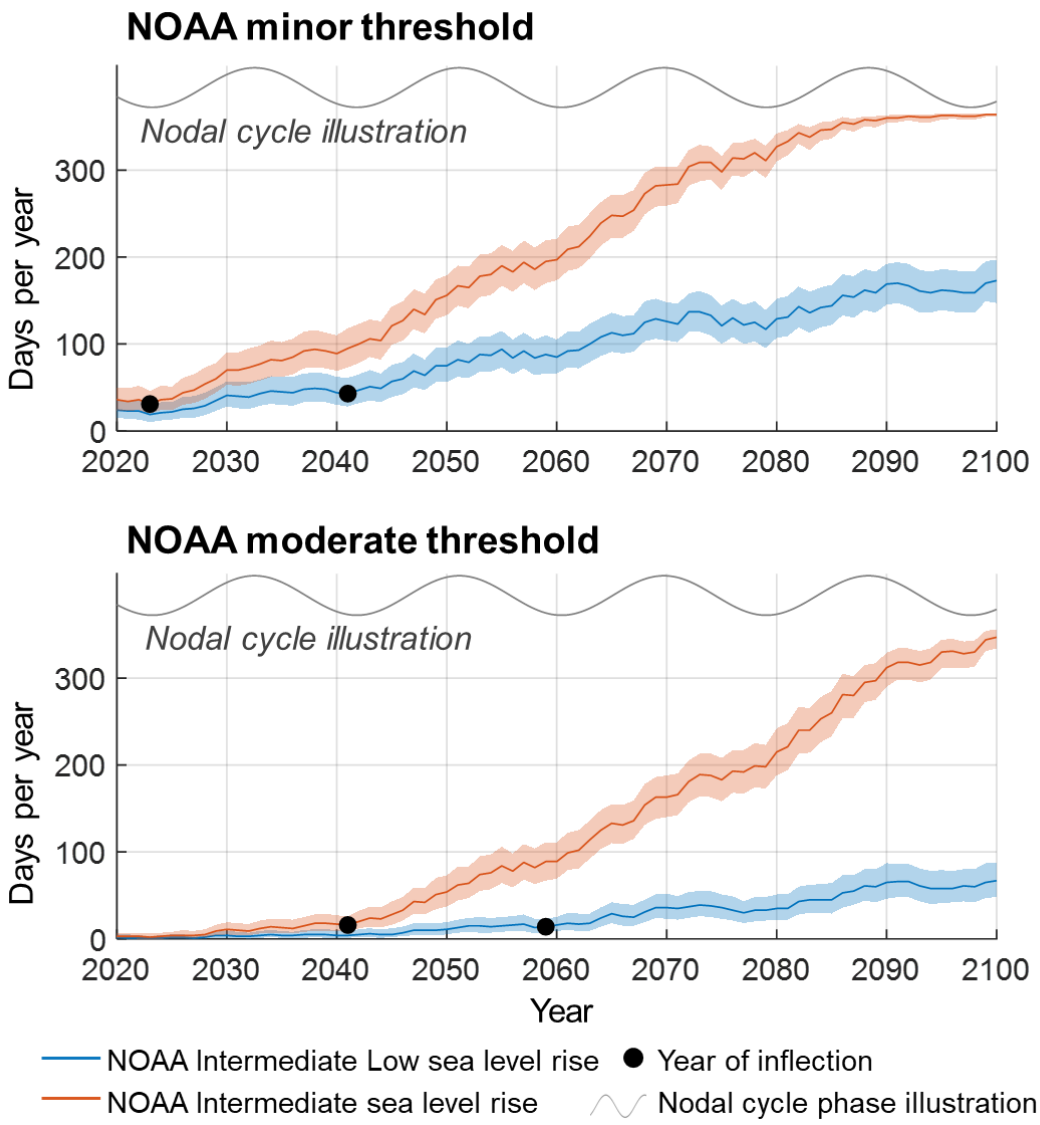

Figure C.6. Thompson et al. (2021) projections of high tide flooding days per year at the Boston NOAA tide gauge. Projections are shown for the NOAA minor flood threshold (63 cm above MHHW; top panel) and the NOAA moderate flood threshold (89 cm above MHHW; bottom panel) under two future sea level rise scenarios: NOAA Intermediate Low (blue) and NOAA Intermediate (red). The 50th percentile from the ensemble of projections (line) and 10th-90th percentile range (shaded regions) show the number of high tide flooding days increasing with time for both flood thresholds and both sea level rise scenarios. The 18.6-year nodal cycle (gray line) clearly modulates the increase in high tide flooding days, with the most rapid accelerations occurring over decades when the nodal cycle is increasing from its minimum to maximum amplitude. This is consistent with the year of inflection (black circle; see text for an explanation) occurring at a nodal cycle minimum for all projections scenarios. Data shown here are tabulated in Supplemental Dataset 2.

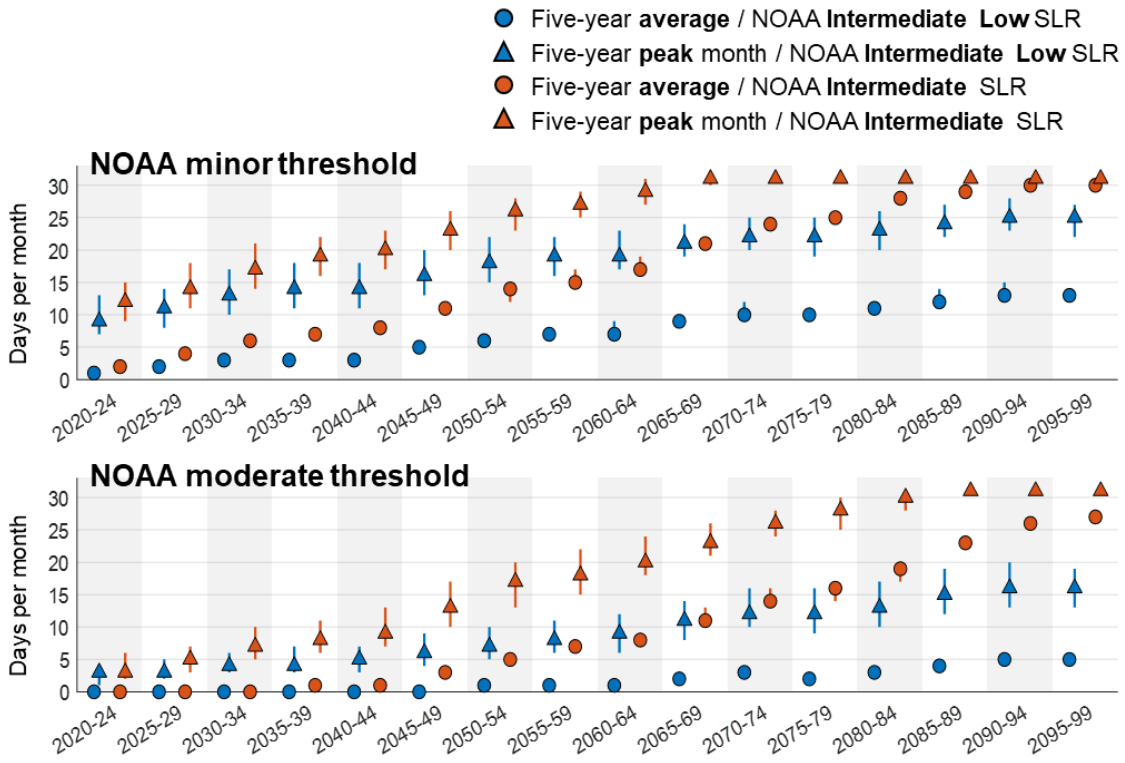

Figure C.7. Thompson et al. (2021) projections of high tide flooding days per month over 5-year periods at the Boston NOAA tide gauge for the NOAA minor (top panel) and moderate (bottom panel) flood thresholds and under the NOAA Intermediate Low (blue markers) and Intermediate (red markers) sea level rise scenarios. Over each 5-year period, circles show the average high tide flooding days per month, and triangles show the number of high tide flooding days in the peak flooding month within the 5 years. Markers represent the 50th percentile for each ensemble of projections, and lines are the 10th-90th percentile range. Data shown here are tabulated in Supplemental Dataset 3.

APPENDIX D

CHAPTER 3 SUPPORTING INFORMATION

Figure D.1. Field photographs showing (a) setup of marsh platform pressure transducers and water level loggers, and (b) netted centrifuge tube sediment traps deployed in low marsh in the North River estuary.

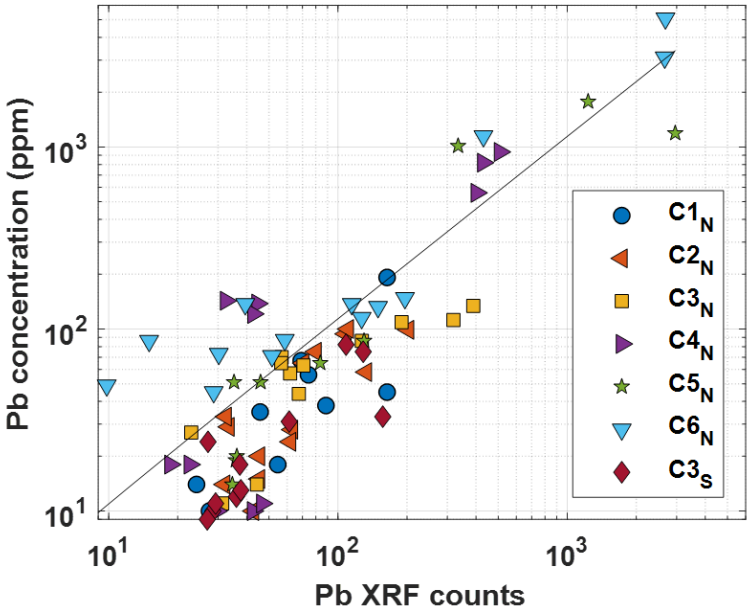

Figure D.2. Pb XRF counts to concentration calibration.

BIBLIOGRAPHY

Aida, I. (1981). Numerical experiments for the tsunamis generated off the coast of the Nankaido district. *Bulletin of the Earthquake Research Institute, 56,* 713-730.

Amante. C., & Eakins, B. W. (2011). ETOPO1 1 Arc-Minute Global Relief Model. *National Geographic Data Center, NOAA.* http://dx.doi.org/10.7289/V5C8276M.

An'naka, T., Inagaki, K., Tanaka, H., & Yanagisawa, K. (2003). Characteristics of great earthquakes along the Nankai trough based on numerical tsunami simulation. *Journal of Earthquake Engineering, 27,* article 307.

Ando, M. (1975). Source mechanisms and tectonic significance of historical earthquakes along the Nankai Trough, Japan. *Tectonophysics, 27(2),* 119-140. https://doi.org/10.1016/0040-1951(75)90102-X.

Argow, B. A., Hughes, Z. J., & FitzGerald, D. M. (2011). Ice raft formation, sediment load, and theoretical potential for ice-rafted sediment influx on northern coastal wetlands. *Continental Shelf Research, 31*(12), 1294–1305. https://doi.org/10.1016/j.csr.2011.05.004

Arcos, M. E. M., & LeVeque, R. J. (2015). Validating velocities in the GeoClaw tsunami model using observations near Hawaii from the 2011 Tohoku tsunami. *Pure and Applied Geophysics, 172(3-4),* 849-867. https://doi.org/10.1007/s00024-014-0980-y.

Arns, A., Wahl, T., Haigh, I. D., Jensen, J., & Pattiaratchi, C. (2013). Estimating extreme water level probabilities: A comparison of the direct methods and recommendations for best practise. *Coastal Engineering, 81,* 51–66. https://doi.org/10.1016/j.coastaleng.2013.07.003

Azuma, T., Ota, Y., Ishikawa, M., & Taniguchi, K. (2005). Late Quaternary coastal tectonics and development of marine terraces in Omaezaki, Pacific coast of central Japan. *Daiyonki-Kenkyu, 44(3),* 169-176. https://doi.org/10.4116/jaqua.44.169.

Baranes, H. E., Woodruff, J. D., Wallace, D. J., Kanamaru, K., & Cook, T. L. (2016). Sedimentological records of the C.E. 1707 Hoei Nankai Trough tsunami in the Bungo Channel, southwestern Japan. *Natural Hazards, 84(2),* 1185-1205. https://doi.org/10.1007/s11069-016-2498-3.

Baranes, H. E., Woodruff, J. D., Talke, S. A., Kopp, R. E., Ray, R. D., & DeConto, R. M. (2020). Tidally Driven Interannual Variation in Extreme Sea Level Frequencies in the Gulf of Maine. *Journal of Geophysical Research: Oceans, 125*(10), e2020JC016291. https://doi.org/10.1029/2020JC016291

Batstone, C., Lawless, M., Tawn, J., Horsburgh, K., Blackman, D., McMillan, A., Worth, D., Laeger, S., & Hunt, T. (2013). A UK best-practice approach for extreme sea-level analysis along complex topographic coastlines. *Ocean Engineering*, *71*, 28–39. https://doi.org/10.1016/j.oceaneng.2013.02.003

Berger, M. J., George, D. L., Leveque, R. J., & Mandli, K. T. (2011). The GeoClaw software for depth-averaged flows with adaptive refinement. *Advances in Water Resources, 34(9),* 1195-1206. https://doi.org/10.1016/j.advwatres.2011.02.016.

Bertin, X., de Bakker, A., van Dongeren, A., Coco, G., André, G., Ardhuin, F., Bonneton, P., Bouchette, F., Castelle, B., Crawford, W. C., Davidson, M., Deen, M., Dodet, G., Guérin, T., Inch, K., Leckler, F., McCall, R., Muller, H., Olabarrieta, M., … Tissier, M. (2018). Infragravity waves: From driving mechanisms to impacts. *Earth-Science Reviews*, *177*, 774–799. https://doi.org/10.1016/j.earscirev.2018.01.002

Boesch, D. F., & Turner, R. E. (1984). Dependence of fishery species on salt marshes: The role of food and refuge. *Estuaries*, *7*(4), 460–468. https://doi.org/10.2307/1351627

Boldt, K. V., Lane, P., Woodruff, J. D., & Donnelly, J. P. (2010). Calibrating a sedimentary record of overwash from Southeastern New England using modeled historic hurricane surges. *Marine Geology*, *275*(1), 127–139. https://doi.org/10.1016/j.margeo.2010.05.002

Bosma, K., Douglas, E., Kirshen, P., McArthur, K., Miller, S., & Watson, C. (2015). *MassDOT-FHWA Pilot Project Report: Climate Change and Extreme Weather Vulnerability Assessments and Adaptation Options for the Central* (p. 172). https://www.massdot.state.ma.us/Portals/8/docs/environmental/SustainabilityEMS/Pilot_Project_Report_MassDOT_FHWA.pdf

Braswell, A. E., Heffernan, J. B., & Kirwan, M. L. (2020). How Old Are Marshes on the East Coast, USA? Complex Patterns in Wetland Age Within and Among Regions. *Geophysical Research Letters*, *47*(19), e2020GL089415. https://doi.org/10.1029/2020GL089415

Bricker-Urso, S., Nixon, S. W., Cochran, J. K., Hirschberg, D. J., & Hunt, C. (1989). Accretion rates and sediment accumulation in Rhode Island salt marshes. *Estuaries*, *12*(4), 300–317. https://doi.org/10.2307/1351908

Buchanan, M. K., Kopp, R. E., Oppenheimer, M., & Tebaldi, C. (2016). Allowances for evolving coastal flood risk under uncertain local sea-level rise. *Climatic Change*, *137*(3), 347–362. https://doi.org/10.1007/s10584-016-1664-7

Buchanan, M. K., Oppenheimer, M., & Kopp, R. E. (2017). Amplification of flood frequencies with local sea level rise and emerging flood regimes. *Environmental Research Letters*, *12*(6), 064009. https://doi.org/10.1088/1748-9326/aa6cb3

Cahoon, D. R. (2006). A review of major storm impacts on coastal wetland elevations. *Estuaries and Coasts*, *29*(6), 889–898. https://doi.org/10.1007/BF02798648

Caldwell, P. C., US DOC/NOAA/NESDIS > National Centers For Environmental Information, Merrifield, M. A., & Thompson, P. R. (2010). *Sea level measured by tide gauges from global oceans as part of the Joint Archive for Sea Level (JASL) since 1846* [Data set]. National Oceanographic Data Center, NOAA. https://doi.org/10.7289/V5V40S7W

Castagno, K. A., Donnelly, J. P., & Woodruff, J. D. (2020). Grain-Size Analysis of Hurricane-Induced Event Beds in a New England Salt Marsh, Massachusetts, USA. *Joural of Coastal Research, in press*.

Catalano, A. J., & Broccoli, A. J. (2018). Synoptic Characteristics of Surge-Producing Extratropical Cyclones along the Northeast Coast of the United States. *Journal of Applied Meteorology and Climatology*, *57*(1), 171–184. https://doi.org/10.1175/JAMC-D-17-0123.1

Central Disaster Management Council. (2012). Final report - toward the reconstruction for sound and unwavering Japan. http://www.bousai.go.jp/kaigirep/chuobou/suishinkaigi/english/pdf/FinalReport.pdf#page=1.

Chen, J., Zhu, W., Tian, Y. Q., & Yu, Q. (2020). Monitoring dissolved organic carbon by combining Landsat-8 and Sentinel-2 satellites: Case study in Saginaw River estuary, Lake Huron. *Science of The Total Environment*, *718*, 137374. https://doi.org/10.1016/j.scitotenv.2020.137374

Cheung, K. F., Tang, L., Donnelly, J. P., Scileppi, E. M., Liu, K.-B., Mao, X.-Z., Houston, S. H., & Murnane, R. J. (2007). Numerical modeling and field evidence of coastal overwash in southern New England from Hurricane Bob and implications for paleotempestology. *Journal of Geophysical Research: Earth Surface*, *112*(F3). https://doi.org/10.1029/2006JF000612

Chmura, G. L., Anisfeld, S. C., Cahoon, D. R., & Lynch, J. C. (2003). Global carbon sequestration in tidal, saline wetland soils. *Global Biogeochemical Cycles*, *17*(4). https://doi.org/10.1029/2002GB001917

Church, J. A., Clark, P. U., Cazenave, A., Gregory, J. M., Jevrejeva, S., Levermann, A., Merrifield, M. A., Milne, G. A., Nerem, R. S., Nunn, P. D., Payne, A. J., Pfeffer, W. T., Stammer, D., & Unnikrishnan, A. S. (2013). Sea level change. In T. F. Stocker, D. Qin, G. K. Plattner, M. Tignor, S. K. Allen, J. Boschung, A. Nauels, Y. Xia, V. Bex, & P. M. Midgley (Eds.), *Climate Change 2013: The Physical Science Basis. Contribution of Working Group I to the Fifth Assessment Report of the Intergovernmental Panel on Climate Change*. Cambridge University Press. http://drs.nio.org/drs/handle/2264/4605

Clawpack Development Team. (2015). Clawpack Version 5.3.0, http://www.clawpack.org.

Coleman, D. J., Ganju, N. K., & Kirwan, M. L. (2020). Sediment Delivery to a Tidal Marsh Platform Is Minimized by Source Decoupling and Flux Convergence. *Journal of Geophysical Research: Earth Surface*, *125*(8), e2020JF005558. https://doi.org/10.1029/2020JF005558

Coles, S. (2001). *An Introduction to Statistical Modeling of Extreme Values*. Springer.

Croudace, I. W., Rindby, A., & Rothwell, R. G. (2006). ITRAX: Description and evaluation of a new multi-function X-ray core scanner. *Geological Society, London, Special Publications*, *267*(1), 51–63. https://doi.org/10.1144/GSL.SP.2006.267.01.04

Dean, W. E. (1974). Determination of carbonate and organic matter in calcareous sediments and sedimentary rocks by loss on ignition; comparison with other methods. *Journal of Sedimentary Research*, *44*(1), 242–248. https://doi.org/10.1306/74D729D2-2B21-11D7-8648000102C1865D

Deegan, L. A., Johnson, D. S., Warren, R. S., Peterson, B. J., Fleeger, J. W., Fagherazzi, S., & Wollheim, W. M. (2012). Coastal eutrophication as a driver of salt marsh loss. *Nature*, *490*(7420), 388–392. https://doi.org/10.1038/nature11533

Discenza, D., Keimowitz, A., & Fitzgerald, N. (2014). Calibration and Evaluation of an X-Ray Fluorescence Method for the Determination of Lead and Arsenic in Soils. *J. Environ. Anal. Chem.*, *1*, 103. https://doi.org/10.4172/JEAC1000103

Dodet, G., Melet, A., Ardhuin, F., Bertin, X., Idier, D., & Almar, R. (2019). The Contribution of Wind-Generated Waves to Coastal Sea-Level Changes. *Surveys in Geophysics*, *40*(6), 1563–1601. https://doi.org/10.1007/s10712-019-09557-5

Donatelli, C., Ganju, N. K., Zhang, X., Fagherazzi, S., & Leonardi, N. (2018). Salt Marsh Loss Affects Tides and the Sediment Budget in Shallow Bays. *Journal of Geophysical Research: Earth Surface*, *123*(10), 2647–2662. https://doi.org/10.1029/2018JF004617

Douglas, E., Kirshen, P., DeConto, R. M., FitzGerald, D. M., Hay, C., Hughes, Z., Kemp, A. C., Kopp, R. E., Anderson, B., Kuang, Z., Ravela, S., Woodruff, J. D., Barlow, M., Collins, M., DeGaetano, A., Schlosser, C. A., Ganguly, A., Kodra, E., & Ruth, M. (2016). *Climate change and sea level rise projections for Boston: The Boston Research Advisory Group report.* (p. 54). Climate Ready Boston. https://www.boston.gov/sites/default/files/document-file-12-2016/brag_report_-_final.pdf

Eliot, M. (2010). Influence of interannual tidal modulation on coastal flooding along the Western Australian coast. *Journal of Geophysical Research: Oceans*, *115*(C11). https://doi.org/10.1029/2010JC006306

Emanuel, K. A. (2013). Downscaling CMIP5 climate models shows increased tropical cyclone activity over the 21st century. *Proceedings of the National Academy of Sciences*, *110*(30), 12219–12224. https://doi.org/10.1073/pnas.1301293110

Fagherazzi, S., Kearney, W. S., Jiménez-Robles, A. M., Hopkinson, C., Castagno, K. A., & Ganju, N. K. (2018). *Assessing salt marsh resilience with sediment fluxes: The critical role of marine sediment inputs*. *2018*.

Fagherazzi, S., Kirwan, M. L., Mudd, S. M., Guntenspergen, G. R., Temmerman, S., D'Alpaos, A., Koppel, J. van de, Rybczyk, J. M., Reyes, E., Craft, C., & Clough, J. (2012). Numerical models of salt marsh evolution: Ecological, geomorphic, and climatic factors. *Reviews of Geophysics*, *50*(1). https://doi.org/10.1029/2011RG000359

Fagherazzi, S., & Priestas, A. M. (2010). Sediments and water fluxes in a muddy coastline: Interplay between waves and tidal channel hydrodynamics. *Earth Surface Processes and Landforms*, *35*(3), 284–293. https://doi.org/10.1002/esp.1909

Fagherazzi, S., Wiberg, P. L., Temmerman, S., Struyf, E., Zhao, Y., & Raymond, P. A. (2013). Fluxes of water, sediments, and biogeochemical compounds in salt marshes. *Ecological Processes*, *2*(1), 3. https://doi.org/10.1186/2192-1709-2-3

Familkhalili, R., Talke, S. A., & Jay, D. A. (2020). Tide-Storm Surge Interactions in Highly Altered Estuaries: How Channel Deepening Increases Surge Vulnerability. *Journal of Geophysical Research: Oceans*, *125*(4), e2019JC015286. https://doi.org/10.1029/2019JC015286

Feigl, K. L., Agnew, D. C., Bock, Y., Dong, D., Donnellan, A., Hager, B. H., et al. (1993). Space geodetic measurement of crustal deformation in central and southern California. *Journal of Geophysical Research, 98(B12)*, 21677-21712. https://doi.org/10.1029/93JB02405.

Ferro, C. A. T., & Segers, J. (2003). Inference for clusters of extreme values. *Journal of the Royal Statistical Society: Series B (Statistical Methodology)*, *65*(2), 545–556. https://doi.org/10.1111/1467-9868.00401

FitzGerald, D. M. (1993). Origin and Stability of Tidal Inlets in Massachusetts. In *Formation and Evolution of Multiple Tidal Inlets* (pp. 1–61). American Geophysical Union (AGU). https://doi.org/10.1029/CE044p0001

Fitzgerald, D. M., & Heteren, S. V. (1999). Classification of paraglacial barrier systems: Coastal New England, USA. *Sedimentology*, *46*(6), 1083–1108. https://doi.org/10.1046/j.1365-3091.1999.00266.x

FitzGerald, D. M., Hughes, Z. J., Georgiou, I. Y., Black, S., & Novak, A. (2020). Enhanced, Climate-Driven Sedimentation on Salt Marshes. *Geophysical Research Letters*, *47*(10), e2019GL086737. https://doi.org/10.1029/2019GL086737

FitzGerald, D., Ryerson, O., Hughes, Z., Black, S., Georgiou, I., Hein, C., & Novak, A. (2020). Long-term Variability in Inorganic Sediment Contributions to the Great Marsh, Massachusetts. *Journal of Coastal Research*, *95*(SI), 490–494. https://doi.org/10.2112/SI95-095.1

Fontenault, J., Vinhateiro, N., & Knee, K. (2013). *Mapping and Analysis of Privately-Owned Coastal Structures along the Massachusetts Shoreline* (p. 76). RPS ASA. https://www.mass.gov/files/documents/2016/08/nk/private-coastal-structures-2013.pdf

Foster, D. R., & Motzkin, G. (2003). Interpreting and conserving the openland habitats of coastal New England: Insights from landscape history. *Forest Ecology and Management*, *185*(1), 127–150. https://doi.org/10.1016/S0378-1127(03)00251-2

Freitas, F., & Ball, D. (1995). *Warnings ignored! The story of the Portland Gale of 1898*.

Fujiwara, O., Fujino, S., Komatsubara, J., Morita, Y., & Namegaya, Y. (2016). Paleoecological evidence for coastal subsidence during five great earthquakes in the past 1500 years along the northern onshore continuation of the Nankai subduction zone. *Quaternary International, 397,* 523-540. https://doi.org/10.1016/j.quaint.2015.11.014.

Fujiwara, O., Hirakawa, K., Irizuki, T., Hasegawa, S., Hase, Y., Uchida, J., & Abe, K. (2010). Millennium-scale recurrent uplift from beach deposits bordering the eastern Nankai Trough, Omaezaki area, central Japan. *Island Arc, 19(3),* 374-388. https://doi.org/10.1111/j.1440-1738.2010.00729.x.

Fujiwara, O., Ono, E., Satake, K., Sawai, Y., Umitsu, M., Yata, T., et al. (2007a). Trace of the AD1707 Hoei earthquake from the coastal lowland, Shizuoka Prefecture, central Japan. *Annual Report on Active Fault and Paleoearthquake Researches, 7,* 157-171.

Fujiwara, O., Sawai, Y., Morita, Y., Komatsubara, J., & Abe, K. (2007b). Coseismic subsidence recorded in the Holocene sequence in the Ukishima-ga-hara lowland, Shizuoka Prefecture, central Japan. *Annual Report on Active Fault and Paleoearthquake Researches, 7,* 91-118.

Furumura, T., Imai, K., & Maeda, T. (2011). A revised tsunami source model for the 1707 Hoei earthquake and simulation of tsunami inundation of Ryujin Lake, Kyushu, Japan. *Journal of Geophysical Research, 116,* B02308. https://doi.org/10.1029/2010JB007918.

Furuse, N., & Kono, Y. (2003). Slab residual gravity anomaly: gravity reduction due to subducting plates beneath the Japanese Islands. *Journal of Geodynamics, 36(4),* 497-514. https://doi.org/10.1016/S0264-3707(03)00062-0.

Galloway, G. E., Baecher, G. B., Plasencia, D., Coulton, K. G., Louthain, J., Bagha, M., & Levy, A. R. (2006). *Assessing the Adequacy of the National Flood Insurance Program's 1 Percent Flood Standard* (p. 197) [2001-2006 Evalulation of the National Flood Insurance Program]. http://s3-us-gov-west-1.amazonaws.com/dam-production/uploads/20130726-1602-20490-6095/nfip_eval_1_percent_standard.pdf

Ganju, N. K. (2019). Marshes Are the New Beaches: Integrating Sediment Transport into Restoration Planning. *Estuaries and Coasts*, *42*(4), 917–926. https://doi.org/10.1007/s12237-019-00531-3

Ganju, N. K., Defne, Z., Kirwan, M. L., Fagherazzi, S., D'Alpaos, A., & Carniello, L. (2017). Spatially integrative metrics reveal hidden vulnerability of microtidal salt marshes. *Nature Communications*, *8*(1), 14156. https://doi.org/10.1038/ncomms14156

Ganju, N. K., Nidzieko, N. J., & Kirwan, M. L. (2013). Inferring tidal wetland stability from channel sediment fluxes: Observations and a conceptual model. *Journal of Geophysical Research: Earth Surface*, *118*(4), 2045–2058. https://doi.org/10.1002/jgrf.20143

Garner, A. J., Mann, M. E., Emanuel, K. A., Kopp, R. E., Lin, N., Alley, R. B., Horton, B. J., DeConto, R. M., Donnelly, J. P., & Pollard, D. (2017). Impact of climate change on New York City's coastal flood hazard: Increasing flood heights from the preindustrial to 2300 CE. *Proceedings of the National Academy of Sciences*, *114*(45), 11861–11866. https://doi.org/10.1073/pnas.1703568114

Garrett, C. (1972). Tidal Resonance in the Bay of Fundy and Gulf of Maine. *Nature*, *238*(5365), 441–443. https://doi.org/10.1038/238441a0

Garrett, E., Fujiwara, O., Garrett, P., Heyvaert, V. M. A., Shishikura, M., & Yokoyama, Y. (2016). A systematic review of geological evidence for Holocene earthquakes and tsunamis along the Nankai-Suruga Trough, Japan. *Earth-Science Reviews*, *159*, 337-357. https://doi.org/10.1016/j.earscirev.2016.06.011.

Geodetic Observation Center, Geospatial Information Authority of Japan. (2015). GEONET. http://terras.gsi.go.jp.

Geographical Survey Institute of Japan. (1952). Resurvey of the southwestern part of Japan after the great Nankaido earthquake of 1946. *Bulletin of the Geographical Survey Institute, 3(Part 1),* 31-118.

Ghanbari, M., Arabi, M., & Obeysekera, J. (2020). Chronic and Acute Coastal Flood Risks to Assets and Communities in Southeast Florida. *Journal of Water Resources Planning and Management*, *146*(7), 04020049. https://doi.org/10.1061/(ASCE)WR.1943-5452.0001245

Goddard, P. B., Yin, J., Griffies, S. M., & Zhang, S. (2015). An extreme event of sea-level rise along the Northeast coast of North America in 2009–2010. *Nature Communications*, *6*(1), 1–9. https://doi.org/10.1038/ncomms7346

Godin, G. (1992). Possibility of rapid changes in the tide of the Bay of Fundy, based on a scrutiny of the records from Saint John. *Continental Shelf Research*, *12*(2), 327–338. https://doi.org/10.1016/0278-4343(92)90034-H

Godin, G. (1993). On tidal resonance. *Continental Shelf Research*, *13*(1), 89–107. https://doi.org/10.1016/0278-4343(93)90037-X

Godin, G. (1995). Rapid evolution of the tide in the Bay of Fundy. *Continental Shelf Research*, *15*(2–3), 369–372. https://doi.org/10.1016/0278-4343(93)E0005-S

González, F., LeVeque, R. J., Varkovitsky, J., Chamberlain, P., Hirai, B., & George, D. L. (2011). GeoClaw Results for the NTHMP Tsunami Benchmark Problems, http://www.clawpack.org/links/nthmp-benchmarks/geoclaw-results.

Greenberg, D. A., Blanchard, W., Smith, B., & Barrow, E. (2012). Climate Change, Mean Sea Level and High Tides in the Bay of Fundy. *Atmosphere-Ocean*, *50*(3), 261–276. https://doi.org/10.1080/07055900.2012.668670

Griggs, G., Arvai, J., Cayan, D., DeConto, R. M., Fox, J., Fricker, H. A., Kopp, R. E., Tebaldi, C., & Whiteman, E. A. (2017). *Rising seas in California: An update on sea-level rise science.* (p. 71) [California Ocean Science Trust Tech. Rep.]. http://climate.calcommons.org/bib/rising-seas-california-update-sea-level-rise-science

Hager, B. H., King, R. W., & Murray, M. H. (1991). Measurement of crustal deformation using the global positioning system. *Annual Review of Earth and Planetary Sciences*, *19*, 351-382. https://doi.org/10.1146/annurev.ea.19.050191.002031.

Haigh, I. D., Eliot, M., & Pattiaratchi, C. (2011). Global influences of the 18.61 year nodal cycle and 8.85 year cycle of lunar perigee on high tidal levels. *Journal of Geophysical Research: Oceans*, *116*(C6). https://doi.org/10.1029/2010JC006645

Haigh, I. D., Nicholls, R., & Wells, N. (2010). A comparison of the main methods for estimating probabilities of extreme still water levels. *Coastal Engineering*, *57*(9), 838–849. https://doi.org/10.1016/j.coastaleng.2010.04.002

Haigh, I. D., Pickering, M. D., Green, J. A. M., Arbic, B. K., Arns, A., Dangendorf, S., Hill, D. F., Horsburgh, K., Howard, T., Idier, D., Jay, D. A., Jänicke, L., Lee, S. B., Müller, M., Schindelegger, M., Talke, S. A., Wilmes, S.-B., & Woodworth, P. L. (2020). The Tides They Are A-Changin': A Comprehensive Review of Past and Future Nonastronomical Changes in Tides, Their Driving Mechanisms, and Future Implications. *Reviews of Geophysics*, *58*(1), e2018RG000636. https://doi.org/10.1029/2018RG000636

Hallegatte, S., Green, C., Nicholls, R. J., & Corfee-Morlot, J. (2013). Future flood losses in major coastal cities. *Nature Climate Change*, *3*(9), 802–806. https://doi.org/10.1038/nclimate1979

Harris, D. L., & Bureau, U. S. W. (1963). *Characteristics of the Hurricane Storm Surge*. Department of Commerce, Weather Bureau.

Hatori, T. (1974). Sources of large tsunamis in southwest Japan. *Journal of the Seismological Society of Japan, 27,* 10-24.

Hatori, T. (1985), Field investigation of historical tsunamis along the east coast of Kyushu, West Japan. *Bulletin of the Earthquake Research Institute, University of Tokyo, 60,* 439-459.

Headquarters for Earthquake Research Promotion/ (2013). Long-term evaluation of Nankai Trough Earthquakes (revised version). http://www.jishin.go.jp/main/chousa/kaikou_pdf/nankai_2.pdf.

Hok, S., Fukuyama, E., & Hashimoto, C. (2011). Dynamic rupture scenarios of anticipated Nankai-Tonankai earthquakes, southwest Japan. *Journal of Geophysical Research, 116(B12),* B12319. https://doi.org/10.1029/2011JB008492.

Hopkinson, C. S., Morris, J. T., Fagherazzi, S., Wollheim, W. M., & Raymond, P. A. (2018). Lateral Marsh Edge Erosion as a Source of Sediments for Vertical Marsh Accretion. *Journal of Geophysical Research: Biogeosciences*, *123*(8), 2444–2465. https://doi.org/10.1029/2017JG004358

Horsburgh, K. J., Williams, J. A., Flowerdew, J., & Mylne, K. (2008). Aspects of operational forecast model skill during an extreme storm surge event. *Journal of Flood Risk Management*, *1*(4), 213–221. https://doi.org/10.1111/j.1753-318X.2008.00020.x

Hughes, R. G. (2004). Climate change and loss of saltmarshes: Consequences for birds. *Ibis*, *146*(s1), 21–28. https://doi.org/10.1111/j.1474-919X.2004.00324.x

Hunter, J. (2010). Estimating sea-level extremes under conditions of uncertain sea-level rise. *Climatic Change*, *99*(3), 331–350. https://doi.org/10.1007/s10584-009-9671-6

Hyodo, M., & Hori, T. (2013). Re-examination of possible great interplate earthquake scenarios in the Nankai Trough, southwest Japan, based on recent findings and numerical simulations. *Tectonophysics*, *600,* 175-186. https://doi.org/10.1016/j.tecto.2013.02.038.

Hyodo, M., Hori, T., Ando, K., & Baba, T. (2014). The possibility of deeper or shallower extent of the source area of Nankai Trough earthquakes based on the 1707 Hoei tsunami heights along the Pacific and Seto Inland Sea coasts, southwest Japan. *Earth, Planets and Space, 66(1),* 123. https://doi.org/10.1186/1880-5981-66-123.

Ide, S., Baltay, A., & Beroza, G.C. (2011). Shallow Dynamic Overshoot and Energetic Deep Rupture in the 2011 Mw 9.0 Tohoku-Oki Earthquake, *Science*, *332*(*6036*), 1426–1429. https://doi.org/10.1126/science.1207020.

Iryu, Y., Maemoku, H., Yamada, T., & Maeda, Y. (2009). Limestones as a paleobathymeter for reconstructing past seismic activities: Muroto-misaki, Shikoku, southwestern Japan. *Global and Planetary Change, 66,* 52-64. https://doi.org/10.1016/j.gloplacha.2008.03.009.

Ishibashi, K. (1999). Great Tokai and Nankai, Japan, earthquakes as revealed by historical seismology: 1. Review of the events until the mid-14th century. *Chigaku Zasshi, 108(4),* 399-423. https://doi.org/10.5026/jgeography.108.4_399.

Ishibashi, K. (2004). Status of historical seismology in Japan. *Annals of Geophysics, 47(2-3),* 339-368.

Johnson, D. W. (1925). *The New England-Acadian Shoreline*. John Wiley & Sons.

Kaneko, Y., Avouac, J., & Lapusta, N. (2010). Towards inferring earthquake patterns from geodetic observations of interseismic coupling. *Nature Geoscience, 3,* 363-369. https://doi.org/10.1038/ngeo843.

Kendall, M. G. (1938). A New Measure of Rank Correlation. *Biometrika*, *30*(1/2), 81–93. JSTOR. https://doi.org/10.2307/2332226

Kirshen, P., Knee, K., & Ruth, M. (2008). Climate change and coastal flooding in Metro Boston: Impacts and adaptation strategies. *Climatic Change*, *90*(4), 453–473. https://doi.org/10.1007/s10584-008-9398-9

Kirwan, M. L., Guntenspergen, G. R., D'Alpaos, A., Morris, J. T., Mudd, S. M., & Temmerman, S. (2010). Limits on the adaptability of coastal marshes to rising sea level. *Geophysical Research Letters*, *37*(23). https://doi.org/10.1029/2010GL045489

Kirwan, M. L., & Megonigal, J. P. (2013). Tidal wetland stability in the face of human impacts and sea-level rise. *Nature*, *504*(7478), 53–60. https://doi.org/10.1038/nature12856

Kirwan, M. L., Murray, A. B., Donnelly, J. P., & Corbett, D. R. (2011). Rapid wetland expansion during European settlement and its implication for marsh survival under modern sediment delivery rates. *Geology*, *39*(5), 507–510. https://doi.org/10.1130/G31789.1

Knutson, T. R., McBride, J. L., Chan, J., Emanuel, K., Holland, G., Landsea, C., Held, I., Kossin, J. P., Srivastava, A. K., & Sugi, M. (2010). Tropical cyclones and climate change. *Nature Geoscience*, *3*(3), 157–163. https://doi.org/10.1038/ngeo779

Kodaira, S., Hori, T., Ito, A., Miura, S., Fujie, G., Park, J., et al. (2006). A cause of rupture segmentation and synchronization in the Nankai Trough revealed by seismic imaging and numerical simulation. *Journal of Geophysical Research, 111(B9)*, B09301-17. https://doi.org/10.1029.2005JB004030.

Kopp, R. E., Horton, R. M., Little, C. M., Mitrovica, J. X., Oppenheimer, M., Rasmussen, D. J., Strauss, B. H., & Tebaldi, C. (2014). Probabilistic 21st and 22nd century sea-level projections at a global network of tide-gauge sites. *Earth's Future*, *2*(8), 383–406. https://doi.org/10.1002/2014EF000239

Kranenburg, W. M., Geyer, W. R., Garcia, A. M. P., & Ralston, D. K. (2019). Reversed Lateral Circulation in a Sharp Estuarine Bend with Weak Stratification. *Journal of Physical Oceanography*, *49*(6), 1619–1637. https://doi.org/10.1175/JPO-D-18-0175.1

Ku, L.-F., Greenberg, D. A., Garrett, C. J. R., & Dobson, F. W. (1985). Nodal Modulation of the Lunar Semidiurnal Tide in the Bay of Fundy and Gulf of Maine. *Science*, *230*(4721), 69–71. https://doi.org/10.1126/science.230.4721.69

Lambert, E., Rohmer, J., Cozannet, G. L., & Wal, R. S. W. van de. (2020). Adaptation time to magnified flood hazards underestimated when derived from tide gauge records. *Environmental Research Letters*. https://doi.org/10.1088/1748-9326/ab8336

Leadbetter, M. R. (1983). Extremes and local dependence in stationary sequences. *Zeitschrift Für Wahrscheinlichkeitstheorie Und Verwandte Gebiete*, *65*(2), 291–306. https://doi.org/10.1007/BF00532484

Leffler, K., & Jay, D. A. (2009). Enhancing tidal harmonic analysis: Robust (hybrid L1/L2) solutions. *Continental Shelf Research*, *29*(1), 78–88. https://doi.org/10.1016/j.csr.2008.04.011

Leonard, L. A. (1997). Controls of sediment transport and deposition in an incised mainland marsh basin, southeastern North Carolina. *Wetlands*, *17*(2), 263–274. https://doi.org/10.1007/BF03161414

LeVeque, R. J., & George, D. L. (2008). High-resolution finite volume methods for the shallow water equations with bathymetry and dry states. In P. L. F. Liu, H. Yeh, & C. Synolakis (Eds.), *Advanced Numerical Models for Simulating Tsunami Waves and Runup* (pp. 43-73). Singapore: World Scientific.

LeVeque, R. J., George, D. L., & Berger, M. J. (2011). Tsunami modeling with adaptively refined finite volume methods. *Acta Numerica. 20,* 211-289. https://doi.org/10.1017/S0962492911000043.

Lin, N., Emanuel, K. A., Smith, J. A., & Vanmarcke, E. (2010). Risk assessment of hurricane storm surge for New York City. *Journal of Geophysical Research: Atmospheres*, *115*(D18). https://doi.org/10.1029/2009JD013630

Lin, N., Kopp, R. E., Horton, B. P., & Donnelly, J. P. (2016). Hurricane Sandy's flood frequency increasing from year 1800 to 2100. *Proceedings of the National Academy of Sciences*, *113*(43), 12071–12075. https://doi.org/10.1073/pnas.1604386113

Lin, N., Marsooli, R., & Colle, B. A. (2019). Storm surge return levels induced by mid-to-late-twenty-first-century extratropical cyclones in the Northeastern United States. *Climatic Change*, *154*(1), 143–158. https://doi.org/10.1007/s10584-019-02431-8

Liu, Z., Fagherazzi, S., & Cui, B. (2021). Success of coastal wetlands restoration is driven by sediment availability. *Communications Earth & Environment*, *2*(1), 1–9. https://doi.org/10.1038/s43247-021-00117-7

Loveless, J. P., & Meade, B. J. (2011). Spatial correlation of interseismic coupling and coseismic rupture extent of the 2011 M_W = 9.0 Tohoku-oki earthquake. *Geophysical Research Letters, 38(17),* L17306. https://doi.org/10.1029/2011GL048561.

Loveless, J. P., & Meade, B. J. (2016). Two decades of spatiotemporal variations in subduction zone coupling offshore Japan. *Earth and Planetary Science Letters, 436,* 19-30. https://doi.org/10.1016/j.epsl.2015.12.033.

Maemoku, H. (1988). Holocene crustal movement in Muroto Peninsula, southwest Japan. *Geographical Review of Japan, Series A 61,* 747-769.

Maemoku, H. (2001). Reexamination of coseismic uplift of Cape Muroto, southwestern Japan, using AMS 14C ages of raised sessile organisms. *Chigaku Zasshi, 110,* 479-490. https://doi.org/10.5026/jgeography.110.4_479.

Mandli, K.T., Ahmadia, A. J., Berger, M., Calhoun, D., George, D. L., Hadjimichael, Y., et al. (2016). Clawpack: building an open source ecosystem for solving hyperbolic PDEs. *PeerJ Computer Science, 2(e68).* https://doi.org/10.7717/peerj-cs.68.

Marion, C., Anthony, E. J., & Trentesaux, A. (2009). Short-term (≤2 yrs) estuarine mudflat and saltmarsh sedimentation: High-resolution data from ultrasonic altimetery, rod surface-elevation table, and filter traps. *Estuarine, Coastal and Shelf Science*, *83*(4), 475–484. https://doi.org/10.1016/j.ecss.2009.03.039

Mariotti, G., & Fagherazzi, S. (2013). Critical width of tidal flats triggers marsh collapse in the absence of sea-level rise. *Proceedings of the National Academy of Sciences*, *110*(14), 5353–5356. https://doi.org/10.1073/pnas.1219600110

Mariotti, G., Kearney, W. S., & Fagherazzi, S. (2016). Soil creep in salt marshes. *Geology*, *44*(6), 459–462. https://doi.org/10.1130/G37708.1

Marsooli, R., Lin, N., Emanuel, K., & Feng, K. (2019). Climate change exacerbates hurricane flood hazards along US Atlantic and Gulf Coasts in spatially varying patterns. *Nature Communications*, *10*(1), 3785. https://doi.org/10.1038/s41467-019-11755-z

Martinez, J. M., Guyot, J. L., Filizola, N., & Sondag, F. (2009). Increase in suspended sediment discharge of the Amazon River assessed by monitoring network and satellite data. *CATENA*, *79*(3), 257–264. https://doi.org/10.1016/j.catena.2009.05.011

McCaffrey, R., Long, M. D., Goldfinger, C., Zwick, P. C., Nabelek, J. L., Johnson, C. K., & Smith, C. (2000). Rotation and plate locking at the southern Cascadia subduction zone. *Geophysical Research Letters, 27(19)*, 3117-3139. https://doi.org/10.1029/2000GL011768.

Meade, R. H. (1969). Landward transport of bottom sediments in estuaries of the atlantic coastal plain. *Journal of Sedimentary Research*, *39*(1), 222–234. https://doi.org/10.1306/74D71C1C-2B21-11D7-8648000102C1865D

Meade, B. J. (2007). Algorithms for the calculation of exact displacements, strains, and stresses for triangular dislocation elements in a uniform elastic half space. *Computers & Geosciences, 33(8),* 1064-1075. https://doi.org/10.1016/j.cageo.2006.12.003.

Melet, A., Meyssignac, B., Almar, R., & Le Cozannet, G. (2018). Under-estimated wave contribution to coastal sea-level rise. *Nature Climate Change*, *8*(3), 234–239. https://doi.org/10.1038/s41558-018-0088-y

Milliman, J. D., & Farnsworth, K. L. (2013). *River Discharge to the Coastal Ocean: A Global Synthesis*. Cambridge University Press.

Menéndez, M., & Woodworth, P. L. (2010). Changes in extreme high water levels based on a quasi-global tide-gauge data set. *Journal of Geophysical Research: Oceans*, *115*(C10). https://doi.org/10.1029/2009JC005997

Miyabe, N. (1955). Vertical earth movements in the Nankai district. *Bulletin of the Geographical Survey Institute*, *4*, 1-14.

Moftakhari, H. R., AghaKouchak, A., Sanders, B. F., Allaire, M., & Matthew, R. A. (2018). What Is Nuisance Flooding? Defining and Monitoring an Emerging Challenge. *Water Resources Research*, *54*(7), 4218–4227. https://doi.org/10.1029/2018WR022828

Moftakhari, H. R., AghaKouchak, A., Sanders, B. F., & Matthew, R. A. (2017). Cumulative hazard: The case of nuisance flooding. *Earth's Future*, *5*(2), 214–223. https://doi.org/10.1002/2016EF000494

Möller, I., Kudella, M., Rupprecht, F., Spencer, T., Paul, M., van Wesenbeeck, B. K., Wolters, G., Jensen, K., Bouma, T. J., Miranda-Lange, M., & Schimmels, S. (2014). Wave attenuation over coastal salt marshes under storm surge conditions. *Nature Geoscience*, *7*(10), 727–731. https://doi.org/10.1038/ngeo2251

Moreno, M., Rosenau, M., & Oncken, O. (2010). 2010 Maule earthquake slip correlates with pre-seismic locking of Andean subduction zone. *Nature, 467*, 198-202. https://doi.org/10.1038/nature09349.

Morris, J. T., Barber, D. C., Callaway, J. C., Chambers, R., Hagen, S. C., Hopkinson, C. S., Johnson, B. J., Megonigal, P., Neubauer, S. C., Troxler, T., & Wigand, C. (2016). Contributions of organic and inorganic matter to sediment volume and accretion in tidal wetlands at steady state. *Earth's Future*, *4*(4), 110–121. https://doi.org/10.1002/2015EF000334

Müller, M. (2012). The influence of changing stratification conditions on barotropic tidal transport and its implications for seasonal and secular changes of tides. *Continental Shelf Research*, *47*, 107–118. https://doi.org/10.1016/j.csr.2012.07.003

Müller, M., Arbic, B. K., & Mitrovica, J. X. (2011). Secular trends in ocean tides: Observations and model results. *Journal of Geophysical Research: Oceans*, *116*(C5). https://doi.org/10.1029/2010JC006387

Murakami, H., Itoh, S., Hiraiwa, Y., & Shimada, T. (1995). Re-examination of historical tsunamis in Shikoku Island, Japan. In Y. Tsuchiya & N. Shuto (Eds.), *Tsunami: Progress in Prediction, Disaster Prevention and Warning* (pp. 197-210). Dordrecht, Netherlands: Kluwer Academic Publishers.

Neumann, B., Vafeidis, A. T., Zimmermann, J., & Nicholls, R. J. (2015). Future Coastal Population Growth and Exposure to Sea-Level Rise and Coastal Flooding—A Global Assessment. *PLOS ONE*, *10*(3), e0118571. https://doi.org/10.1371/journal.pone.0118571

Nishimura, S., & Hashimoto, M. (2006). A model with rigid rotations and slip deficits for the GPS-derived velocity field in Southwest Japan. *Tectonophysics, 421(3-4)*, 187-207. https://doi.org/10.1016/j.tecto.2006.04.017.

Nishimura T., Yokota, Y., Tadokoro, K., & Ochi, T. (2018). Strain partitioning and interplate coupling along the northern margin of the Philippine Sea plate, estimated from Global Navigation Satellite System and Global Positioning System-Acoustic data. *Geosphere, 14(2)*. https://doi.org/10.1130/GES01529.1

NOAA_Technical_Report_NOS_COOPS_073.pdf. (n.d.). Retrieved April 30, 2020, from https://tidesandcurrents.noaa.gov/publications/NOAA_Technical_Report_NOS_COOPS_073.pdf

NYC. (2013). *A stronger, more resilient New York* (p. 435) [New York City PlaNYC Tech Rep.]. https://www1.nyc.gov/assets/sirr/downloads/pdf/Ch_2_ClimateAnalysis_FINAL_singles.pdf

Oppenheimer, M., Glavovic, B. C., Hinkel, J., van de Wal, R., Magnan, A. K., Abd-Elgawad, A., Cai, R., Cifuentes-Jara, M., DeConto, R. M., Ghosh, T., Hay, J., Isla, F., Marzeion, B., Meyssignac, B., & Sebesvari, Z. (n.d.). *Sea Level Rise and Implications for Low-Lying Islands, Coasts and Communities.* (IPCC Special Report on the Ocean and Cryosphere in a Changing Climate).

Orton, P., Georgas, N., Blumberg, A., & Pullen, J. (2012). Detailed modeling of recent severe storm tides in estuaries of the New York City region. *Journal of Geophysical Research: Oceans, 117*(C9). https://doi.org/10.1029/2012JC008220

Ozawa, S., Yarai, H., Imakiire, T., & Tobita, M. (2013). Spatial and temporal evolution of the long-term slow slip in the Bungo Channel, Japan. *Earth, Planets and Space, 65(2)*, 67-73. https://doi.org/10.5047/eps.2012.06.009.

Pawlowicz, R., Beardsley, B., & Lentz, S. (2002). Classical tidal harmonic analysis including error estimates in MATLAB using T_TIDE. *Computers & Geosciences*, *28*(8), 929–937. https://doi.org/10.1016/S0098-3004(02)00013-4

Pelling, H. E., & Green, J. A. M. (2013). Sea level rise and tidal power plants in the Gulf of Maine. *Journal of Geophysical Research: Oceans*, *118*(6), 2863–2873. https://doi.org/10.1002/jgrc.20221

Peng, D., Hill, E. M., Meltzner, A. J., & Switzer, A. D. (2019). Tide Gauge Records Show That the 18.61-Year Nodal Tidal Cycle Can Change High Water Levels by up to 30 cm. *Journal of Geophysical Research: Oceans*, *124*(1), 736–749. https://doi.org/10.1029/2018JC014695

Pethick, J. S. (1981). Long-term accretion rates on tidal salt marshes. *Journal of Sedimentary Research*, *51*(2), 571–577. https://doi.org/10.1306/212F7CDE-2B24-11D7-8648000102C1865D

Protti, M., González, V., Newman, A. V., Dixon, T. H., Schwartz, S. Y., Marshall, J. S., et al. (2014). Nicoya earthquake rupture anticipated by geodetic measurement of the locked plate interface. *Nature Geoscience*, 7, 117-121. https://doi.org/10.1038/ngeo2038.

Pugh D. T. & Vassie J. M. (1978). Extreme Sea Levels from Tide and Surge Probability. *Coastal Engineering 1978*, 911–930. https://doi.org/10.1061/9780872621909.054

Pugh, D., & Vassie, J. (1980). Applications of the joint probability method for extreme sea level computations. *Proceedings of the Institution of Civil Engineers*, *69*(4), 959–975. https://doi.org/10.1680/iicep.1980.2179

Rabinovich, A. B. (2009). Seiches and Harbor Oscillations. In *Handbook of Coastal and Ocean Engineering* (Vol. 1–0, pp. 193–236). WORLD SCIENTIFIC. https://doi.org/10.1142/9789812819307_0009

Ralston, D. K., Yellen, B., & Woodruff, J. D. (2021). Watershed Suspended Sediment Supply and Potential Impacts of Dam Removals for an Estuary. *Estuaries and Coasts*, *44*(5), 1195–1215. https://doi.org/10.1007/s12237-020-00873-3

Ray, R. D. (2006). Secular changes of the M2 tide in the Gulf of Maine. *Continental Shelf Research*, *26*(3), 422–427. https://doi.org/10.1016/j.csr.2005.12.005

Ray, R. D., & Foster, G. (2016). Future nuisance flooding at Boston caused by astronomical tides alone. *Earth's Future*, *4*(12), 578–587. https://doi.org/10.1002/2016EF000423

Ray, R. D., & Merrifield, M. A. (2019). The Semiannual and 4.4-Year Modulations of Extreme High Tides. *Journal of Geophysical Research: Oceans*, *124*(8), 5907–5922. https://doi.org/10.1029/2019JC015061

Ray, R. D., & Talke, S. A. (2019). Nineteenth-Century Tides in the Gulf of Maine and Implications for Secular Trends. *Journal of Geophysical Research: Oceans*, *124*(10), 7046–7067. https://doi.org/10.1029/2019JC015277

Redfield, A. C. (1972). Development of a New England Salt Marsh. *Ecological Monographs*, *42*(2), 201–237. https://doi.org/10.2307/1942263

Redfield, A. C., & Miller, A. R. (1957). Water Levels Accompanying Atlantic Coast Hurricanes. In A. C. Redfield, A. R. Miller, G. W. Groves, D. L. Harris, R. O. Reid, W. Marks, & J. Chase (Eds.), *Interaction of Sea and Atmosphere: A Group of Contributions* (pp. 1–23). American Meteorological Society. https://doi.org/10.1007/978-1-940033-15-0_1

Reed, D. J. (1989). Patterns of sediment deposition in subsiding coastal salt marshes, Terrebonne Bay, Louisiana: The role of winter storms. *Estuaries*, *12*(4), 222–227. https://doi.org/10.2307/1351901

Reed, D. J., Spencer, T., Murray, A. L., French, J. R., & Leonard, L. (1999). Marsh surface sediment deposition and the role of tidal creeks: Implications for created and managed coastal marshes. *Journal of Coastal Conservation*, *5*(1), 81–90. https://doi.org/10.1007/BF02802742

Sagiya T. & Thatcher, W. (1999). Coseismic slip resolution along a plate boundary megathrust: The Nankai Trough, southwest Japan. *Journal of Geophysical Research, 104(B1),*1111–1129. https://doi.org/10.1029/98JB02644.

Sagiya, T., Miyazaki, S., & Tada, T. (2000). Continuous GPS array and present-day crustal deformation of Japan. *Pure and Applied Geophysics, 157(11-12),* 2303-2322. https://doi.org/10.1007/PL00022507.

Sakaguchi, A., Chester, F., Curewitz, D., Fabbri, O., Goldsby, D., Kimura, G., et al. (2011). Seismic slip propagation to the up-dip end of plate boundary subduction interface faults: vitrinite reflectance geothermometry on Integrated Ocean Drilling Program NanTroSEIZE cores. *Geology, 39(4),* 395-398. https://doi.org/10.1130/G31642.1.

Schindelegger, M., Green, J. a. M., Wilmes, S.-B., & Haigh, I. D. (2018). Can We Model the Effect of Observed Sea Level Rise on Tides? *Journal of Geophysical Research: Oceans*, *123*(7), 4593–4609. https://doi.org/10.1029/2018JC013959

Shishikura, M. (2013). Earthquake and tsunamis along the Nankai Trough, inferred from geology and geomorphology – examples in Nankai region. *Geological Survey Institute of Japan Chishitsu News, 2,* 201-204.

Shishikura, M., Echigo, T., Maemoku, H., & Ishiyama, T. (2008). Height and ages of uplifted sessile assemblage distributed along the southern coast of the Kii Peninsula, south-central Japan – reconstruction of multi-segment earthquake history along the Nankai Trough. *Annual Report on Active Fault and Paleoearthquake Researches, 8,* 267-280.

Sobey, R. J. (2005). Extreme low and high water levels. *Coastal Engineering*, *52*(1), 63–77. https://doi.org/10.1016/j.coastaleng.2004.09.003

Sousa, A. I., Lillebø, A. I., Pardal, M. A., & Caçador, I. (2010). Productivity and nutrient cycling in salt marshes: Contribution to ecosystem health. *Estuarine, Coastal and Shelf Science*, *87*(4), 640–646. https://doi.org/10.1016/j.ecss.2010.03.007

Sweet, W. V., Dusek, G. W., Carbin, G. W., Marra, J. J., Marcy, D. C., & Simon, S. (2020). *2019 State of U.S. High Tide Flooding with a 2020 Outlook.* https://doi.org/10.25923/Q56G-BA90

Sweet, W. V., Dusek, G. W., Obeysekera, J. T. B., & Marra, J. J. (2018). *Patterns and projections of high tide flooding along the U.S. coastline using a common impact threshold.* [PDF]. https://doi.org/10.7289/V5/TR-NOS-COOPS-086

Sweet, W. V., Kopp, R. E., Weaver, C. P., Obeysekera, J., Horton, R. M., Thieler, E. R., & Zervas, C. E. (2017). *Global and Regional Sea Level Rise Scenarios for the United States* (NOAA Tech. Rep. NOS CO-OPS 83).

Sweet, W. V., Park, J., Marra, J. J., Zervas, C., & Gill, S. (2014). *Sea Level Rise and Nuisance Flood Frequency Changes around the United States* (p. 53) [NOAA Technical Report NOS CO-OPS 73; PDF]. U.S. Department of Commerce, National Oceanic and Atmospheric Administration, National Ocean Service, Center for Operational Oceanographic Products and Services. http://tidesandcurrents.noaa.gov/publications/NOAA_Technical_Report_NOS_COOPS_073.pdf

Sweet, W. V., Zervas, C. E., & Gill, S. (n.d.). *Elevated East Coast Sea Levels Anomaly: June–July 2009* (p. 28) [NOAA Technical Report NOS CO-OPS 051]. https://tidesandcurrents.noaa.gov/publications/EastCoastSeaLevelAnomaly_2009.pdf

Talke, S. A., & Jay, D. A. (2020). Changing Tides: The Role of Natural and Anthropogenic Factors. *Annual Review of Marine Science*, *12*, 121–151. https://doi.org/10.1146/annurev-marine-010419-010727

Talke, S. A., Kemp, A. C., & Woodruff, J. (2018). Relative Sea Level, Tides, and Extreme Water Levels in Boston Harbor From 1825 to 2018. *Journal of Geophysical Research: Oceans*, *123*(6), 3895–3914. https://doi.org/10.1029/2017JC013645

Talke, S. A., Mahedy, A., Jay, D. A., Lau, P., Hilley, C., & Hudson, A. (2020). Sea Level, Tidal, and River Flow Trends in the Lower Columbia River Estuary, 1853–present. *Journal of Geophysical Research: Oceans*, *125*(3), e2019JC015656. https://doi.org/10.1029/2019JC015656

Talke S. A., Orton P., & Jay D. A. (2014). Increasing storm tides in New York Harbor, 1844–2013. *Geophysical Research Letters*, *41*(9), 3149–3155. https://doi.org/10.1002/2014GL059574

Tawn, J. A. (1992). Estimating Probabilities of Extreme Sea-Levels. *Journal of the Royal Statistical Society: Series C (Applied Statistics)*, *41*(1), 77–93. https://doi.org/10.2307/2347619

Tawn, J. A., & Vassie, J. M. (1989). *EXTREME SEA LEVELS: THE JOINT PROBABILITIES METHOD REVISITED AND REVISED*. https://trid.trb.org/view/435293

Tebaldi, C., Strauss, B. H., & Zervas, C. E. (2012). Modelling sea level rise impacts on storm surges along US coasts. *Environmental Research Letters*, *7*(1), 014032. https://doi.org/10.1088/1748-9326/7/1/014032

Temmerman, S., Govers, G., Wartel, S., & Meire, P. (2003). Spatial and temporal factors controlling short-term sedimentation in a salt and freshwater tidal marsh, Scheldt estuary, Belgium, SW Netherlands. *Earth Surface Processes and Landforms*, *28*(7), 739–755. https://doi.org/10.1002/esp.495

Tetra Tech EC, Inc. (2005). *Comprehensive Site Assessment Report: Fireworks I*. http://eeaonline.eea.state.ma.us/EEA/FileViewer/Scanned.aspx?id=206833

Thieler, E. R., Smith, T. L., Knisel, J. M., & Sampson, D. W. (2013). *Massachusetts Shoreline Change Mapping and Analysis Project, 2013 Update* (U.S. Geological Survey Open-File Report 2012-1189, p. 42). http://pubs.usgs.gov/of/2012/1189/

Thompson, P. R., Mitchum, G. T., Vonesch, C., & Li, J. (2013). Variability of Winter Storminess in the Eastern United States during the Twentieth Century from Tide Gauges. *Journal of Climate*, *26*(23), 9713–9726. https://doi.org/10.1175/JCLI-D-12-00561.1

Thompson, P. R., Widlansky, M. J., Hamlington, B. D., Merrifield, M. A., Marra, J. J., Mitchum, G. T., & Sweet, W. (2021). Rapid increases and extreme months in projections of United States high-tide flooding. *Nature Climate Change*, *11*(7), 584–590. https://doi.org/10.1038/s41558-021-01077-8

Thompson, P. R., Widlansky, M. J., Merrifield, M. A., Becker, J. M., & Marra, J. J. (2019). A Statistical Model for Frequency of Coastal Flooding in Honolulu, Hawaii, During the 21st Century. *Journal of Geophysical Research: Oceans*, *124*(4), 2787–2802. https://doi.org/10.1029/2018JC014741

Town of Hanover, MA. (2008). *Fireworks I Site*. https://www.hanover-ma.gov/sites/g/files/vyhlif666/f/file/file/2008_fact_sheet.pdf

Turner, R. E., Baustian, J. J., Swenson, E. M., & Spicer, J. S. (2006). Wetland Sedimentation from Hurricanes Katrina and Rita. *Science*, *314*(5798), 449–452. https://doi.org/10.1126/science.1129116

US Air Force. (2014). *Final Environmental Assessment to Renovate Fourth Cliff Recreational Area at Hanscom Air Force Base, Massachusetts*. https://apps.dtic.mil/sti/pdfs/ADA617408.pdf

U.S. Fish and Wildlife Service. (2013). *National Wetlands Inventory website*. U.S. Department of the Interior, Fish and Wildlife Service. http://www.fws.gov/wetlands/

U.S. Geological Survey. (2016). *The StreamStats program for Massachusetts*. http://water.usgs.gov/osw/streamstats/massachusetts.html

Vousdoukas, M. I., Voukouvalas, E., Mentaschi, L., Dottori, F., Giardino, A., Bouziotas, D., Bianchi, A., Salamon, P., & Feyen, L. (2016). Developments in large-scale coastal flood hazard mapping. *Natural Hazards and Earth System Sciences*, *16*(8), 1841–1853. https://doi.org/10.5194/nhess-16-1841-2016

Wahl, T., & Chambers, D. P. (2015). Evidence for multidecadal variability in US extreme sea level records. *Journal of Geophysical Research: Oceans*, *120*(3), 1527–1544. https://doi.org/10.1002/2014JC010443

Wahl, T., Haigh, I. D., Nicholls, R. J., Arns, A., Dangendorf, S., Hinkel, J., & Slangen, A. B. A. (2017). Understanding extreme sea levels for broad-scale coastal impact and adaptation analysis. *Nature Communications*, *8*(1), 1–12. https://doi.org/10.1038/ncomms16075

Ward, L. (2004). Variations in physical properties and water quality in the Webhannet River Estuary (Wells National Estuarine Research Reserve, Maine). *Journal of Coastal Research*, *45*, *Special Issue*. https://doi.org/10.2112/SI45-039.1

Weston, N. B. (2014). Declining Sediments and Rising Seas: An Unfortunate Convergence for Tidal Wetlands. *Estuaries and Coasts*, *37*(1), 1–23. https://doi.org/10.1007/s12237-013-9654-8

Williams, J., Horsburgh, K. J., Williams, J. A., & Proctor, R. N. F. (2016). Tide and skew surge independence: New insights for flood risk. *Geophysical Research Letters*, *43*(12), 6410–6417. https://doi.org/10.1002/2016GL069522

Winterwerp, J. C., Wang, Z. B., van Braeckel, A., van Holland, G., & Kösters, F. (2013). Man-induced regime shifts in small estuaries—II: A comparison of rivers. *Ocean Dynamics*, *63*(11), 1293–1306. https://doi.org/10.1007/s10236-013-0663-8

Wolf, J. (2008). Coupled wave and surge modelling and implications for coastal flooding. *Advances in Geosciences*, *17*, 19–22. https://doi.org/10.5194/adgeo-17-19-2008

Wolf, J. (2009). Coastal flooding: Impacts of coupled wave–surge–tide models. *Natural Hazards*, *49*(2), 241–260. https://doi.org/10.1007/s11069-008-9316-5

Woodruff, J. D., Venti, N. L., Mabee, S. B., DiTroia, A. L., & Beach, D. (2021). Grain size and beach face slope on paraglacial beaches of New England, USA. *Marine Geology*, *438*, 106527. https://doi.org/10.1016/j.margeo.2021.106527

Woodworth, P. L. (2010). A survey of recent changes in the main components of the ocean tide. *Continental Shelf Research*, *30*(15), 1680–1691. https://doi.org/10.1016/j.csr.2010.07.002

Woodworth, P. L., Melet, A., Marcos, M., Ray, R. D., Wöppelmann, G., Sasaki, Y. N., Cirano, M., Hibbert, A., Huthnance, J. M., Monserrat, S., & Merrifield, M. A. (2019). Forcing Factors Affecting Sea Level Changes at the Coast. *Surveys in Geophysics*, *40*(6), 1351–1397. https://doi.org/10.1007/s10712-019-09531-1

Yellen, B. C., Woodruff, J. D., Geyer, W. R., Baranes, H. E., Ralston, D. K., Engelhart, S., & Randall, N. (In prep.). Rapid salt marsh aggradation following instantaneous rise in effective sea level. *Journal of Geophysical Research: Earth Surface*.

Yasuda, K., Tadokoro, K., Taniguchi, S., Kimura, H., & Matsuhiro, K. (2017). Interplate locking condition derived from seafloor geodetic observation in the shallowest subduction segment at the Central Nankai Trough, Japan. *Geophysical Research Letters, 44(8)*, 3572-3579. https://doi.org/10.1002/2017GL072918.

Yokota, Y., Ishikawa, T., Watanabe, S., Tashiro, T., & Asada, A. (2016). Seafloor geodetic constraints on interplate coupling of the Nankai Trough megathrust zone. *Nature, 534*, 374-377. https://doi.org/10.1038/nature17632.

Zervas, C. (2013). *Extreme Water Levels of the United States 1893-2010* (NOAA Technical Report NOS CO-OPS 067; p. 200). NOAA. https://tidesandcurrents.noaa.gov/publications/NOAA_Technical_Report_NOS_COOPS_067a.pdf

Zhao, L., Chen, C., Vallino, J., Hopkinson, C., Beardsley, R. C., Lin, H., & Lerczak, J. (2010). Wetland-estuarine-shelf interactions in the Plum Island Sound and Merrimack River in the Massachusetts coast. *Journal of Geophysical Research: Oceans, 115*(C10). https://doi.org/10.1029/2009JC006085